BULGARIAN ACADEMY OF SCIENCES

INSTITUTE OF NUCLEAR RESEARCH AND NUCLEAR ENERGY

Mariana Filipova Shopova

PERFORMANCE OF THE CMS RPC SYSTEM – FROM LS1 UPGRADE TO RUN2 AT LHC

THESIS

for obtaining the degree of
Doctor of Philosophy

Supervisor: Assoc. Prof. Dr. Plamen Iaydjiev

Sofia, 2018

Acknowledgements

This thesis is one of my major accomplishments, but it is because of a lot of people I managed to finally have it done. I would like to express my sincere gratitude for the invaluable support of my supervisor, colleagues, friends and family.

I wouldn't be who I am without all of you!

I am very thankful to my supervisor Dr. Plamen Iaydjiev, who helped me and guided me throughout the journey of my thesis writing. I would like to thank him for the professionalism, support and patience, as well as the never ending positivism in answering all of my questions.

I am very thankful to Dr. Roumyana Hadjiiska, who guided me and thought me throughout the long process of analyzing experimental data. I would like to thank her for the never-ending support and patience, for her professionalism and rigorousness. She helped me become the professional I am today.

I would like to thank to Dr. Gueorgui Soultanov, Dr. Aleksandar Aleksandrov, Mircho Rodozov and Dr. Peter Vankov for their invaluable help, discussions and the friendly atmosphere in our group.

I would like to thank to my colleagues from Sofia University for the discussions, help and support, as well as the friendly atmosphere in the Bulgarian office in CERN.

Here is the place to thank to all the members of the RPC Community and especially the colleagues I have worked with throughout the years. They helped me learn and grow in a stimulating and fun environment.

I would like to thank to all of my friends for the help, the support and belief in me. I am grateful for the moments of fun, joy and happiness we shared, for the difficult times they were there for me and the moments they helped me even unknowingly. Even not present here by their names, they know who I refer to.

Finally, but most importantly, I would like to say "Thank you!" to my family, who are there for me throughout all of my life – loving, supporting and believing in me. I would also like to thank to my kids, who never stopped asking me when I will finish writing, so I can continue playing with them. I dedicate this thesis to them.

Contents

Introduction

Understanding elementary particles and their interactions is the main task of scientific society for more than a century. This continuing journey starts with the discovery of X-rays by W. C. Röntgen in 1895. After years of theoretical and experimental progress, establishing and proving quantum mechanics and discovering of new particles, a united model describing the electromagnetic, strong and weak forces is developed. The Standard Model (SM) is a field theory in which theoretical predictions agree extraordinarily well with experimental observations. After years of extensive testing and doubting its accuracy, the basic principles of the SM still stand. It managed to predict the existence and the discovery of the top quark, the tau neutrino and a lot more particles including the most recently discovered Higgs boson in 2012. Yet SM is not a complete theory of everything, but more a low-energy limit of a more profound theory. It does not explain and incorporate gravity, does not give an answer to why the electro-weak scale and the Planck scale are so disparate, it does not have a viable candidate for dark matter and gives no explanation of the hierarchy problem.

There are numerous extensions to the Standard Model, a lot of revisions and replacements in it attempting to correct these and other issues. All those theories require verification, while unfortunately at present moment there is no experimental evidence for any of them over the other. This leads to exploring of the physics at the TeV energy scale.

The Large Hadron Collider (LHC) at the European Organization for Nuclear Research (CERN) is a proton-proton accelerator built with the main goal to test all these theories. The LHC lies in a tunnel 27 km in circumference and 175 m beneath the surface near Geneva, Switzerland, which makes it the world's largest particle accelerator. It has a design center-of-mass energy of 14 TeV and luminosity of $10^{34}cm^{-2}s^{-1}$ which also makes it the highest-energy accelerator. It collide oppositely circulating beams of either protons or lead nuclei.

The Compact Muon Solenoid (CMS) detector is one of the two multipurpose experiments at the LHC. It was built to record and reconstruct proton-proton collisions at very high precision level. The final-state muons that these events are expected to produce are of particular interest in studying very high-energy physics processes. CMS has been collecting data successfully since the start of the first LHC physics run in 2009. In order to be able to record the final state muons, the CMS experiment has a highly efficient and redundant muon system, which is specialized in covering the muon identification, momentum measurement and trigger. There are three types of gas detectors used in it. In the barrel region ($|\eta| < 1.2$) Drift Tubes chambers (DT) and Resistive Plate Chambers (RPC) are used, while in the endcap region there are Cathode Strip Chambers (CSC), which cover up to $|\eta| < 2.4$ and RPCs up to $|\eta| < 1.9$.

This thesis is structured in seven chapters. The first one gives the physics behind LHC, while the second and the third chapter describe the LHC accelerator and the CMS experiment. The forth chapter is devoted to Resistive Plate Chambers. The fifth chapter gives a detailed review of the CMS muon system upgrade during LS1, and the sixth chapter presents the performance of the CMS RPC system during Run 2. Chapter 7 describes the personal involvement of the doctorate candidate.

1. Physics Studies

1.1. Standard Model of particle physics

In Particle Physics, the relativistic Quantum Field Theory used to describe the fundamental building blocks of matter and their interactions with each other is called the Standard Model (SM) [1]. This model combines successfully the Electroweak theory [2], which describes electromagnetic and weak interactions, with Quantum Chromodynamics (QCD) [3], which gives description of strong interactions.

The matter constituents in the SM are called fermions. These are half spin particles (spin ½) which interact with each other by the exchange of other particles called gauge bosons (spin 1). The fermions are divided into two major types – quarks and leptons. There are 6 quarks and 6 leptons paired into three generations, depending on their mass. The quark generations, also called families, are made out of two quarks each – up (u) and down (d) in the first, charm (c) and strange (s) in the second and top (t) and bottom (b) in the third. The lepton generations are made of one electrically charged and one neutral particle. The charged leptons in the three generations are electron (e), muon (μ) and tau (τ) for the first, second and third generation respectively, while the neutral leptons are called neutrinos (ν) – electron- (ν_e), muon- (ν_μ) and tau neutrino (ν_τ). Quarks hold electric charge, weak isospin and color charge and because of that interact through both electroweak and strong forces. Quarks have never been observed as free particles due to confinement (a strong interactions property). They are forming bound states of color neutral particles called hadrons, which are divided into baryons and mesons. Leptons can interact only through electroweak force since they have zero color charge. Neutrinos also interact only via the weak force as they are also not electrically charged.

The up quark has an electric charge of $+\frac{2}{3}e$, while the electric charge of the down quark is $-\frac{1}{3}e$. The electron has a negative charge of $-e$, and as mentioned, the neutrino is a neutral particle. These four particles, i.e. the first generation of fermions, are the constituents of all stable matter observed in the universe. For each of the fermions there is an anti-particle with exactly the same coupling but opposite quantum numbers.

Diagram of the particles in the Standard Model, sorted by generations and ordered with respect to their mass is shown in figure 1.1. Although neutrinos are described as massless particles in the SM, recent experiments proved that they have very small but still existing masses [4]. The logarithmic scale for the mass in the figure shows that each fermion generation is drastically more massive than the previous one.

In order to exist in the form of matter, elementary particles interact with each other through four types of interactions. So far only three of these interactions have been experimentally observed among fermions – electromagnetic, weak and strong. The fundamental interactions are mediated by gauge bosons and for each fundamental force behind the interaction, there is a special boson carrying it.

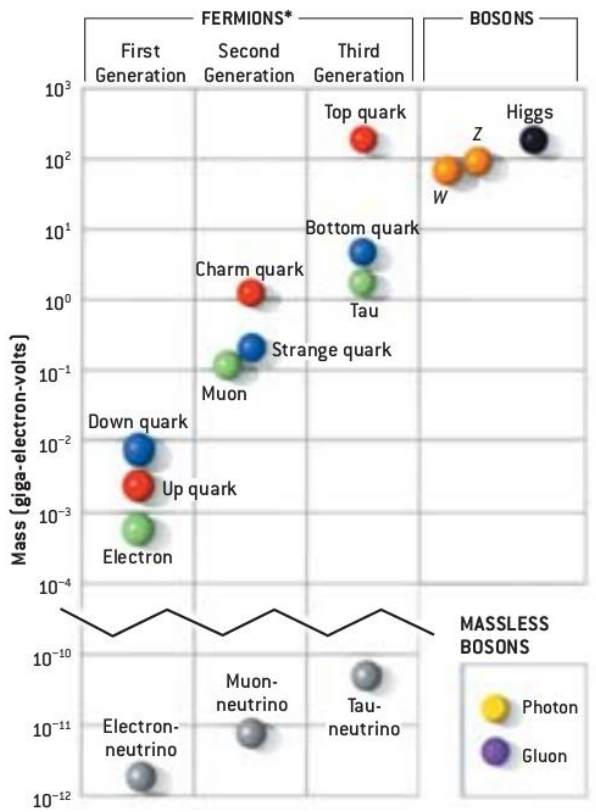

Figure 1.1: Elementary particles in the Standard Model shown with respect to their masses [5].

The photons (γ) are massless particles mediating the electromagnetic force, the charged W^+ and W^- bosons and the neutral Z^0 boson are mediators of the weak force, while the gluons (g) are the strong force mediators. The $W^{\pm}$ and the Z bosons are massive particles and their masses are $m_W = 80.399 \pm 0.023\ GeV$ and $m_Z = 91.1876 \pm 0.0021\ GeV$ [6]. According to the QCD there are eight different massless gluons which have a color charge and can also interact with each other. The color charge comes in three flavors – red (r), green (g) and blue (b).

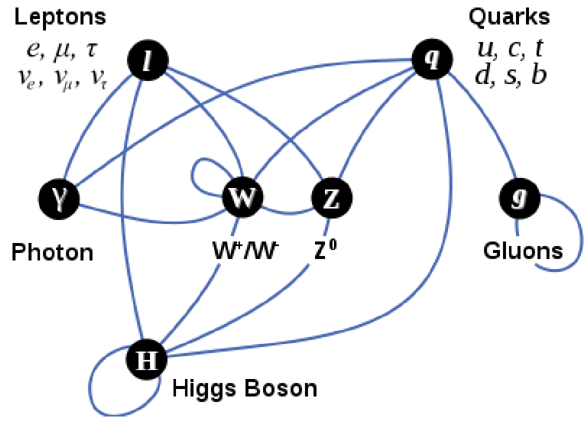

Figure 1.2: Scheme of interactions between the constituents of the Standard Model © Wikipedia.

The forth known fundamental force – gravity is not part of the Standard Model. In the large scale world it is an extremely strong force keeping the planets in their orbits around stars, but in particle physics it is negligible in comparison with the magnitude of the other three forces. Figure 1.2 shows the allowed interactions between the particles of the SM.

The Standard Model of particle physics is the most successful Quantum Field Theory (QFT) to describe all elementary particles and interaction fields so far. The Elektroweak (EWK) theory combines the electromagnetic and weak interactions, while the strong interaction is described by Quantum Chromodynamics (QCD). The mass of particles is added by an additional mechanism which describes the electroweak symmetry breaking – Higgs mechanism.

A more detailed review of the mathematical foundation of the SM in the theory of gauge symmetries can be found in [7].

1.2. Higgs boson

Understanding the mechanism behind electroweak symmetry breaking is one of the most important objectives in high energy physics. Three groups of researchers postulate independently the existence of a special scalar field which adds mass to all known particles. The mechanism behind this field is called the Brout-Englert-Higgs mechanism, which postulates the existence of the Higgs boson (H) and thus adds mass to the weak gauge bosons [8-12]. Yukawa couplings with the Higgs scalar field on the other hand give mass to the fermions [13-15].

It takes more than 48 years before the experimental observation of the postulated Higgs boson is reported. In 2012 the ATLAS and CMS Collaborations at the LHC observe independently a new boson with mass near 125 GeV [16-18]. All subsequent measurements of the production, decay rates and the spin-parity quantum numbers of the new boson [19-24] show that its properties are compatible with the ones expected for the SM Higgs. The CDF and D0 experiments also reported a consistent with the LHC observations excess of events [25, 26].

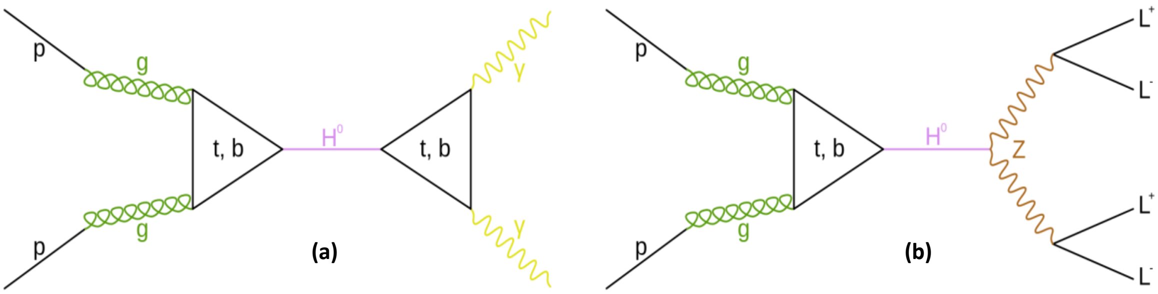

Figure 1.3: Feynman diagrams of the cleanest Higgs production channels – diphoton channel (a) and 4-lepton channel (b).

Based on all studies results, the newly discovered boson can be described as a massive scalar boson, which has no spin and zero electric and color charge. It is its own anti-particle and has even parity. Figure 1.3 shows the Feynman diagrams of cleanest channels associated with the Higgs boson observation. The production mechanism involves two gluons from each proton, which fuse to a top quark or W boson loop. The loop couples strongly to the Higgs field to produce a Higgs boson. In the diphoton channel, Higgs decays subsequently into 2 gamma ray photons by virtual interaction with a top quark or W boson loop, while in the 4-lepton channel, the Higgs emits 2 Z bosons, which decay into 2 leptons (electrons, muons) each. Experimental analyses of these channels reach a significance of more than 5 σ in both the ATLAS and CMS experiments [23, 24].

1.3. Beyond the Standard Model

The Standard Model of Particle Physics is a very successful theory, tested and questioned for more than a century. Still it seems not entirely compatible with the ultimate description of nature. There are a number of questions and problems both theoretical and phenomenological that do not have an explanation in the SM. Why the exact number of quark and lepton generations is three, what is the explanation of the values of the mixing angles in the CKM matrix [27, 28, 29] and the values of the masses of the particles, why there is a baryon asymmetry…, these are all questions that need an answer and unfortunately the Standard Model cannot give one.

One of the major problems with no explanation in this theory is the so called hierarchy problem – it comes from the huge difference in the scales of magnitude for electroweak physics ($m_Z \sim 10^2 GeV$) and the fundamental gravity scale (Plank mass scale – $m_P \sim 10^{19} GeV$). The SM already describes all fundamental interactions but the gravitational one, so no new physics is expected in between these two scales.

Another major problem is the unification of the coupling constants. There is a belief that following the good unification of the electromagnetism and weak interaction, it will be possible to unify all fundamental interactions and thus describe them by a single symmetry group. Unfortunately no evidence for this unification possibility is observed so far, so new physics at higher energies must be searched.

Gravitational interactions are also not defined in the SM which makes the model incomplete by itself. There is also no explanation of the observed existence of neutral non-baryonic matter. It is called dark matter and based on cosmic microwave background studies it is 6 times more than baryonic (SM postulated) matter in the universe [30]. Another cosmological problem with no explanation is the asymmetry between matter and anti-matter.

A number of promising models have been introduced throughout the years in order to extend or replace the Standard Model. So far there is no experimental evidence accepting or rejecting any of them.

1.3.1. Supersymmetry

Supersymmetry (SUSY) [31] is one of the most promising extensions of the Standard Model. It introduces symmetry between bosons and fermions [32] by allowing for each boson to be introduced a fermion and vice versa. Thus unification of the bosons and fermions at the Planck scale is allowed. SUSY comes with a spectrum of new particles, including some candidates for dark matter. Figure 1.4 shows the SM particles and their possible SUSY partners.

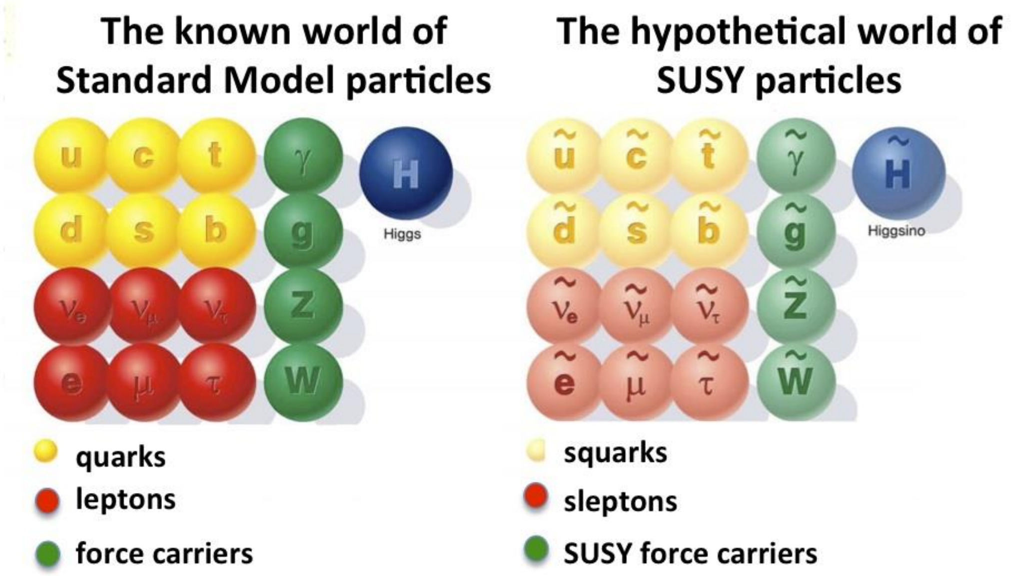

Figure 1.4: Standard Model particles and their hypothetical Supersummetry partners.

Supersymmetry is a very natural theory which gives solution to a number of SM inconsistencies. Since there are still no super partners of the SM particles discovered though, SUSY must be broken. Thus it solves the gauge hierarchy problem since with the introduction of bosons as super partners of the SM fermions, the quantum corrections to the Higgs mass would cancel out in a natural way. It also provides the means for completing the unification of strong and electroweak interactions, since when the SM gauge couplings are extrapolated to higher scale $M_{GUT} \sim 10^{16}\ GeV$ they meet at a single point. There is a special R-parity introduced in the SUSY model, which results in that the lightest supersymmetric particle (LSP) has to be stable and this particle is a very good candidate for dark matter.

1.3.2. Other possible SM extension scenarios

There are several other alternative theories and models for extending the Standard Model in a bit different way than the supersymmetry. Introducing extra space-time dimensions in the theory can help with solving the hierarchy problem and integrating gravity at the quantum level. Thus instead of cancelling the divergences, the Planck scale is leveled with the TeV energy scale. There are two possible scenarios for introducing extra dimensions – either they are too big (brain scenarios) or they are very small, so in both cases they are unreachable from the four space-time dimensional world. There are a lot of extra dimensional models and some of them predict at the high energy TeV scale some new particles like radions and gravitons can be produced. String theory for example requires both supersymmetry and extra dimensions. It treats particles as extended objects.

There are a number of other exotic scenarios proposed as alternatives to these ones beyond the SM. In general in such scenarios new matter fields are needed. Finding new unobserved so far particles will help to determine the correct theory which can extend our current knowledge of the way nature works. There is an overview of many of these models and scenarios in [33-35].

1.4. Cosmic rays

Cosmic rays are high-energy particles originating mainly from supernovae, quasars and other astronomical events, but also from the solar flares [36].They can be divided into two separate parts – primary cosmic rays and secondary cosmic rays. The primary are the ones entering the terrestrial atmosphere – protons and alpha particles (99%) with a small amount of heavier nuclei (~1%), which are synthesized in stars. Interaction of the primaries with the nuclei from the upper layers of the atmosphere results in forming a shower of particles, which are referred as secondary cosmic rays. A cosmic ray cascade of a primary particle, forming a shower of secondary particles is shown in figure 1.5.

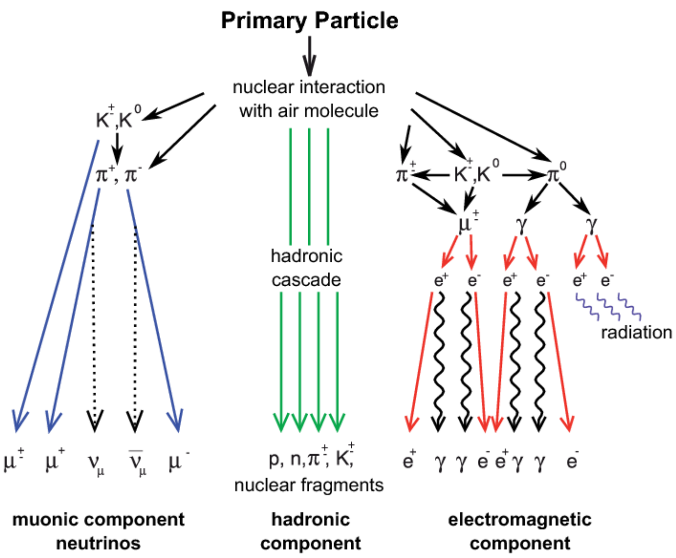

Figure 1.5: Primary cosmic particle collides with an atmosphere molecule [37].

Majority of the newly produced particles are neutral (π^0) and charged ($\pi^{\pm}$) pions [38]. The neutral pions decay into gamma-rays (γ) with a very short lifetime – less than 10^{-17} s, generating electro-magnetic showers from electron-positron pairs ($e^{\pm}$). The charged pions, which do not undergo further nuclear reactions, decay into positive and negative muons ($\mu^{\pm}$) and muon neutrinos ($\nu_\mu, \overline{\nu_\mu}$). Fast nucleons, kaons ($K^{\pm}$, K^0), as well as neutrons (n) and protons (p) can also be created during the cosmic ray cascade of secondary particles. Assuming they have enough energy, they can also interact with other air nuclei, forming lower energetic nucleons, neutrons and protons.

The majority of particles from the secondary particle shower, which reach sea level, are muons. Muons are discovered in 1937 while studying the cosmic rays [39]. They have a very high energy and an average lifetime of 2.2 μs, which though seeming extremely short allows them to travel long distances in the atmosphere. The distance muons can travel before they decay lengthens with the increase of their energy. This correlation is explained by the time dilation predicted by the Einstein relativity theory [40]. Muons have a spin of ½, but they are about 207 times heavier than electrons with a mass of 105.7 MeV/c^2. This allows them to penetrate far more deeply into matter than electrons, since they are not so influenced by electromagnetic fields and don't emit deceleration radiation (bremsstrahlung). Some muons can be detected even at depths below 500 meters and are the only particles which can be observed there. More than 10 000 muons coming from the secondary particle showers reach Earth's surface every square meter per minute. Apart as products of the cosmic rays interaction with atmosphere, muons can be created also in large particle accelerators, as result of collisions between high energy particles. All their properties make them a never-ending source for different experiments and researches. Muon studies give a good opportunity to learn more about the interactions of cosmic rays with the atmosphere and to study the weak interactions between particles. They are also used for studying different geographical objects, materials and medical applications [41-45].

2. The Large Hadron Collider

2.1 LHC overview

The Large Hadron Collider (LHC) [46] is the highest-energy particle accelerator ever built. It accelerates and collides beams of oppositely circulating protons and heavy ions. The design and the operation of this discovery machine are driven by the goal to explore new frontiers in physics at the TeV energy scale. Hopefully this new high-energy physics will bring some light on the nature of electroweak symmetry breaking and the Beyond Standard Model phenomena.

Located at the European Organization for Nuclear Research (CERN) near Geneva (Switzerland), LHC is installed in the 27 km circular tunnel of the former Large Electron-Positron Collider (LEP) near the French-Swiss border, some 100 m beneath the surface. Inside the tunnel there are mainly superconducting magnets with a number of accelerating structures to keep the energy of the accelerated particles. Figure 2.1 shows the layout of the LHC tunnel.

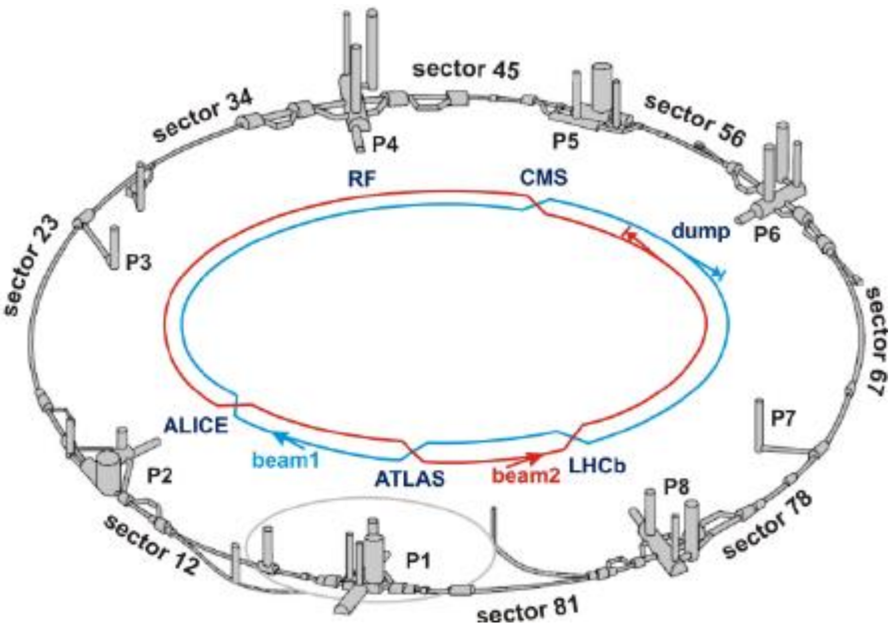

Figure 2.1: Layout of the Large Hadron Collider [47]. Particles rotate in two beams with opposite directions, crossing at four interaction regions where the main experiments are located.

The LHC is designed as proton-proton collider with optimal center-of-mass energy of 14 TeV and foreseen luminosity of $\mathcal{L} = 10^{34}$ cm^{-2}s^{-1}. It can also collide heavy ions ($^{208}Pb^{82+}$), with beam energies of 2.76 TeV/nucleon, a total center-of-mass energy of 1.148 PeV and nominal luminosity of $\mathcal{L} = 10^{27}$ cm^{-2}s^{-1}.

Colliding protons (pp) instead of electron-positron($e\bar{e}$), like in LEP, allows high intensity beams, thus increasing the collision rates and resulting in decreasing of the minimal cross section to be probed. Table 2.1 shows the design parameters for LHC for proton and lead beams.

Though using this design, the LHC is not a perfectly circular collider (figure 2.1). It consists of eight straight sections, which are around 5 km in total, and 22 km of curved sections divided into eight sectors. The straight sections are used as injection regions. At four of them the physics experiments are built. One houses the acceleration system, one the beam dump, and the beam cleaning systems are installed at the remaining two. The curved sections are occupied by magnets and the systems to make them functional.

Parameters	p-p collisions	Pb-Pb collisions
Center-of-mass energy (TeV)	14	1148
Number of particles per bunch	1.1×10^{11}	$\sim 8 \times 10^{7}$
Number of bunches	2808	608
Design Luminosity ($cm^{-2}s^{-1}$)	10^{34}	2×10^{27}
Bunch length (mm)	53	75
Beam radius at interaction point (μm)	15	15
Time between collisions (ns)	25	124.75×10^{3}
Bunch crossing rate (MHz)	40.08	0.008
Circumference (km)	~ 27	~ 27
Dipole field (T)	8.3	8.3

Table 2.1: Parameters of the Large Hadron Collider for p-p and Pb-Pb collisions [46]

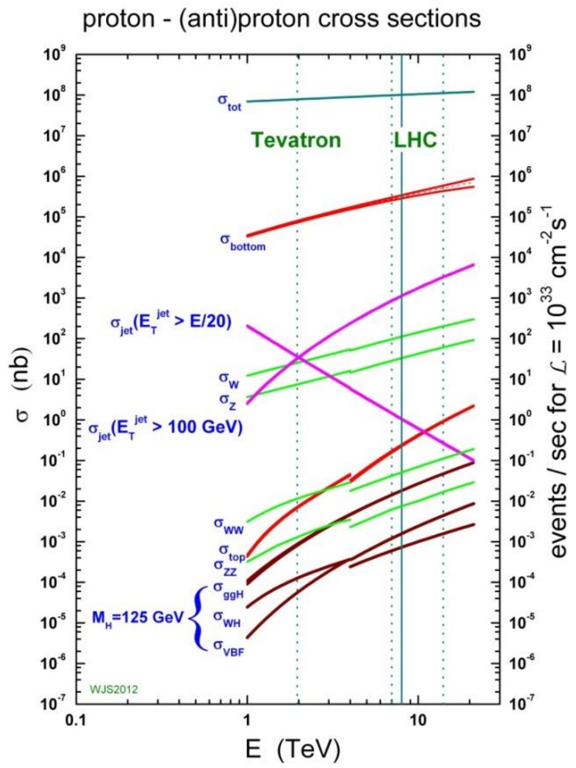

Figure 2.2: Predicted Standard Model of Particle Physics cross sections as a function of the center-of-mass energy [48]. Discontinuities at 4 TeV are due to the switch from $p\bar{p}$ to pp collisions.

In order to discover new physics, a lot of interesting processes need to be studied in detail. These processes are extremely rare, as can be seen in figure 2.2.

A collider generates number of events per second via a given process. This number is given by:

$$N = \mathcal{L}\sigma \tag{2.1}$$

where $\mathcal{L}$ is the machine luminosity, which depends only on the beam parameters, and σ is the cross section for the process being studied. Greater luminosity gives more possibility of an interesting process to occur.

For a circular collider luminosity is given by:

$$\mathcal{L} = \frac{N_1 N_2 n_b f_{rev} \gamma}{4\pi\epsilon_n \beta^*} F \tag{2.2}$$

In this formula N_1 and N_2 are the numbers of particles per bunch in each beam (particles inside the beam are accelerated into small groups, called bunches), n_b is the number of bunches per beam, f_{rev} is the revolution frequency, ϵ_n is the normalized beam emittance (a measure of how much the particles depart from the ideal trajectory), γ is the relativistic gamma factor for the particles in the beam, β^* is the beta function at the collision point (it gives the envelope for the motion of particles) and F is the luminosity reduction factor due to the crossing angle at the interaction point. In this equation, only f_{rev} and γ are determined by collider radius and particle energy, while all the other parameters may be controlled to maximize the luminosity.

2.2 LHC magnets

The LHC is built as the world's largest high-energy physics experiment. Accelerating particles into such circular path as in the collider requires a huge magnetic force to keep the beams steady. In order to achieve this and due to space constrains in the tunnel, LHC uses a new two-in-one magnet design – twin bore magnets that consists of two coils with a common infrastructure and cryostat [49].

In figure 2.3 is shown the cross section design of the main LHC dipole magnets. The two beam pipes are in the center, each with diameter of 54 mm and distance between them of 194 mm. Around the beam pipes there are superconducting coils made of superconducting NbTi cables. These cables need to be cooled down to temperatures of about 1.9 K. The cold mass of the magnet is formed by these coils, the steel collars that hold them in place and the magnetic yoke which surrounds the coils. The cold mass is insulated in a vacuum vessel immersed in superfluid Helium of 1.9 K, which is used as a coolant of the magnetic system. As a result 15 m long, 30 tons dipole magnets with a cryostat diameter of 0.914 m are built [50].

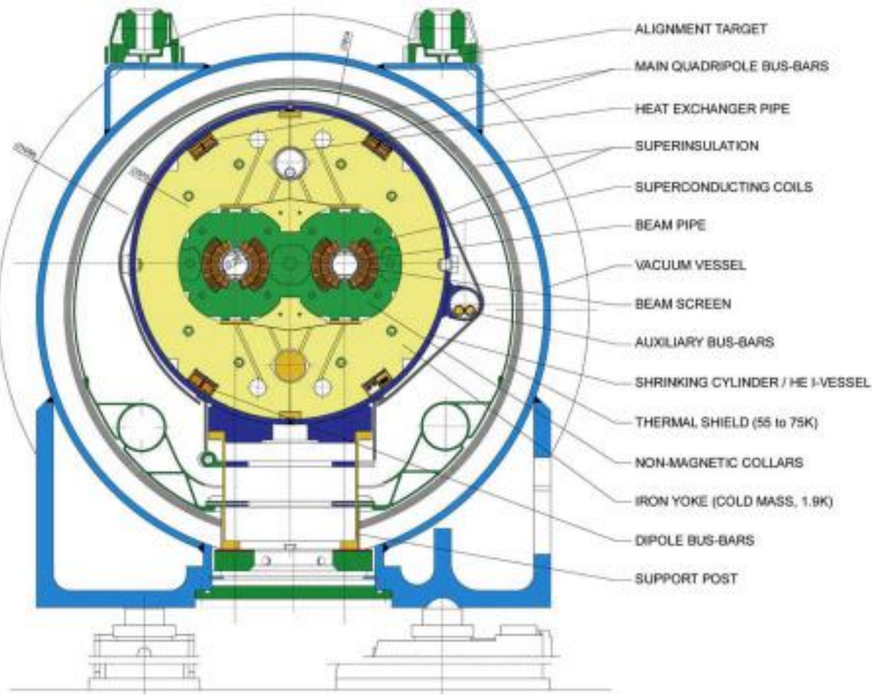

Figure 2.3: Cross section of the LHC Main Dipole in its cryostat.

These dipole magnets are used for bending the beams in order to follow the space constrains of the LHC tunnel. A circular accelerator though requires also a focusing mechanism that can keep the particles centered at the design orbit. Modern storage rings use strong focusing, which is a concept where dedicated quadrupole magnets provide field components proportional to the deviation of the particles from the design orbit. Thus due to the prevented by the Lorenz force divergent trajectories, the particles oscillate around the designed orbit while they circulate in the storage ring.

Each sector of the LHC consists of 46 series of 1 quadrupole and 3 dipole magnets. In order to focus the beam in both planes, a series of focusing and defocusing quadrupoles is arranged throughout the LHC sectors. In total there are 1232 main dipoles and 392 quadrupoles. Correcting errors in the particles trajectory is done by additional sextupole, octupole and decapole corrector magnets.

2.3 CERN Accelerator Complex

The Large Hadron Collider relies on a chain of accelerators in order to reach the designed center-of-mass energy for the particles. Each machine in this chain brings the beam to a higher energy and then injects it into the next one. The LHC is the last element in the row, where accelerating of the beam energy can go up to 7 Tev. A schematic view of the CERN accelerator complex is shown in figure 2.4.

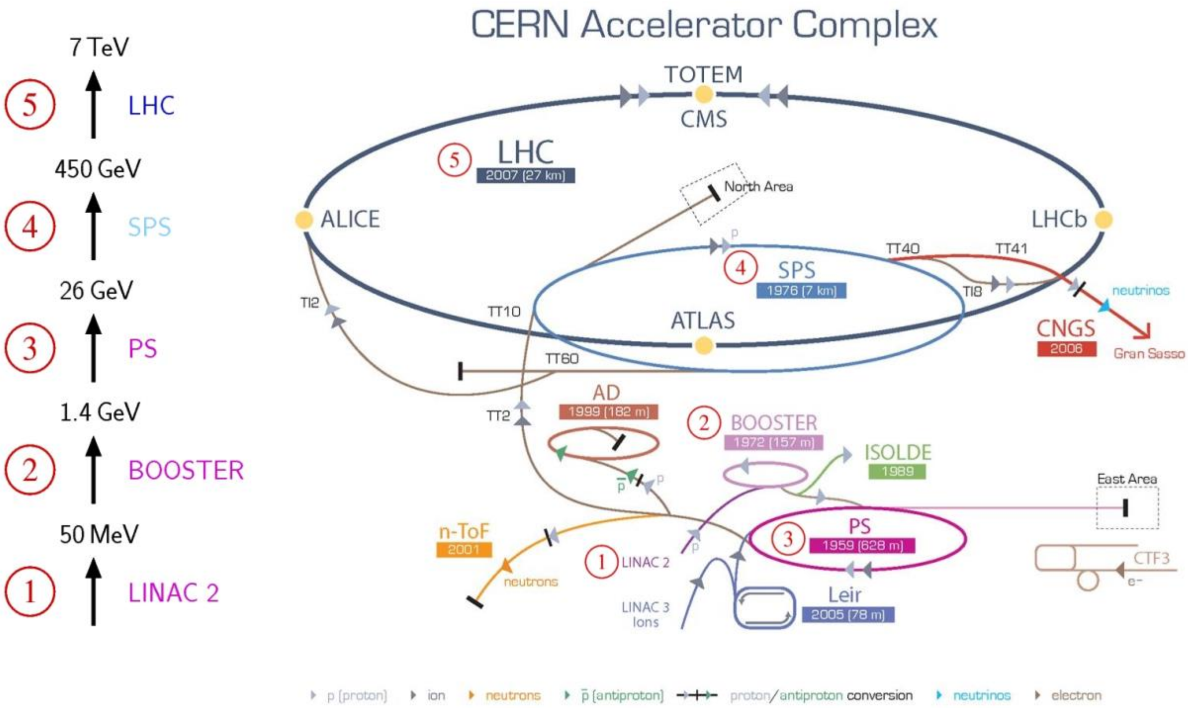

Figure 2.4: Overview of the CERN Accelerator Complex

It all starts with a bottle of hydrogen gas. The hydrogen atoms are stripped of their electrons and the protons left after this process are accelerated by a linear accelerator, LINAC2, up to energies of 50 MeV. Next is the Proton Synchrotron Booster (PSB) which accelerates this proton beam up to 1.4 GeV. After being accelerated in the following Proton Synchrotron (PS) the protons reach 25 GeV. The final acceleration step before injection into the LHC is provided by the Super Proton Synchrotron (SPS), where particles reach energies of 450 GeV. The LHC then starts accelerating the beams in two separate beam pipes for each direction until they reach maximum energy of 7 TeV. Then collisions start at the different experiments with center-of-mass energies of up to $\sqrt{s} = 14\, TeV$.

Accelerating lead ions start from a source of vaporized lead and enter LINAC3. After this they are transferred to Low Energy Ion Ring (LEIR) and then they follow the same route to maximum acceleration as protons.

2.4 LHC Experiments

Being the most sophisticated scientific experiment so far, the LHC covers a vast region of physics studies. In order to perform a detailed analysis of known physics processes and to search for new physics, at the four experimental interaction regions of the LHC are built four particle detectors, shown in figure 2.5.

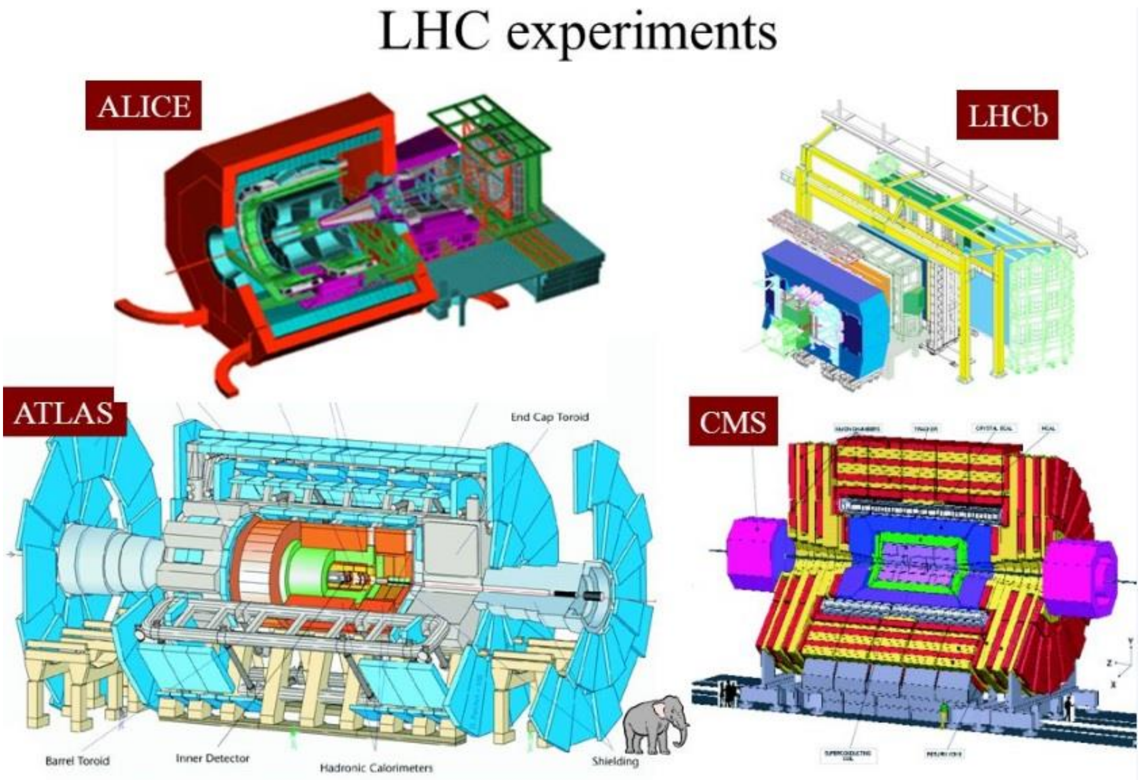

Figure 2.5: The four main experiments at the LHC – ATLAS, CMS, LHCb and ALICE

The CMS [51] and the ATLAS [52] experiments are general purpose detectors, i.e. they aim at detailed studies of the known physics and search for new physics beyond the SM. In the ALICE [53] experiment a study over lead-ion collisions is done in order to improve the understanding of the quark-gluon plasma, which is postulated to have existed during the early universe. The LHCb [54] experiment is specialized in studying of bottom-quark physics and CP violation in order to better understand the matter-antimatter asymmetry in the universe.

There are also two smaller experiments Large Hadron Collider Forward Experiment (LHCf) [55] and Total Elastic and Diffractive Cross Section Measurement (TOTEM) experiment [56], which are installed near ATLAS and CMS respectively. The first one aims at studying particle showers close to the beam pipe in order to test models of particle showers as present in astroparticle physics. The latter is measuring up to high pseudo-rapidity in order to study the total cross section of proton collisions.

3. The CMS Experiment

The Compact Muon Solenoid (CMS) [57] is one of the four main experiments at the Large Hadron Collider. It is a “general purpose” detector built to study a large spectrum of physics phenomena. Its aim is to give a detailed description of all known particles, including the latest discovered Higgs boson [16], as well as search for new physics beyond the Standard Model at the TeV energy scale. The CMS is a multi-national experiment with Collaboration of more than 4300 scientists and engineers from about 185 institutions of 41 countries.

3.1 Detector overview

The CMS detector is located in an underground cavern near the French town of Cessy. In order to cover the requirements of the LHC physics program [58], CMS is made of different sub-detectors. It is a compact 28.7 m long cylinder with an overall diameter of 15 m and total weight of about 14 500 tones.

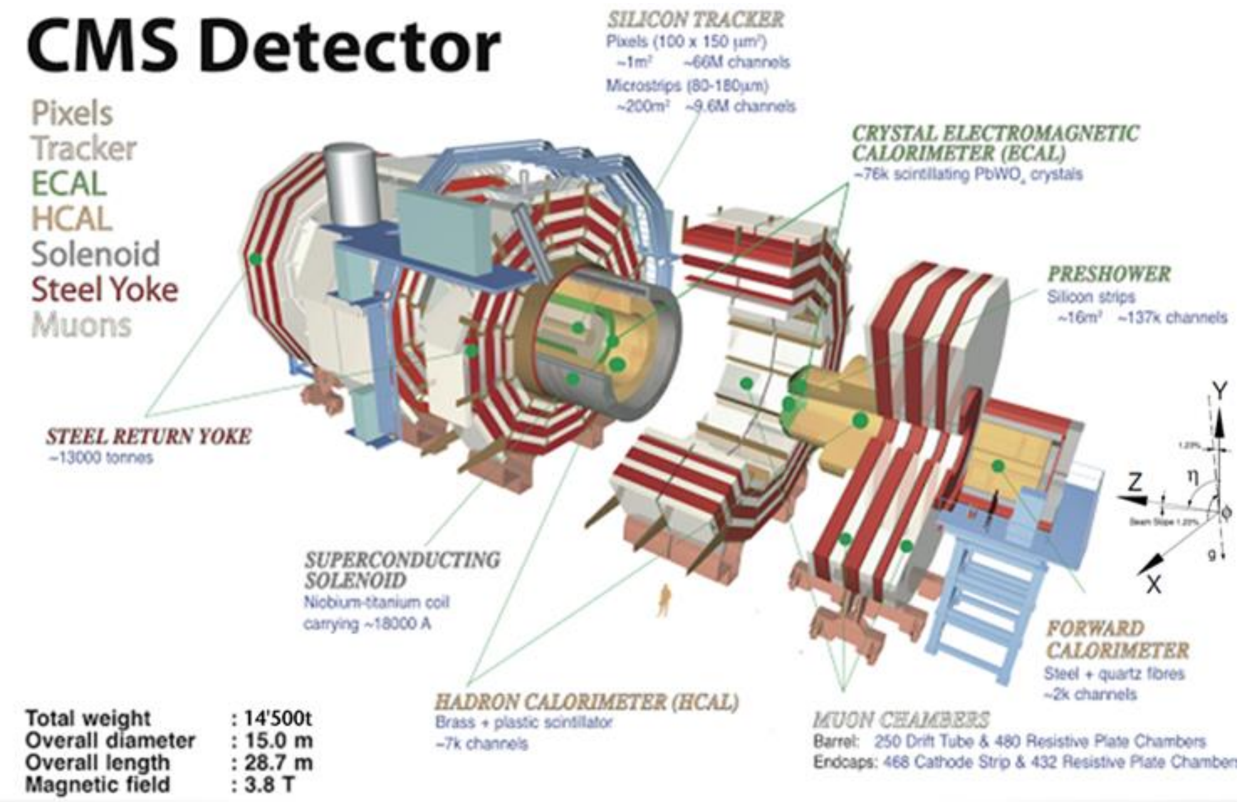

Figure 3.1: Schematic layout of the CMS experiment.

The layout of the detector is shown in figure 3.1. It is a classical one, starting with an inner tracking detector right next to the beam pipe (section 3.3). There are two calorimeters after it - an electromagnetic one (section 3.4) and a hadron one (section 3.5). The solenoid comes after the calorimeters and the last sub-detector is the muon system (section 3.6). All these layers are organized into three regions – a barrel region and two endcap regions. The Barrel consists of cylindrical layers around the beam pipe, while the Endcaps are made of disks which close the barrel region.

The cylindrical shape of the detector is dictated by its main feature – a super-conducting solenoid magnet (section 3.2) with length of 12.9 m and inner diameter of 6 m. The solenoid is installed in the barrel region and can reach a magnetic field of 3.8 T. It is used for unambiguous determination of the sign of muons with a momentum up to 1 TeV. In order to achieve this, the muon system, which is placed outside the solenoid, should have a very high performance with good muon identification and momentum resolution over a wide range of momenta and angles.

The tracker detector ensures good charged particle momentum resolution and reconstruction efficiency. The electromagnetic calorimeter gives good energy resolution for electrons and photons and the hadron calorimeter measures the energy of charged and neutral hadrons. Both calorimeters are hermetic.

The CMS experiment uses a right-handed coordinate system with point of origin the interaction point in the center of the detector where the particles collide (figure 3.1). It is oriented so that the x-axis is pointing radially inwards, towards the center of the LHC, the y-axis points upwards and the z-axis is parallel to the beam direction. The x-y plane is called transverse plane and the azimuthal angle ϕ is measured with respect to the x-axis in it. The polar angle θ is defined with respect to the z-axis, i.e. it is the angle between the particle three-momentum and the positive direction of the beam axis. The pseudorapidity η is defined using polar angle θ:

$$\eta = -ln\left(tan\frac{\theta}{2}\right) \tag{3.1}$$

Along the z-direction the CMS detector is divided into five wheels, which form the barrel region and eight disks, which constitute the forward regions, i.e. the positive and negative endcaps.

The CMS experiment collects a huge amount of data, which needs to be sorted in some way. The trigger system does this on a two-level basis, explained in section 3.7. The first level is a hardware trigger (L1), and the second one is a high-level software trigger (HLT).

Detailed description of the CMS experiment and its sub-detectors can be found in [59-61].

3.2 CMS Solenoid

The superconducting solenoid of the CMS experiment [62] is used for achieving accurate measurements on the transverse momentum p_T for charged particles crossing the detector. Its magnetic field is bending the paths of the particles coming out of the high-energy collisions at the LHC. The more momentum a particle has, the less curved its path is. Thus, tracing the particles path gives a measure of the momentum.

The CMS magnet is 12.9 m long with inner diameter of 6 m and produces a magnetic field of 3.8 T. This makes it the largest superconducting magnet ever built. It is made of a stabilized reinforced NbTi superconducting wire coils that produce a uniform magnetic field when electricity flows through them and is cooled down to -268.5 ˚C, which is just a degree warmer than outer space.

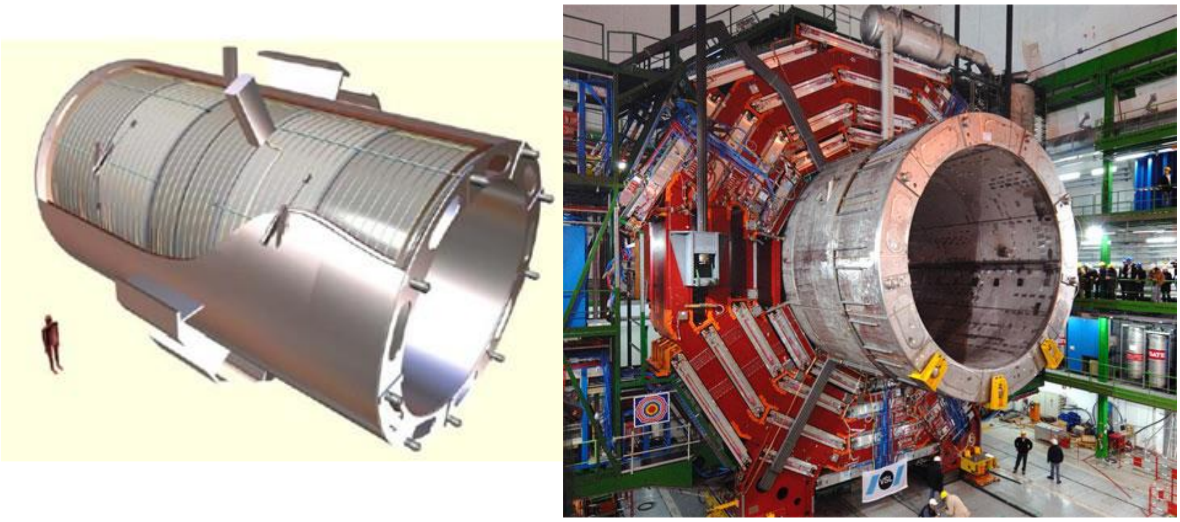

Figure 3.2: A schematic representation of the CMS solenoid (left) and a view of the magnet and the return yoke with muon chambers installed (right).

The magnetic field is closed through a 12 500 tones steel return yoke in which the muon detectors are placed. The inner coil radius is big enough so that the inner tracker and the full calorimetry can fit inside. In figure 3.2 a schematic view of the CMS solenoid is shown as well as the steel return yoke and muon chambers around the magnet. Supporting all sub-detectors makes the CMS magnet the real backbone of the CMS experiment.

3.3 Tracker system

The innermost sub-detector in the CMS experiment is the tracking system (Tracker) [63, 64]. The Tracker is a very sophisticated silicon-based detector, designed for precise measuring of charged particles trajectories, as well as precise reconstructing of secondary vertices. It is a system of two sub-detectors with independent cooling, powering and read-out schemes – inner silicon pixel detector and outer silicon strip detector. The Tracker has an overall length of 5.4 m and an outer diameter of 2.4 m. Overview of the CMS tracker layout is shown in figure 3.3, with its subsystems – Pixel, Tracker Inner Barrel (TIB) and Tracker Inner Disks (TID), Tracker Outer Barrel (TOB) and Tracker Endcaps (TEC).

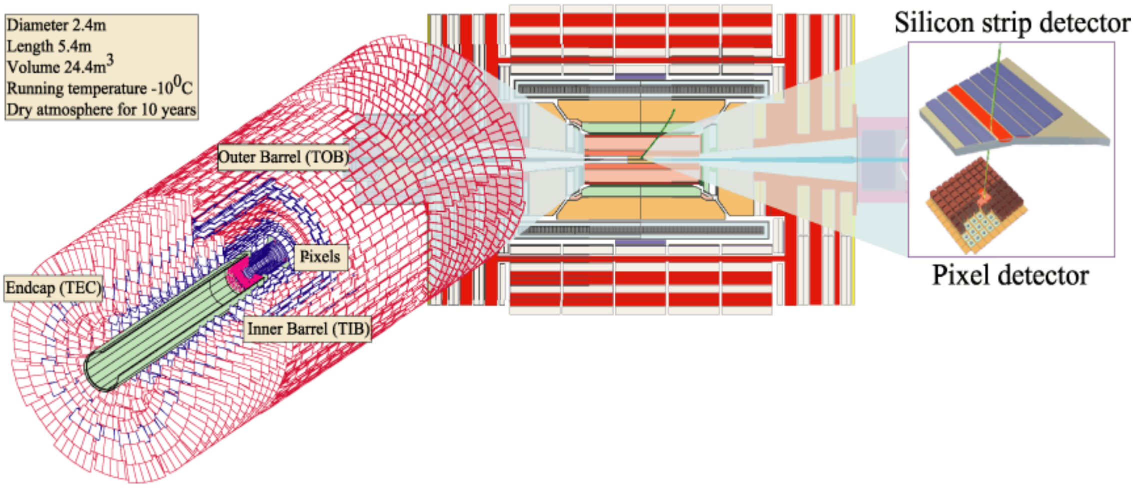

Figure 3.3: Overview of the inner tracking system of the CMS experiment.

The inner pixel detector [65] is installed within a distance of 20 cm from the beam pipe. It is designed to provide four high precision three-dimensional points on track trajectories. The Pixel detector has an active area of about 1.1 m^2, which is arranged in four cylindrical barrel layers and three endcap layers on each side of the barrel Barrel layers are situated at 3, 6.8, 10.2 and 16 cm surrounding the interaction point, while the endcap ones are at 24.1, 34.5 and 46.5 cm from the interaction point. A total number of 66 million pixel sensors [66] of size 100 μm by 150 μm are implemented into 285 mm tick n-type bulk and p-type back side, shown in figure 3.4. They are oriented with the smaller pitch in the azimuthal direction in the barrel and in the radial direction in the disks [67].

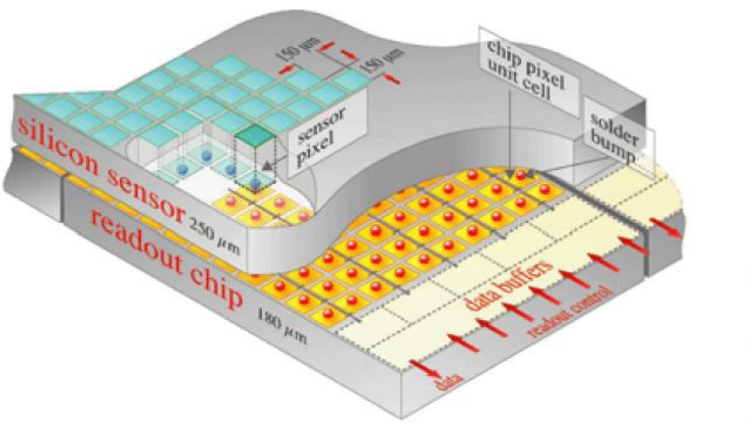

Figure 3.4: Schematic representation of the CMS silicon pixel detector.

Signals from these sensors are read by 15840 readout chips (ROC), each reading an array of 52 x 80 pixels. The data from the modules, in which the ROCs are arranged, is transmitted via 1312 readout links. The pixel system provides efficient four-hit coverage in the entire region of pseudorapidity $0 < \eta < 2.5$.

The CMS silicone strip tracker [68] is the largest silicon tracker ever built with more than 10 million detector channels, 15 000 silicon modules and a total active area of about 200 m^2. It is placed around the pixel detector and covers the region up to 116 cm from the beam pipe, along the distance of 5.6 m. It is divided into four main subsystems shown in figure 3.5 – the Tracker Inner Barrel (TIB), composed of four barrel layers, the Tracker Outer Barrel (TOB), having six barrel layers, and on each side of the barrel region, the Tracker Inner Disks (TID) and the Tracker EndCaps (TEC), each with three and nine disks respectively.

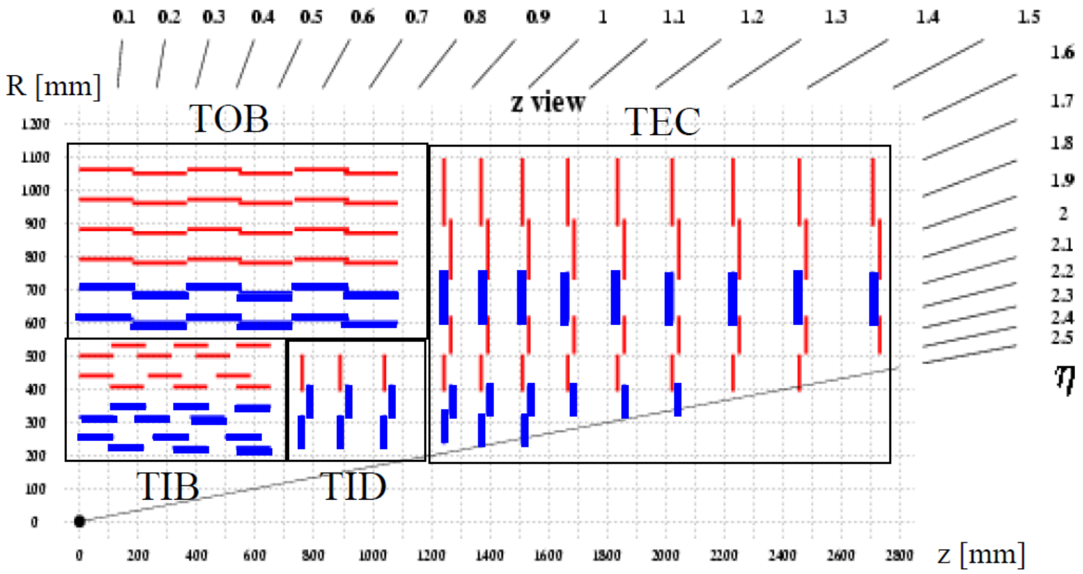

Figure 3.5: Cross-section of one quarter of the tracker in the longitudinal view. Thick lines represent double-sided modules, while the thin ones are for the single-sided modules [69]

The TIB and TID are composed of 320 µm tick silicon sensors. The strips are oriented parallel to the beam axis in the barrel with strip pitch ranging from 80 µm to 120 µm, while in the disks strips are oriented radially with strip pitch from 100 µm to 141 µm. Both TIB and TID are enclosed within the TOB, which consists of 500 µm tick microchip sensors with strip pitch of 122 µm in the first four layers and 183 µm in the last two ones. The nine disks of the TEC are instrumented with up to seven rings of silicon detectors with sensor thickness of 320 µm in the inner four rings and 500 µm in the outer three rings. The average strip pitch varies from 97 µm to 184 µm. Double-sided modules (two single-sided modules mounted back to back with a stereo angle of 100 µm) are used in the inner two layers of the TIB and TOB and the inner two rings of the TID and TEC, as well as in the fifth ring of the TEC. They enable the proper measurement of the orthogonal coordinate. The silicon strip tracker provides two-coordinate measurements in at least ~4 hits for the pseudorapidity range $|\eta| < 2.4$.

3.4 Electromagnetic Calorimeter

The energy of photons and electrons is measured in the CMS Electromagnetic Calorimeter (ECAL) [70]. The ECAL has 75,848 crystals arranged in a central barrel section (EB), with pseudorapidity coverage up to η = 1.48, closed by two endcaps (EE), extending coverage up to η =3.0. The $PbWO_4$ crystals have high density (ρ = 8.28 g/cm^3), small Moliere radius (r_M = 2.2 cm) and short radiation length (X_0 = 0.89 cm) and thus allow fine granularity and of the calorimeter. The $PbWO_4$ crystals have a good radiation resistivity. The scintillation light in the barrel region is detected by avalanche photodiodes (APDs), while in the endcap region vacuum phototriodes (VPTs) [71] are used, as shown in figure 3.6.

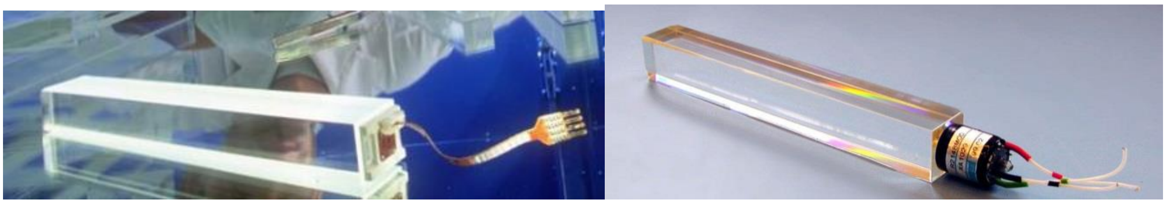

Figure 3.6: $PbWO_4$ ECAL crystals with photo-detectors attached – a barrel crystal with APD capsule (left) and an endcap crystal with a VPT (right).

The barrel section (EB) covers the pseudorapidity range |η| < 1.479 and has an inner radius of 129 cm. It is structured in 36 supermodules, each composed by 20x85 crystals. Each crystal is 230 mm long, which corresponds to 25.8 radiation lengths (X_0) and covers approximately 0.0174x0.0174 in η-ϕ or a front-face cross section of 22x22 mm^2. In order to avoid cracks, crystals are mounted slightly turned, so that the crystal axes make a 3-degree angle with respect to the direction of the nominal interaction point in both the azimuthal ϕ and η projections.

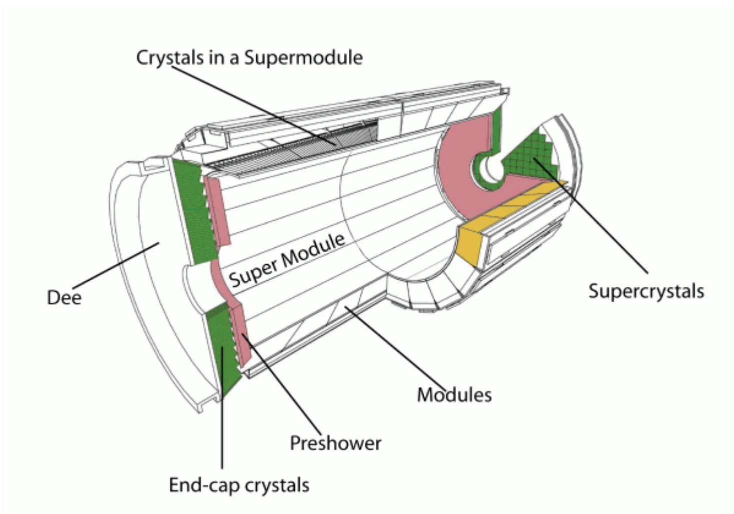

Figure 3.7: Schematic view of the CMS ECAL structure – Barrel (yellow), Endcap (green) and Preshower (orange).

The endcap (EE) sections have four half-disks called "*Dees*", each holding 3662 crystals. They cover the pseudorapidity range 1.479 < |η| < 3.0 with distance from the interaction point to the front face of 3.15 m. The front face cross section of the crystals is 28.62x28.62 mm^2 and their length is 220 mm, corresponding to 24.7 X_0. They are arranged in a quasi-projective geometry focusing at a point 1.3 m farther than the nominal interaction point along the beam line, and with off-pointing angles between 2° and 8°. A schematic view of the ECAL layout is shown in figure 3.7.

In front of the two endcaps is installed the Preshower (PS) [72]. It is designed to improve the resolution in the forward region in the range 1.653 < |η| < 2.6 and provide information on the electrons identification against minimum ionizing particles, as well as identification of neutral pions decaying into two photons. The Preshower is 20 cm thick and consists of two layers – silicon strip sensors, which are interleaved with 3 X_0 lead radiators (2 X_0 in front of the first silicone plane and 1 X_0 behind it). The lead initiates electromagnetic showers from incoming photons/electrons, while the silicon strip sensors measure the transverse shower profiles and the deposited energy. The strips in the two planes are oriented orthogonally, while the lead planes have the same orientation as the ECAL crystals.

3.5 Hadron Calorimeter

The CMS Calorimeter is completed by adding the Hadron Calorimeter to the ECAL. This combine system allows estimating the amount of missing transverse energy of each event, as well as measuring the direction and energy of hadronic jets over a wide range of energies [73].

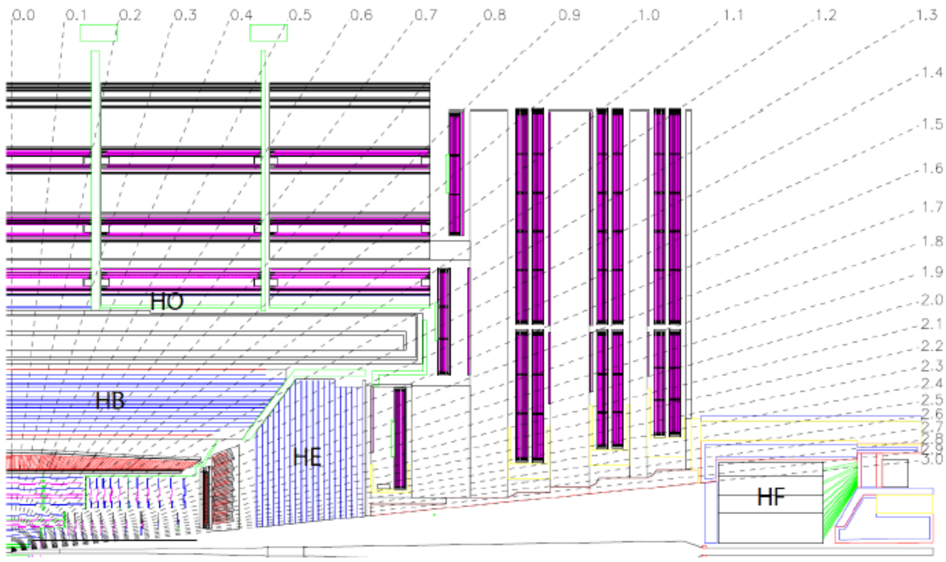

Figure 3.8: Schematic view of the HCAL sub-detectors.

The CMS HCAL [73] is a very hermetic compact sampled system located between the ECAL and the magnet coil. The cascade of secondary particles for high energy hadrons initiated in it is achieved by using alternating layers of non-magnetic brass absorbers and fluorescent scintillators. The brass absorbers are chosen for their non-magnetic nature and short interaction length λ_I. A schematic view of all HCAL parts is shown in figure 3.8.

There are four sub-detectors building up the HCAL – the barrel part (HB), two endcap detectors (HE), the outer calorimeter (HO) and the forward calorimeters (HF). The detecting scintillator tiles have a segmentation of $\Delta\eta \times \Delta\phi = 0.087 \times 0.087$ at central region ($|\eta| < 1.74$) and 0.09×0.174 to 0.35×0.174 at forward region ($1.74 < |\eta| < 3.0$). The HB covers pseudorapidity $|\eta| < 1.3$, while the endcaps HE cover $1.3 < |\eta| < 3.0$. The HB and HE scintillator tiles are grouped in towers, which via wavelength-shifting fibers are read out by Hybrid photodiodes (HPDs). Passing particle's energy is measured with respect to the total amount of collected light over the layers within a given tower. The HCAL barrel and endcap sub-detectors are shown in figure 3.9.


Figure 3.9: Photographs of the CMS HCAL – barrel HB (left) and endcap HE (right).

The outer calorimeter HO is used to overcome the not sufficient stopping power caused by the limited space in the barrel region. It is placed in front of the iron return yoke, consists of five wheels and also covers $|\eta| < 1.3$ as HB. The central wheel has two layers of scintillators surrounding the absorber (iron), while the other four wheels are only scintillators, using the magnet coil as an absorber. The readout and segmentation of the HO are the same as the HBs towers which allows forming of combined HCAL towers. The minimum material thickness (11.8 λ_I) achieved in the calorimeter is a combination from the ECAL, the HCAL, the solenoid, the support structure and the first layer of the iron return yoke.

The forward calorimeters HF provide fast collection of Cherenkov light. They are installed behind the HEs at a distance of 11.2 m from the interaction point to the front face of the detectors and cover the pseudorapidity range of $2.9 < |\eta| < 5.2$. They consist of radiation-hard quartz fibers embedded in iron absorbers. The use of long fibers running over the full depth of the absorber (165 cm, ~10 λ_I) along with short fibers, which start at a 22cm depth from the front of the detector, segments the HF longitudinally. This unique design with different lengths of the fibers makes it possible to distinguish electromagnetic showers from hadronic ones [74]. Radiation hard photomultiplier tubes (PMTs) are used to detect the collected light.

3.6 Muon System

One of the processes of central importance in the CMS experiment is muon detection. The clean signature, which muons provide in detectors, is used for identifying and studying of interesting processes over the complicated background rate at the LHC [75]. This implies a robust and redundant muon spectrometer providing efficient muon reconstruction.

The CMS muon system [76] has a few primary functions – muon identification, transverse momentum (p_T) measurement, muon triggering and charge determination. The magnetic flux-return yoke serves as a hadron absorber, cleaning up the muon signal for better muon identification, while the high magnetic field enables good muon momentum resolution, both in the trigger and the reconstruction. The muon system is designed to identify the muons produced in many SM processes, like top quark, the Higgs boson decay, as well as W and Z decays which follow after it [77]. It has a good p_T resolution of around 9% at 200 GeV/c and between 15% to 40% at 1 TeV/c. Combined with the CMS tracker, the muon system achieves a global resolution of 1% at low p_T and about 5% at 1 TeV/c [78].

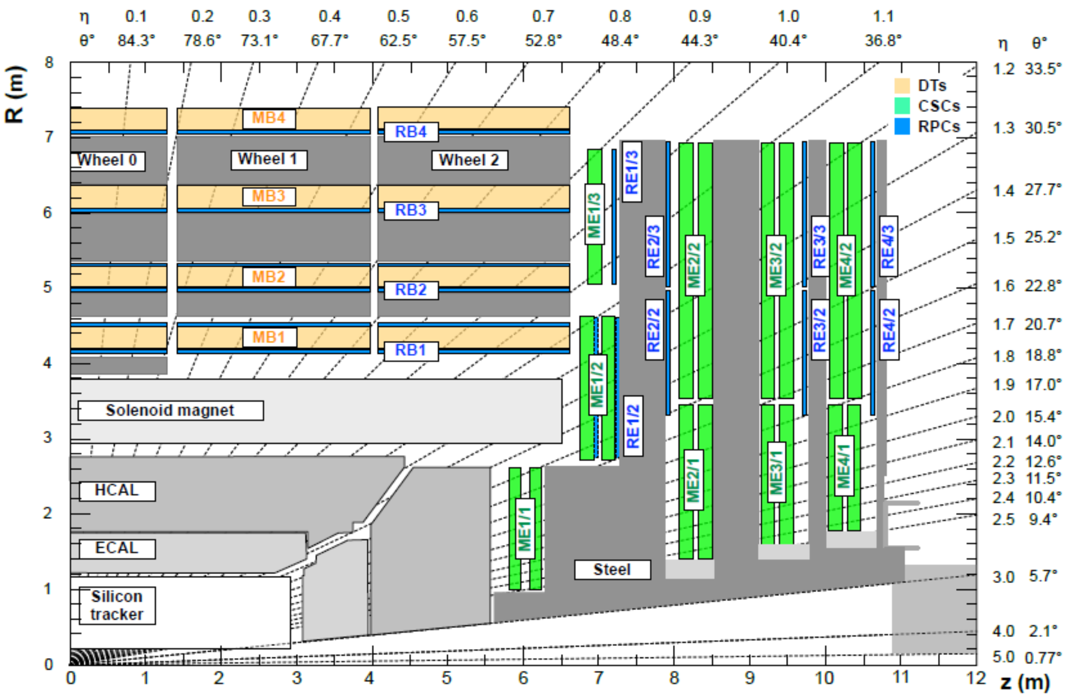

Figure 3.10: R-z cross section of a quadrant of the CMS muon system, showing DT (yellow), CSC (green) and RPC chambers (light blue). The interaction point is at the lower left coner.

On the quest to identify muons, the CMS muon system uses three different gaseous detector technologies – Drift Tubes (DTs) in the barrel region ($|\eta| < 1.2$), Cathode Strip Chambers (CSCs) in the endcap region ($0.9 < |\eta| < 2.4$) and Resistive Plate Chambers (RPCs) both in barrel and endcap regions ($1.2 < |\eta| < 1.6$). Both the DT and CSC systems provide precise space and time measurement, while the RPC system provides an independent trigger measurement with fast time response of the order of few ns, but not so accurate position resolution. A schematic view of the CMS muon system is shown in figure 3.10.

The Barrel follows the cylindrical shape of the solenoid and is divided into five mechanically independent wheels – Wheel 0, Wheel ±1 and Wheel ±2. Each wheel is sub-divided in twelve sectors, each covering an azimuthal angle $\phi = 30°$ and every sector has four detector stations integrated in the magnet return yoke. The Endcaps are planar and have four disks, called stations (ME1, ME2, ME3, ME4), closing the magnet circuit of CMS and the barrel on each side. Each endcap station has 36 sectors covering an azimuthal angle $\phi = 10°$.

3.6.1 Drift Tubes

The drift tube system [79] is part of the CMS muon barrel, covering the region $|\eta| < 1.2$. It consists of 4 coaxial stations (MB1 to MB4), forming concentric wheels (Wheel 0, Wheel±1, Wheel ±2) which are segmented in 12 sectors around the beam line. The system has a total number of 250 DT chambers. The smallest independent unit of the DT design is the Super Layer (SL) - each chamber is made of 3 SLs with 4 layers of staggered drift cells each. Schematic view of a DT chamber is given in figure 3.11(b). The wires in the innermost and outermost SLs are parallel to the beam line and provide a track measurement in the CMS bending plane ($r – \phi$ plane). The inner SL has its wires orthogonal to the beam line and thus measure the hits position in the $r – z$ plane. This inner SL is not present in the fourth station (MB4), which is located outside the iron return yoke and measures only the hit position with respect to its ϕ coordinate. This DT configuration results in two measurements in ϕ and one measurement in z position per station for each muon coming from the interaction point.

The Drift Tube Chambers (DTs) are gaseous detectors and their working principle is based on the produced ionization in the gas volume of the detector caused by passing of charged particles. DTs are built with 13 x 42 mm^2 rectangular drift cells, shown in figure 3.11(a). For cathodes are used two 50 μm thick aluminum electrodes on the short edges of the drift cell at 1.8 kV, while the anode is a 50 μm in diameter gold-plaited stainless steel wire at 3.6 kV. The cells are located along the full length ~ 2.5 m or width of the DT chambers with distance between two consecutive anode wires of 42 mm. The cells have an offset of half-cell with respect to the upper and lower neighbor cells and are separated by 1 mm thick aluminum.

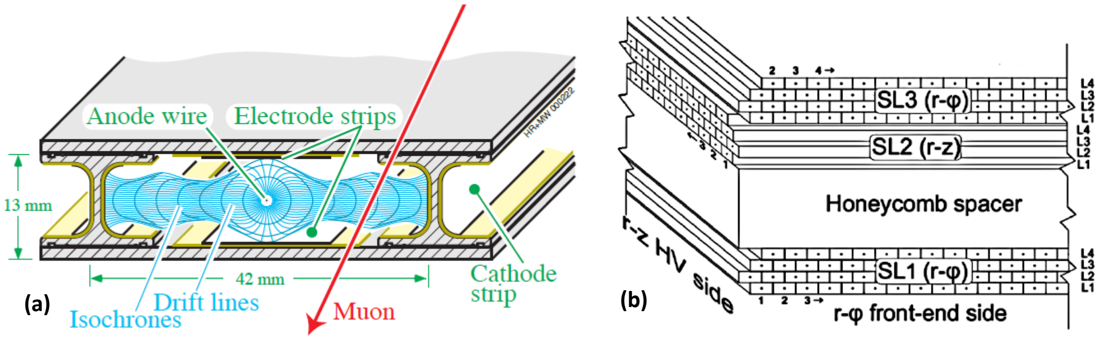

Figure 3.11: Transverse view of a DT cell (a) and schematics of a DT chamber (b) [80].

When passing, muons create electrons and ions, which drift towards and away from the anode wire respectively. Once the electrons reach the strong electric field close to the wire, an avalanche is created and it is transformed to an electrical signal on the anode. The maximum drift time in each DT chamber for the working gas mixture of 85% Ar and 15% CO_2 is ~ 400 ns. The drift velocity in the DT cells is approximately constant, which relates the passing muon position to the time measurement. The spatial resolution at the cell level is in the order of 250 μm, while combining the information from the different layers allows the reconstruction of track segments with a resolution of 100 μm. The DT time resolution is around 5 ns.

3.6.2 Cathode Strip Chambers

The Cathode Strip Chambers (CSCs) System [81] consists of 540 gaseous particle detectors integrated in four layers on each Endcap - ME1, ME2, ME3 and ME4, covering the pseudorapidity region of $0.9 < |\eta| < 2.4$ [82], shown in figure 3.10. Each layer has up to three rings of trapezoidal chambers with two different sizes – covering either 10° or 20° in azimuthal angle ϕ. A schematic view of a CSC chamber and its working principle is given in figure 3.12.

Each CMS CSC is a multi-wire proportional chamber comprised of seven copper-clad panels, forming six gas gaps layers. The gas gaps are 6 mm for the ME1/1 chambers and 9.5 mm for the rest of the chambers. On each copper panel, cathode strips with different width (3 – 16 mm) are etched. They are used for measuring of the azimuthal coordinate of passing muons which is crucial for the proper estimation of their transverse momentum. Anode wires are aligned between each cathode strips layer. They are oriented perpendicular to the strips and provide the radial coordinate of the passing muons. The wires are held at a potential of 2.9 – 3.6 kV, and the gaps are filled with the CSC standard gas mixture – 50% CO_2, 40% Ar and 10% CF_4.

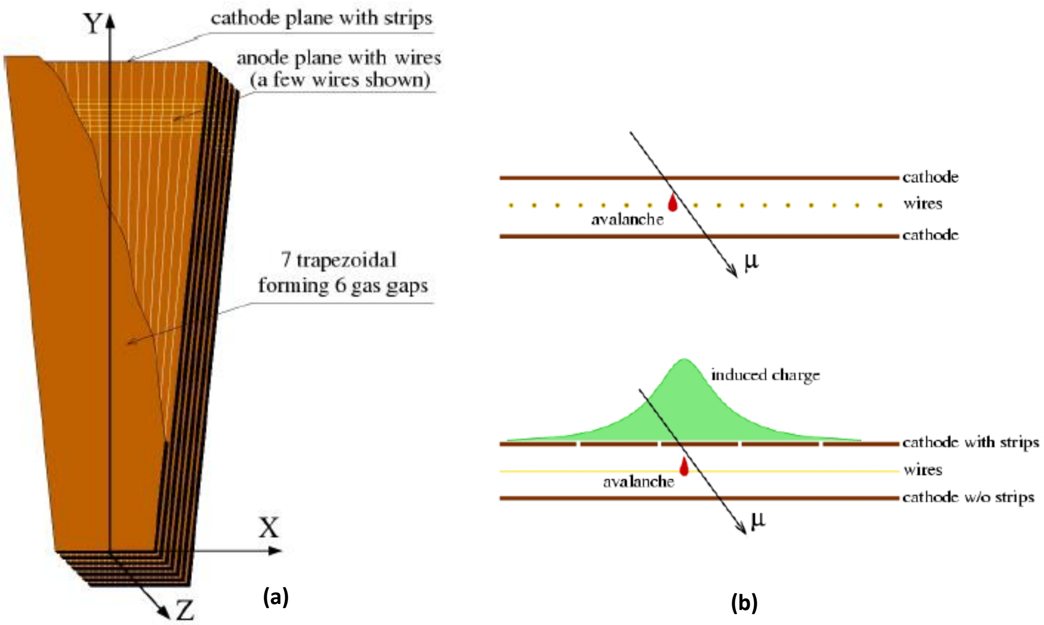

Figure 3.12: Schematic view of a CMS Cathode Strip Chamber with local chamber coordinates (a) and an illustration on the CSC working principle (b) [83].

The CSC operation principle is shown in figure 3.12(b). A muon passing through a gas gap causes an electron avalanche. It produces a signal on the anode wires and induces a distributed charge on the cathode strips.

CMS CSCs have strip pitch from 8.4 to 16 mm and distance between wires of 2.5 to 3.16 mm depending on their location. They can provide good spatial resolution of 75 to 150 μm.

3.6.3 Resistive Plate Chambers

The Resistive Plate Chambers (RPCs) [84] are gaseous detectors, which complement the CMS muon system both in the barrel (along with DTs) and the endcap regions (along with CSCs), covering the pseudorapidity range of $|\eta| < 1.9$. There are 1056 RPC detectors which cover an active area of more than 3500 m^2.

The barrel region of the RPC system has 480 RPCs, distributed equally among 5 wheels (Wheel 0, Wheel ±1, Wheel ±2) around the beam pipe. According to the direction of ϕ (azimuthal angle), each wheel is divided into 12 sectors (S01-S12), where the first sector is aligned to the positive X-axis, see figure 3.10. Further to the trigger requirements, the chambers are subdivided with respect to pseudorapidity in 2 or 3 partitions, called rolls [76]. This geometry difference is driven by the need to have adjustable trigger on muons with different transverse momentum pT. The endcap region has 576 chambers distributed in 8 disks (4 for the positive side of interaction and 4 for the negative side of interaction), where chambers are trapezoidal, covering 10◦ of the azimuthal angle and are arranged in two concentric rings. Each chamber is indicated as a segment CH01 through CH36 within a ring. Segment CH01 lays on the positive X-axis direction and the numbering proceeds anti-clockwise in respect to the interaction point. Endcap RPCs are divided in η in 3 rolls. The readout strips have different geometry depending on which part of the system they are in – the barrel chambers have rectangular shaped strips, while in the endcap chambers their shape is trapezoidal. The pitch of the strips depends on the distance to the beam pipe varying from 1.5 cm for the innermost stations to 4 cm for the outermost stations.

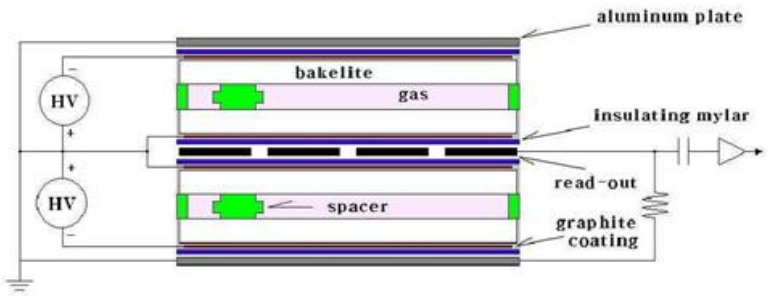

Figure 3.13: Schematics of a double-gap RPC chamber.

The RPC chambers rely on High Pressure Laminate (HPL) Bakelite gaps with 2 mm gas space between the plates, organized in a double gap design with a copper strip readout panel placed in between [85]. A schematic view of an RPC chamber is given in figure 3.13. The HPL sheets resistivity is of the order of $2 - 5 \times 10^{10}$ Ωcm. The standard CMS RPC gas mixture is composed of 95.2% $C_2H_2F_4$, 4.5% iC_4H_{10} and 0.3% SF_6. The RPCs operate in avalanche mode in order to cope with high background rates, while ensuring precise bunch crossing assignment and excellent time resolution of ~2 ns. A more detailed description of the RPC system is given in the next chapter.

3.7 Trigger and Data Acquisition

At the design LHC luminosity of 10^{34} $cm^{-2}s^{-1}$ every bunch-crossing occur approximately 22 proton-proton events, corresponding to a data rate of ~40 TB/s. This data needs to be analyzed, selected and collected by the LHC experiments (see sec. 2.4), but such data rate is many orders of magnitude higher than the available storage capability. Therefore a serious reduction of the collected data is required until it reaches the maximum accepted rate of ~100 MB/s, corresponding to ~100 Hz.

The CMS experiment uses a two-step trigger system in the process of data reduction – Level 1 Trigger (L1) and High Level Trigger (HLT) [86], shown in figure 3.14. The first step L1 trigger reduces the events rate to less than 100 kHz, while the second step HLT trigger is giving the final output data rate of about 100 Hz [87].

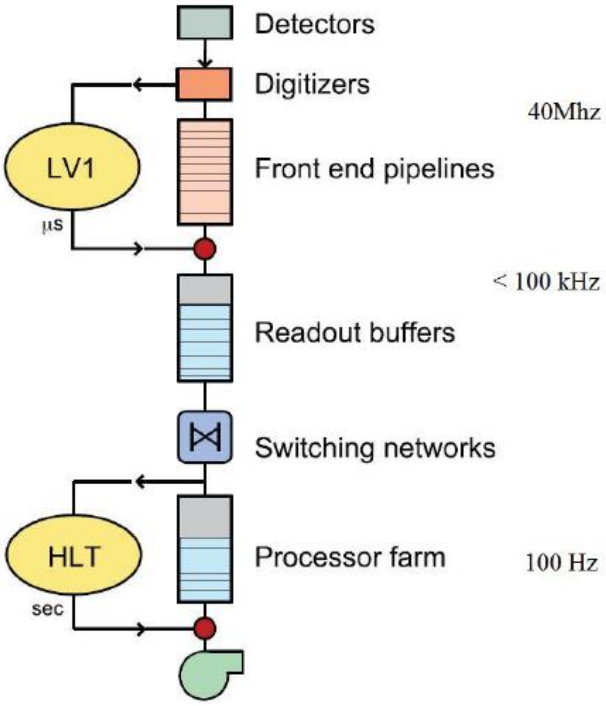

Figure 3.14: Data flow in the CMS Trigger system with the different trigger levels and event rates shown.

3.7.1 Level 1 Trigger

The Level 1 trigger [86] is a system of hardware based online triggers, which decide whether or not to save the experimental data directly after it is recorded by the experiment. This decision is made within 3 μs after each collision, since data is saved in a buffer which is overwritten after this period. The event rate after L1 triggers is reduced from 40 MHz to 100 kHz, which is low enough for the data to be saved and transferred to a computer farm. The L1 triggers select events with interesting signatures based on the presence of local objects like photons, electrons, muons and jets, as well as global sums of E_T and missing E_T. They use information from the calorimeters and the muon systems in given elements of $\eta - \phi$ space, called trigger towers.

The three major subsystems implemented in the L1 Trigger System are the Calorimeter Trigger, the Muon Trigger and the Global Trigger, shown in figure 3.15. The Calorimeter Trigger [88] preserves the local energy sums from the ECAL, HCAL and HF individual readout towers, i.e. the Trigger Primitive Generator (TPG) circuits. These sums are accompanied by a fine-grain bit for the ECAL, which indicates the transverse extent of the electromagnetic energy deposit, i.e. if a large fraction of the summed energy comes from 2 out of 5 adjacent (η) strips. The TPG information is then transferred to the Regional Calorimeter Trigger (RCT), which identifies electrons, γs, τs and hadron jets candidates. Finally these trigger primitives along with sums of transverse energy are sent to the Global Calorimeter Trigger (GCT), where the best four candidates from each category go to the Global Trigger.

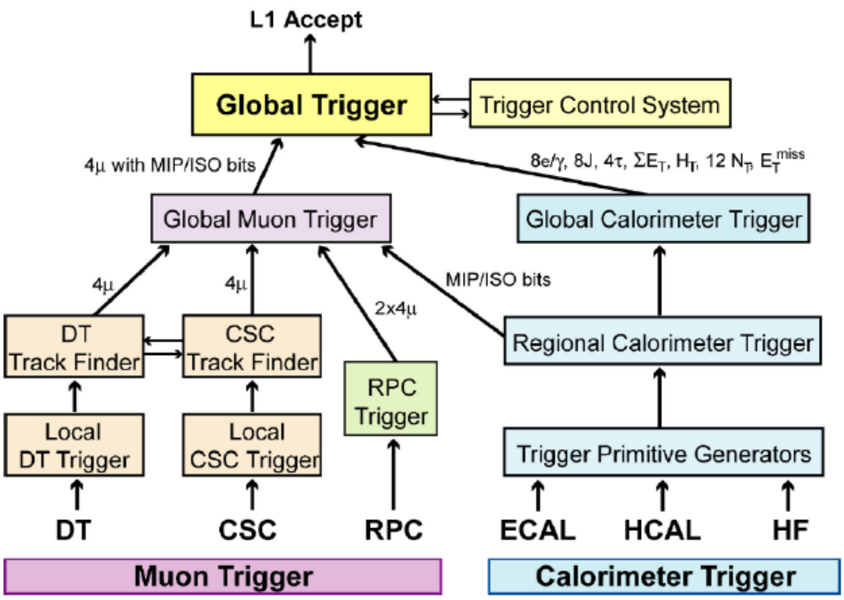

Figure 3.15: Architecture of the Level 1 Trigger [66].

The Muon Trigger uses information from DT, CSC and RPC local triggers to drop events with low quality muons. The trigger information from the different muon chambers comes in different scales. The Global Muon Trigger (GMT) major task is to combine and convert the information from all three systems into the same η, ϕ and p_T scale in order to correlate the muon tracks. Finally GMT estimates only the 4 best muon objects and sends them to the L1 Global Trigger [89].

The L1 Global Trigger based on programmed logical combinations holds a time match on the information from both GCT and GMT and decides to accept or reject these events.

3.7.2 High Level Trigger

The second stage of the Trigger system is the High Level Trigger (HLT) [87]. All events passing the L11 trigger are transferred to a computer farm where the software based offline trigger filters further the events rate by using different reconstruction algorithms. Only events that pass at least one of the HLT criteria are kept for permanent storage and thus the event rate is reduced from 100 kHz to 100 Hz, which is the accepted rate to be stored on tape.

The HLT algorithms execute complex physics selection on a farm of commercial processors in order to accept only the events with most interesting physics content. Each processor has access to the full raw L1 data and analyzes one event with a total processing time of ~1 s/event. The minimal processing time is guaranteed by three basic reconstruction concepts of the HLT software. Trigger objects are reconstructed only if they are needed in the trigger decision. Fast algorithms help avoiding unnecessary calculations by rejecting events as early as possible by using several stages of virtual trigger levels for selection and reconstruction. There is no limitation on the number of employed algorithms or the number of virtual levels, the only exception being the CPU time. It is accepted that Level 2 Trigger is used for a first HLT stage based on data from the calorimeters and muon systems, while the algorithms using the tracker data are referred to as Level 3 Trigger. The HLT algorithms are used to process only parts of detector information, which contains trigger objects found in the preceding trigger levels. Reconstruction is aborted in case the result cannot be altered by any further calculations.

The information coming out of the HLT constitutes primary data sets, where event have different HLT paths according to the kind of physics they may content. This information is originally stored in CERN Tier0 of the Worldwide LHC Computing Grid (WLCG) network [90] and later is distributed around the entire network for an easy access for the CMS collaboration.

3.7.3 Data Acquisition System

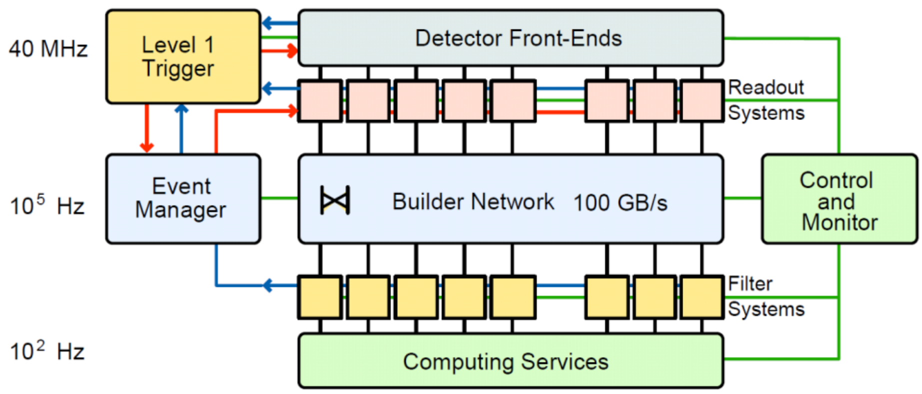

Figure 3.16: Schematics view of the general architecture of the CMS DAQ system.

The Data Acquisition (DAQ) System [84] read the output of the L1 trigger and merges in a complete event all the event fragments from different front-end devices. After this it passes events to the Event Filter Farm where the HLT algorithms are run. The general architecture of the DAQ system is shown in figure 3.16.

The Detector Front-End modules are used for storing digitized data from the front-end electronics until a L1 trigger accept signal is received. Data is held in pipelined memories. Then, based on the L1 trigger decision, data is transferred to front-end Readout Units (RU). The data flow in the RU builders is coordinated by the Event Manager. It also keeps track of the RUs memory occupancy. The readout builder network is capable of supplying 800 GB/s data flow to the filter systems. It is used to send event fragments to the builder units, where each event is defragmented before being transferred to the HLT for further processing.

4. Resistive Plate Chambers for the CMS experiment

This chapter gives an overview of the Resistive Plate Chambers. Their working principle, design and configuration inside the CMS experiment are also described. Main requirements for the RPC CMS system are given.

4.1 Gaseous Particle Detectors

Gaseous particle detectors have been used as crucial components in High Energy Physics (HEP) experiments since the early stages in particles observation and detection. Their design and configuration has evolved throughout the years from the single-wire proportional counters introduced by Rutherford [91], to a wide range of fine resolution, fast and efficient detectors [92].

The basic physics particle detection principle remains the same, despite the great variety of gaseous detectors. As a particle crosses the detector gaseous medium and causes excitation and ionization within its constituents. The resulting primary electrons and ions act as free charges and are accelerated by an external electric field. These accelerated charged particles gain enough energy to cause secondary ionization and thus cause an avalanche. Depending on the electric field, the geometry and the used gas, the avalanche can grow to a streamer or a spark in the anode to cathode distance. These charges induce a signal on the readout electrodes, which depending on the detector layout and electronics can give good position and time resolution on the particle's path. Schematic view of an avalanche formation in gaseous detectors is shown in figure 4.1.

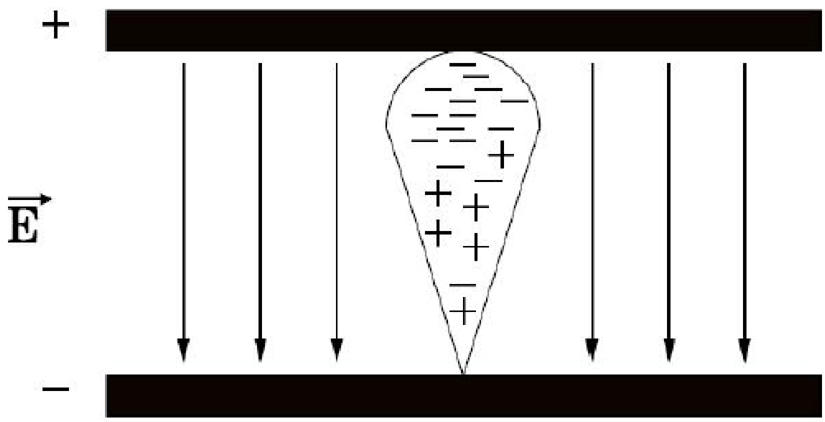

Figure 4.1: Illustration of an avalanche formation in a gaseous particle detector.

4.2. RPC Working Principle

Resistive Plate Chambers (RPCs) are planar gaseous detectors, that combine very good time resolution of ~ 1 ns, adequate spatial resolution, simple design and low cost. They are first developed in the early seventies when a parallel chamber using one glass plane with high resistivity (10^9 – 10^{10} Ωcm) is successfully applied in an experiment [93, 94]. It the early eighties the two-plane chambers are built, consisting of two high-resistivity High Pressure Laminate (HPL) Bakelite planes containing a low-pressure gas mixture [95]. Introducing of the avalanche mode to the RPCs [96, 97] in the nineties leads to increase in their rate capabilities to the kHz cm^{-2} range. All these developments make RPCs a leading choice for large area high rate experiments.

RPCs have a very simple design – a gas detecting volume is enclosed by two resistive electrodes. The electrodes are generally made from Bakelite with a bulk resistivity of 10^{10} – 10^{12} Ωcm and have conducting coating (usually graphite). Rectangular plastic frames are used for electrodes mounting, and small plastic separators (spacers) keep the constant distance between them, thus ensuring electrical and mechanical stability. A schematic view of an RPC and its principle of operation are shown in figure 4.2.

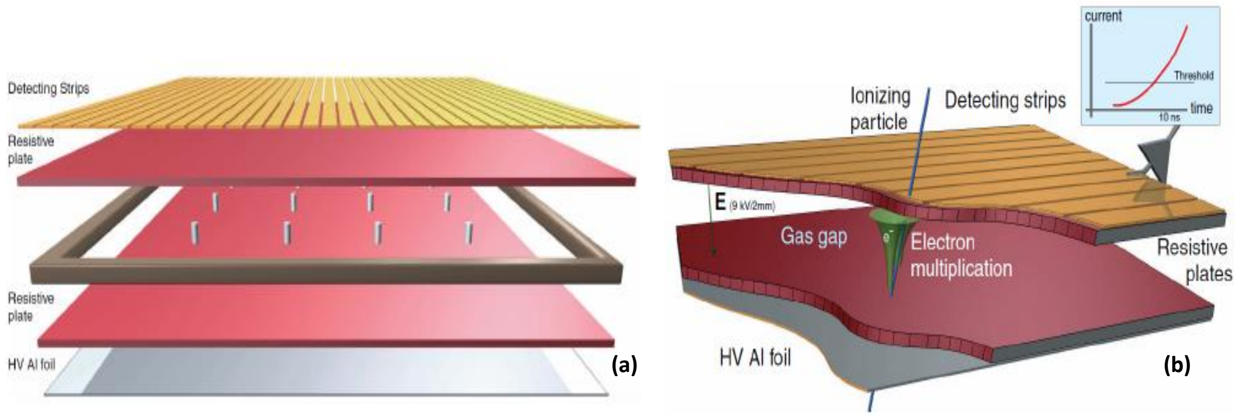

Figure 4.2: Schematic view of the different layers of an RPC (a) and illustration of RPC detecting principle (b).

As RPCs are gaseous detectors, their working principle is based on the ionization effect in the gas, caused by a charged particle passing through the detector volume. The avalanche multiplication is caused by a cluster of electrons obtained after the ionization [98]. This leads to an electron charge developed inside the gap, which further drifts towards the anode. The useful signal of the detector is the charge induced on the pickup electrode. The HV power supply is compensating the charge collected on the electrodes, by moving the charges outside the gap.

The effective ionization coefficient is defined as:

$$\eta = \alpha - \beta \qquad (4.1),$$

where α the Townsend coefficient describing the electron-ion pairs originally created, and β is the attachment coefficient describing the average number of electrons attached to form a negative ion [99].

For RPCs operating in avalanche mode (as in the CMS experiment), the average charge q_e of a single avalanche can be defined as [81]:

$$\langle q_e \rangle = \frac{k}{\eta d}\langle Q_e(d)\rangle = en_0 \frac{k}{\eta d}\frac{\lambda}{\eta + \lambda} e^{\eta d} \qquad (4.2),$$

where k is defined as

$$k = (\varepsilon_r d/s)/(\varepsilon_r d/s + 2) \qquad (4.3),$$

and

- e is the electron charge,
- n_0 is the average size of the primary ionization cluster,
- λ is the cluster density for the used gas mixture,
- ε_r is the relative dielectric constant of the electrode,
- d is the gap width
- s is the electrode thinckness
- Q_e is electron charge developed within a gap width d.

Maximum useful signal on the readout electrodes for a given ηd is obtained when the factors k and λ are as large as possible.

4.3 RPC system at the CMS experiment

4.3.1 Detector Design

CMS RPC system consists of 1056 double-gap chambers operating in avalanche mode [100]. Each RPC detector relies on two High Pressure Laminate (HPL) Bakelite gaps with 2 mm gas space between the plates [85]. The HPL electrodes bulk resistivity is of the order of 1 – 6 x 10^{10} Ωcm. The plates in each gap are separated by a 10 x 10 cm^2 grid of plastic pieces called spacers in order to avoid contact due to the electrical attraction between them. The inside surface of the gaps is coated with a 35 to 45 μm linseed oil [101] in order to smoothen the surface and quench the Ultraviolet (UV) photons [102]. The outer surfaces of the gaps are coated with conductive graphite paint, thus forming the High Voltage and ground electrodes. The two gaps are placed one on top of another with a common readout performed by copper readout strips placed in between and isolated from the graphite by mylar sheets. Schematic view of the RPC double-gap design is shown in figure 4.3.

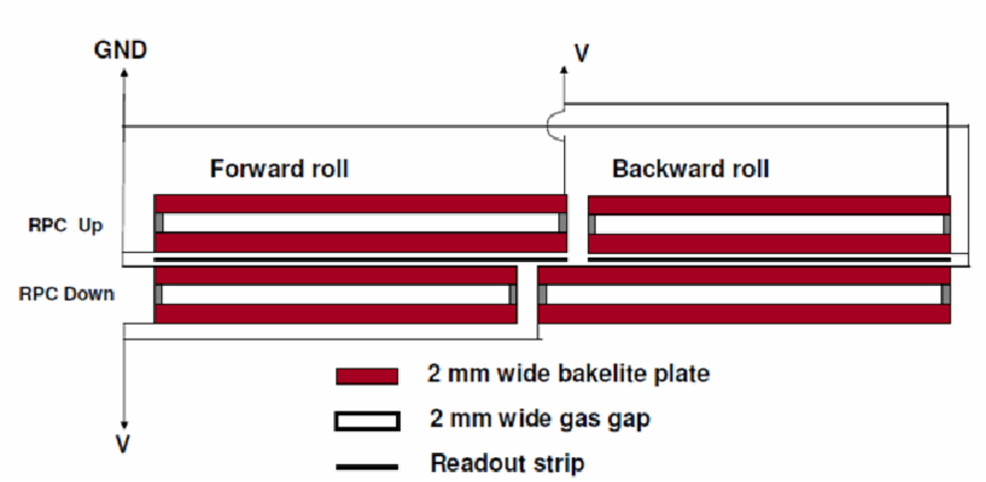

Figure 4.3: Schematic layout of a Barrel double-gap RPC.

The standard RPC gas mixture is composed of three components –

- **95.2% $C_2H_2F_4$**, acting as the charge carrier gas [103]
- **4.5% iC_4H_{10}**, acting as a quencher gas to absorb UV photons from molecule de-excitation
- **0.3%** SF_6, controlling the excess electrons through its high electron affinity [104].

The gas mixture is kept at 21°C and ~ 35% - 40% humidity is added in order to maintain the bakelite resistivity, which increase as the bakelite dries out [105].

The RPC system should fulfill the following CMS requirements:

- High detector efficiency > 95% with more than 300 V long plateau
- High rate capability ~ 300 Hz/cm^2
- Average cluster size ~ 2 strips
- Intrinsic time resolution < 1.6 ns (for BX identification)
- Intrinsic Noise < 5 Hz/cm^2
- Spatial resolution ~ 10 mm
- Ability to withstand in long term operation and high background radiation.

4.3.2 Detector Layout

The need to trigger on the transverse momentum p_T of passing muons is the main driving force behind the detector layout of the CMS RPC system. The p_T is measured with the bending of the muon in the CMS magnetic field and this requires a muon to cross at least 3 out of 4 layers in the Muon system. These layers are interleaved with the steel return yokes ensuring a maximum muon track bending between them.

The RPC system is divided two regions following the CMS experiment configuration – Barrel region and Endcap region. It is composed of 1056 chambers covering a pseudorapidity range of $|\eta| < 1.2$ in the Barrel and $0.9 < |\eta| < 1.9$ in the Endcap. It has more than 110 000 electronic channels and covers a sensitive area of 3500 m^2.

4.3.2.1 Barrel RPCs

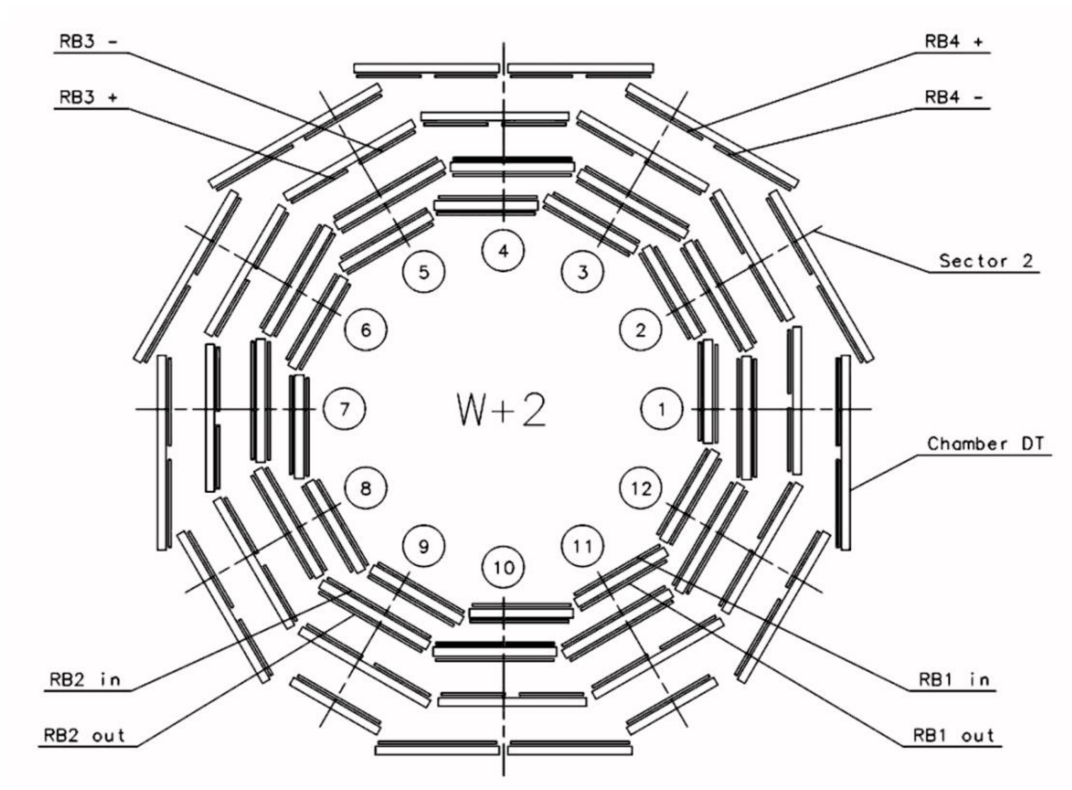

Figure 4.4: Schematic layout of one of the 5 Barrel wheels with the numbered sectors shown.

The Barrel RPC system consists of 480 RPCs, distributed equally among 5 wheels along the beam pipe – Wheel 0, Wheel ±1, Wheel ±2. Each wheel consists of 4 stations (RB1, RB2, RB3 and RB4) with increasing radius R, which are interleaved with the steel return yoke. The inner two stations has 2 layers of RPCs with a DTs in the middle, while the outer two stations each consist of one layer of RPCs and lone layer of DTs. According to the direction of the azimuthal angle ϕ, each wheel is divided into 12 sectors (S01-S12), as dictated by the mechanical construction of the CMS return yoke. Due to mechanical reasons, RB3 and RB4 are further divided to + and – along ϕ in all sectors apart from S04, S09 and S11 in RB4. Since RB4/S09 and RB4/S11 are in the feet of the barrel wheel, they consist of only a single RPC chamber. RB4/S04 is divided even more along 4 chambers - ++, +, – and – –. Schematic view of the RPC Barrel geometry is given in figure 4.4.

Further to the trigger requirements, the chambers are divided with respect to pseudorapidity in 2 partitions, called rolls – forward and backward [76], shown in figure 4.5. Only RB2in in Wheels -1, 0, +1 and RB2out in Wheels -2, +2 are divided in 3 rolls – forward, middle and backward, as shown in figure 4.6.

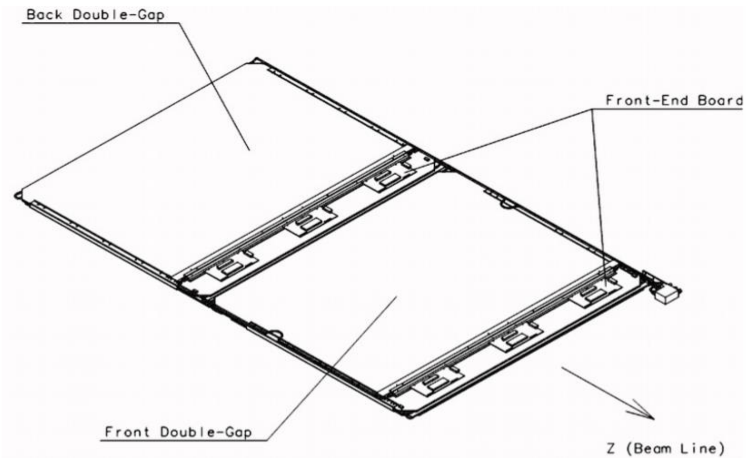

Figure 4.5: Schamatic illustration of the RPC Barrel 2 - η partitions.

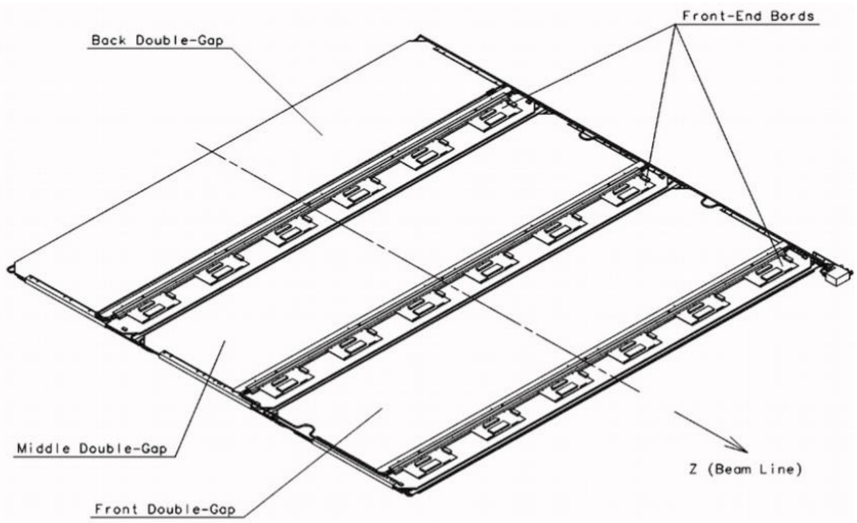

Figure 4.6: Schamatic illustration of the RPC Barrel 3 - η partitions.

4.3.2.2 Endcap RPCs

The RPCs design in the Endcap is very similar to the one used in the Barrel. The main difference comes from the geometry aspects and the fine segmentation which higher multiplicity in the forward regions require.

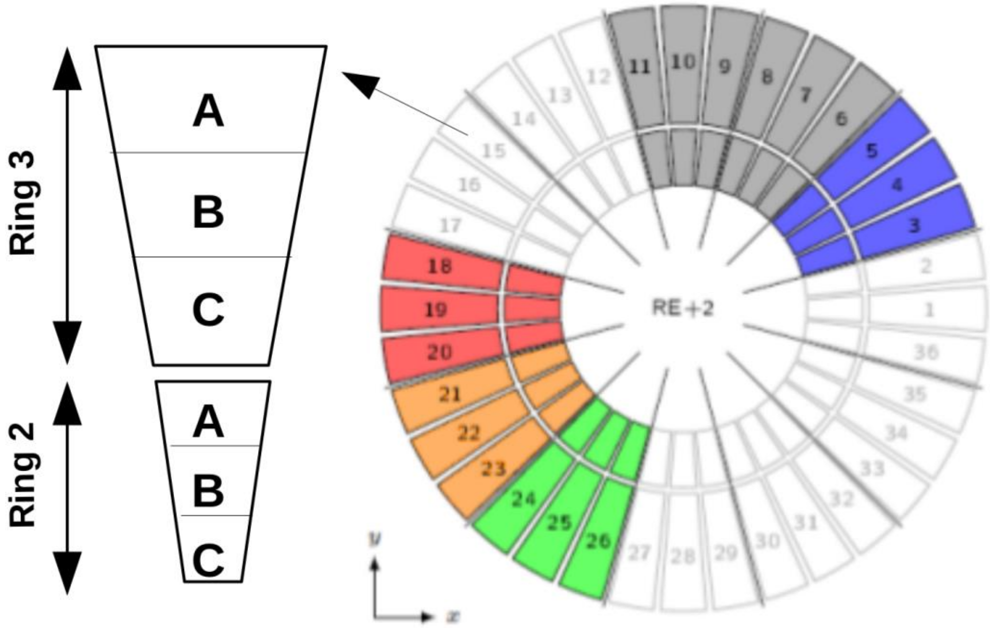

Figure 4.7: Schematic layout of one of the Endcap disks (RE+2) showing the grouping of chambers into sectors.

The Endcap RPC system consists of 576 RPCs, which are distributed along 8 disks named RE ±1, RE ±2, RE ±3 and RE ±4 – 4 disks per each endcap (positive and negative). The two disks for the fourth stations both positive and negative are instrumented with 144 RPC detectors during the LS1 Muon system upgrade (2013-2014). Each disk is divided in 36 sectors along ϕ, and has two concentric rings – ring 2 (R2) and ring 3 (R3). There are 36 10° trapezoidal RPC chambers building up each ring, which are further divided into three rolls, labeled A, B and C with respect to increasing η. Each chamber is indicated as a segment CH01 through CH36 within a ring. Segment CH01 lays on the positive X-axis direction and the numbering proceeds anti-clockwise in respect to the interaction point. Schematic view of the RPC Endcap geometry is given in figure 4.7.

4.3.3 Detector Electronics

The CMS RPCs have a configuration of two 2 mm gaps, operated in the so-called avalanche mode, with a common pick-up readout signal electrodes (strips) in the middle. For freon-based gas mixtures with a gas time constant [106] at the nominal working point of the detector $\tau \sim 1$ ns and electron drift speed in order of 130 μm, a single cluster induces a shape of current signal that can be easily described by the function [107]:

$$I(t) = I_0 \exp(t/\tau) \quad (4.4),$$

where $0 \leq t \leq 15$ ns. The expected dynamic range is between 20 fC and 20 pC.

The readout strips have length of 1.3 m in the Barrel and 1.6 m in the Endcap RPCs [76, 108]. Their width ranges between 1.5 and 4 cm, according to the position of the detector in the apparatus (see sec.4.3.2), with characteristic resistance of the strip from 40 to 15 Ω, respectively, and capacitance between ~160 and ~420 pF. Strips are connected to the channels of the front end electronics by Kapton foils in the barrel region or coaxial cables in the endcap region on one end. In order to avoid reflections, strips in the barrel region are terminated by a resistor on the other end.

- The Front End Chip –

The Front End Chip (FEC) aim is to amplify the RPC signals and generate fast output pulses for timing. The circuit for each FEC is made of eight identical front-end channels, shown in figure 4.8 [107]. Each channel consists of a preamplifier, zero-crossing discriminator, monostable and a differential driver.

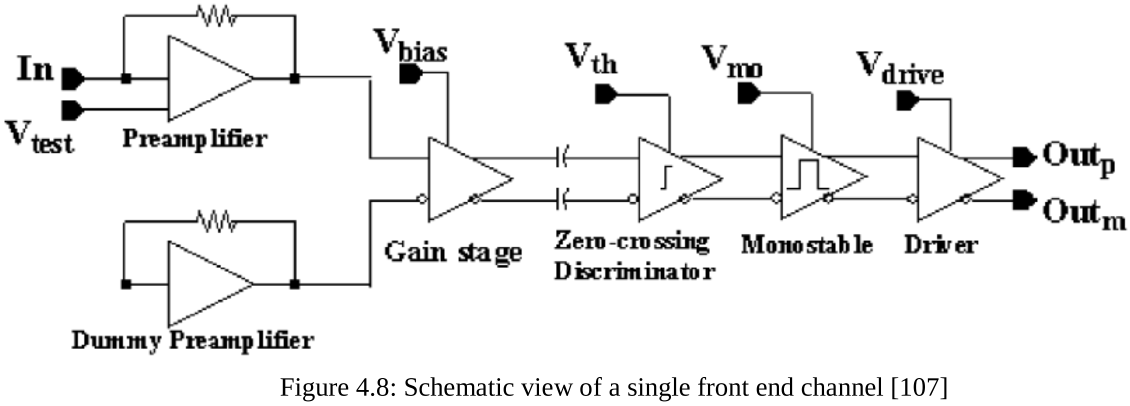

Figure 4.8: Schematic view of a single front end channel [107]

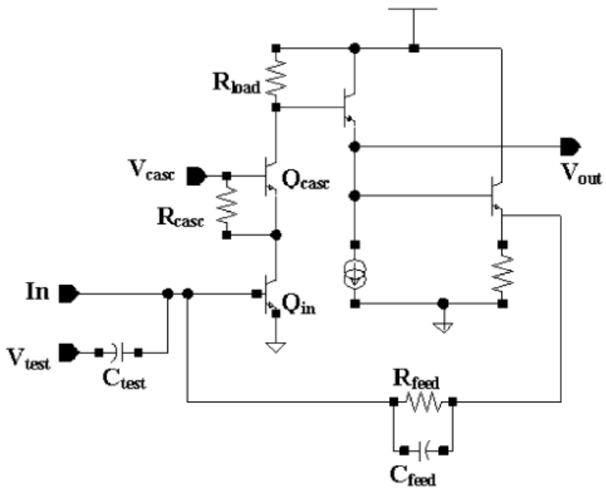

Figure 4.9: Current preamplifier [107]

Taking into account the signal frequencies (between 100 and 200 MHz), the preamplifier, shown in figure 4.9, is a cascaded common emitter transimpedance stage, which, in order to match the characteristic impedance of the strip in case of 4 cm wide strips, has input impedance of 15 Ω. For all other cases the matching is obtained by adding an external series resistor at the board level. The obtained charge sensitivity is 0.5 mV/fC. Balancing the DC output variations of the real input first stage requires adding of a "dummy" input preamplifier (figure 4.9).

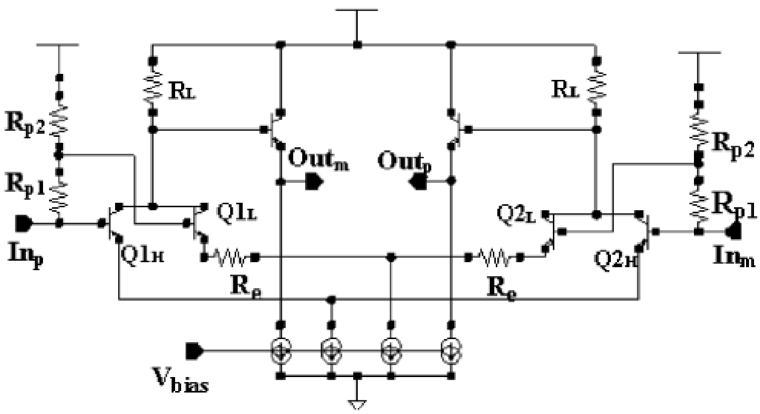

Figure 4.10: Gain Stage. [107]

Next is the gain stage, shown in figure 4.10. It is designed to provide non-saturated response on the dynamic range and to fully exploit the zero-crossing timing. Gain stage is DC-coupled to the preamplifier. Larger inputs do not require linearity, so the circuit must ensure a linear behavior only in the threshold range. The preamplifier output is thus sent to two differential amplifiers, which have different gains, but common output nodes.

Unambiguous assignment of the event to the related bunch crossing requires accurate timing information from the RPC. A threshold discriminator is used for achieving the leading edge timing, which is the simplest way to provide trigger pulse. This method is simple, but it can be affected by the amplitude time-walk. When considering RPC signals with 1000:1 dynamic range (20 fC – 20 pC), the time walk is ~10 ns [109].

The technique of zero-crossing can approximate an amplitude-independent timing response – a CR network produces a bipolar pulse after differentiating the input signal. The bipolar pulse is then crossing the zero in correspondence of the peak of the input signal [110]. Considering that input signals have the same peaking time, the zero-crossing time can be used as time reference, since it is independent of signal amplitude. Figure 4.11 shows the block diagram of the discriminator. The outputs of the amplifier are differentiated through a CR network. In this way, the fast recovery time of the baseline is granted. The recovery time is < 50 ns even in the case of a 20 pC input charge.

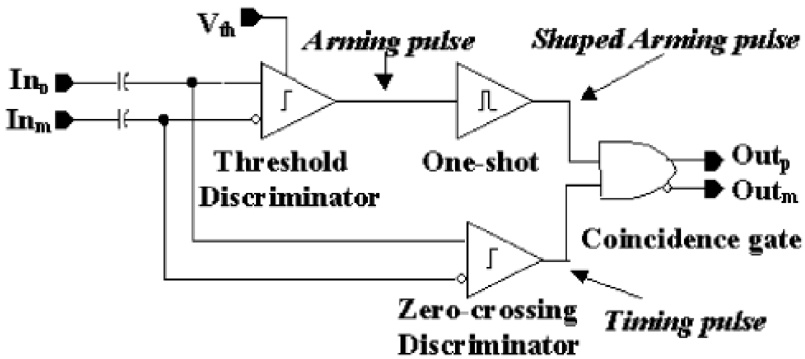

Figure 4.11: Block diagram of the Discriminator. [107]

The threshold discriminator consists of a double stage differential amplifier and provides charge selection capability. The threshold range is between 5 and 500 fC. The discriminator is followed by a one-shot circuit, which shapes the pulse typically at 20 ns, and so ensuring its coincidence with the zero-crossing discriminator (ZCD) output. The ZCD is also a double-stage differential amplifier, which has no threshold. Figure 4.12 shows the output of the discriminator, which is obtained after combining the outputs of the one-shot and the ZCD. A monostable circuit following the discriminator, gives a pulse typically shaped at 100 ns, in order to mask a possible second trigger due to an after-pulse of the avalange one. The monostable prevents the ZCD from triggering on the noise.

Finally, an Output Differential Driver feeds a twisted pair cable with a signal level of 250 mV on 100 Ω to the LVDS (Low Voltage Differential Signaling) receivers [111].

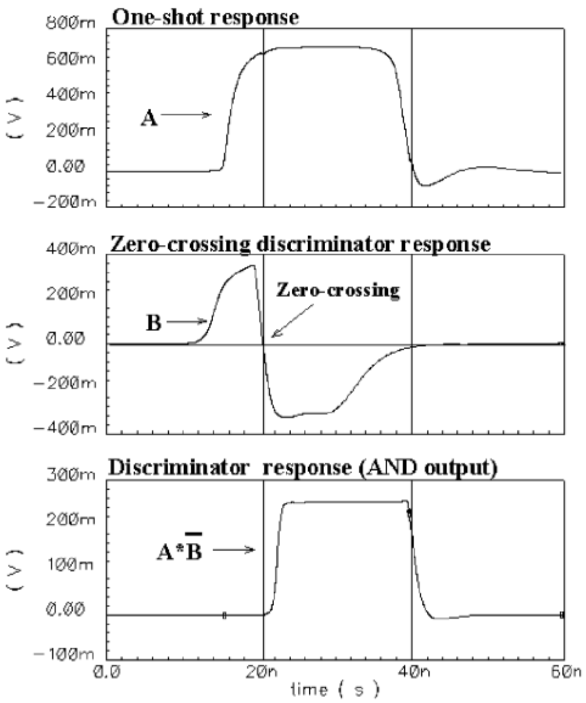

Figure 4.12: Discriminator operations principles. [107]

- The Front End Board –

The Front End Board (FEB), shown in figure 4.13, is connected directly to the RPC and contains two or four 8-channel FECs, depending on the region (see sec 4.2.2), Front End Control Circuit (FECC or FEBC) and 2 Synchronization units (SUs). The FECC provides the threshold voltages and test pulses to the FECs and synchronizes the front end signals to the system clock.

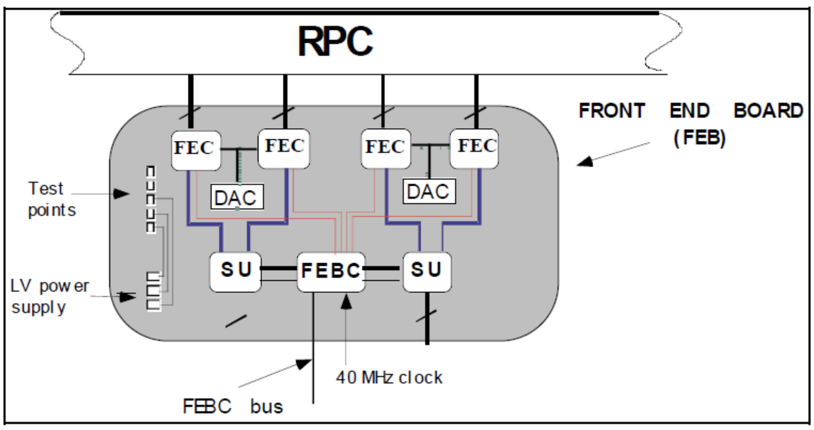

Figure 4.13: Schematic view of a Front End Board (FEB) [76]

FEBs have two main parameters – the discriminator threshold, implemented as a Threshold Voltage (V_{TH}) and the output pulse width, which is defined by the Monostable Voltage (V_{Mon}). These threshold voltages are provided by on-board Digital-to-Analog Converters (DACs). They are common for the 8 channels of one FEC. The value of the output voltage is given by [112]:

$$V_{TH} = \frac{2V_{ref}}{1024} * word \quad (4.5),$$

where V_{ref} is the voltage reference (500 mV), and *word* is the input digital word of the DAC. The relationship between the charge threshold and threshold voltage (V_{TH}) is [109]:

$$Q_{TH}[fC] = \frac{V_{TH}}{3.2} \sim 0.3\, fC/bit \quad (4.6).$$

The Synchronization unit (SU) stores the FEC output data. It synchronizes the data which fall within a predefined time window within a bunch crossing period with a pre-selected bunch crossing period. The SU has its own histogramming of rates for every data channel.

For safe operation, each FEB contains also at least one temperature sensor.

5. RPCs for the 2013-2014 muon upgrade of CMS

This chapter presents the entire RPCs production process for the 2013-2014 muon upgrade. As a member of the CERN team participating in the production process, the doctorate candidate takes part in all activities on testing the detecting elements, assembling of the new RPC chambers and the subsequent evaluation on their working parameters before their mounting on the CMS experiment. A detailed description on all production steps is given below.

5.1 Upgrade Physics motivation

The Compact Muon Solenoid (CMS) experiment [56] has been running and collecting data successfully since the beginning of the first Large Hadron Collider (LHC) [46] physics run in 2009. The foreseen gradual increase of the instantaneous luminosity of up to more than twice its nominal value of 10^{34} $cm^{-2}s^{-1}$ during Phase 1 of the LHC running, (until about 2022), presents special challenges for the machine and the experiments. There are two shutdown periods [113] scheduled to give the necessary time to anticipate these luminosity increases – Long Shutdown 1 (LS1) in 2013/2014 prepares the accelerator to run at its nominal luminosity and Long Shutdown 2 (LS2) in 2018/2019 should take it to 2.2 times this value. During these long shutdown periods the CMS Collaboration main goal is the upgrade of several subsystems of its detector [113]. In particular during LS1 one of the major upgrades is done at the CMS muon system [114, 115]. The major focus goes to the muons with high transverse momenta, since they are among the key objects in detection of possible new physics phenomena. In order to be effective, the muon trigger must have good resolution to identify high transverse momenta (p_T) tracks. Thus, the RPC upgrade is essentially driven by the impact of the instantaneous peak luminosity on the trigger system.

The CMS Level-1 muon trigger relies on Resistive Plate Chambers (RPCs). They serve as dedicated trigger detectors, which improve the muon reconstruction. There are six concentric layers of chambers in the barrel part and four layers of chambers in the endcaps (see sec. 4.2.1). Adding of the forth layers during 2013-2014 upgrade completed the original design of the muon system, thus improving the trigger efficiency in the endcap region with pseudorapidity in the range $1.2 < |\eta| < 1.9$, shown in figure.3.10.

The necessity of adding the RPCs forth layers (RE4s) to the endcap system is driven by the Level-1 trigger, which requires hits in at least three layers. [76] Thus, as can be seen in figure 5.1, before the upgrade the system does not have the necessary redundancy to control the trigger rate while preserving high trigger efficiency at the increased luminosity.

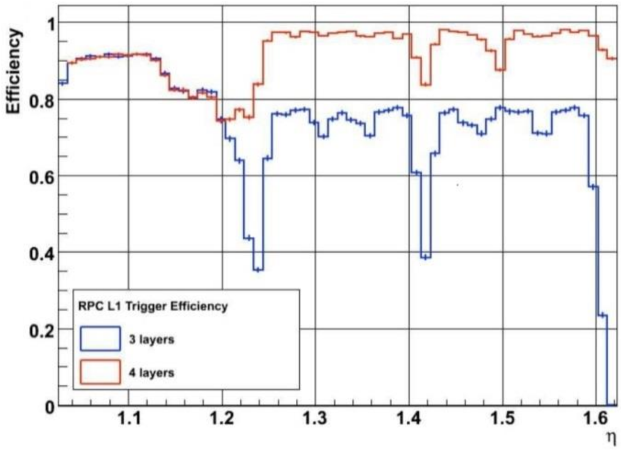

Figure 5.1: Simulated RPC Level-1 trigger efficiency for the system before the 2013-2014 upgrade with three endcap layers compared to the system after the upgrade with four endcap layers.

The main contribution to the trigger rate comes from mis-measurements of muons with low transverse momenta that are promoted to high pT muons. In a three-layers system, the much higher flux of such poorly measured low-momentum muons at increased luminosity will dominate the trigger rate and make it unacceptably high, which in turn leads to unacceptably high muon pT-trigger thresholds. Adding the forth layer in the endcaps, enabling a 3-out-of-4 trigger logic in those regions, brings the RPC endcap performance to a similar level as the barrel system.

5.2 RPC design

The forward stations of the RPC system consist of wedge shaped detectors with a double gap RPC. The layout of the stations and the chambers is shown in figure 5.2a. The actual system consists of 576 chambers (including the forth stations) mounted in two concentric rings [108] on the endcap disks as illustrated in figure 5.2b.

The newly installed chambers RE4 chambers inherit their design from the RPC endcap chambers installed before them, shown in figure 5.4a. The detector relies on trapezoidal shaped High Pressure Laminate (HPL) Bakelite gaps, with 2 mm gas space between the plates, organized in a double-layer configuration with copper strip readout panel placed in between [85]. The HPL sheets resistivity is of the order of $2 – 5*10^{10}$ Ωcm. They operate in avalanche mode with a standard gas mixture of 95.2% $C_2H_2F_4$, 4.5% iC_4H_{10} and 0.3% SF_6.

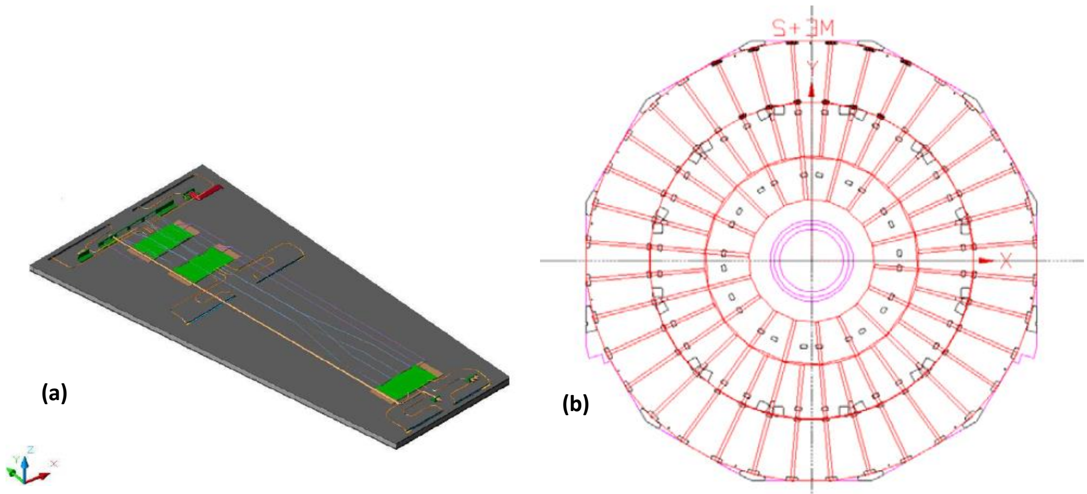

Figure 5.2: Schematic layout of a forward double-gap RPC (a)
and layout of an RPC layer on the yoke disk (b).

A chamber is made of three kinds of different gap geometries – one large gas gap is used at the bottom layer, while the top layer is segmented into two parts, as illustrated in figure 5.3.b. This configuration is used to simplify the signal cable routing.

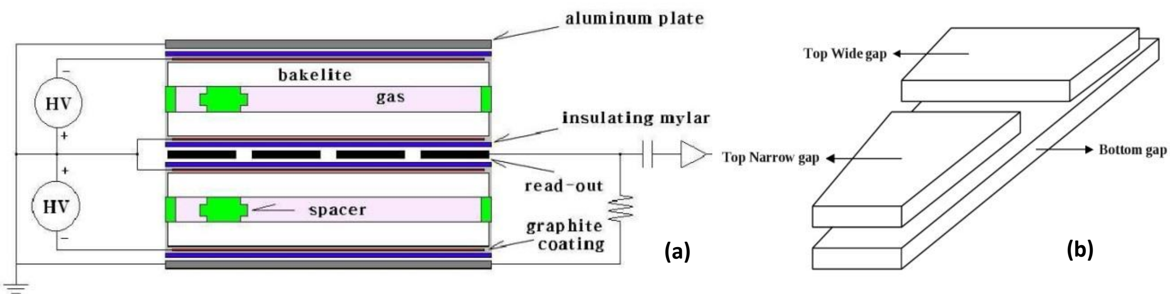

Figure 5.3: Schematic representation of the double-layer layout of the endcap chambers (a).
Configuration of the gas gaps of the endcap chambers (b).

The readout strips are segmented in three η-partitions with increasing strip pitch from 1.5 cm to 4 cm [116]. Since each partition has 32 strips, there are a total of 96 strips per chamber. Coaxial cables are used to connect strips to Adapter Boards which are linked to 3 Front-End Boards (FEBs) per chamber. There is 1 Distribution Board (DB) for the electronics control for each chamber. Link Boards (LBs) are the main components of the off-detector electronics. They receive from the FEBs signals in LVDS (Low-Voltage Differential Signaling) standard. Thus, synchronization with the LHC clock and transmission of the signals to Trigger Electronics in the control room is performed by the LBs. In each LB crate there is a Control Board (CB) that drives the crate, provides inner-crate communication and takes care of the connection to the readout and trigger systems. The layout of the RPC electronics is shown in figure 5.4.

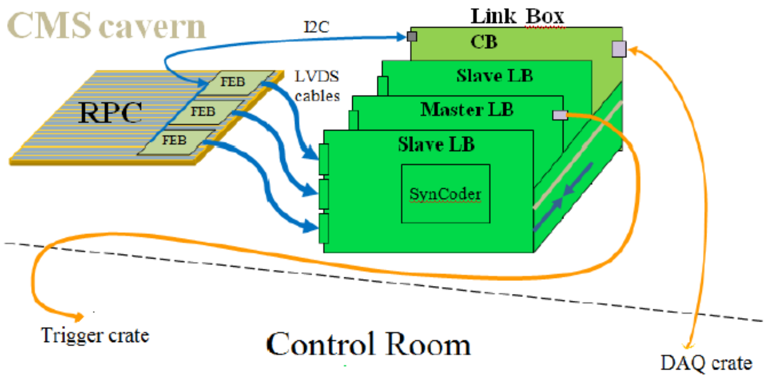

Figure 5.4: Schematic layout of the RPC electronics.

Chambers are embedded in honeycomb boxes with all the chamber services (readout electronics, gas inlets and outlets and water cooling circuit) mounted on the outside. The water cooling circuit on the RE4 chambers consists of Cu pipes, which are soldered onto three copper plates where the FEBs are mounted. The cooling circuit and the FEBs are covered by an aluminum screen box.

5.3 Production procedures

In the section below are reviewed briefly the main aspects relevant to the chamber production. The quoted numbers refer to the production of 200 RPCs during the LS1 upgrade, out of which 144 are used in the RE4 stations and the rest are kept as spares for the forward system.

5.3.1 HPL production

Producing the High Pressure Laminate (HPL) sheets [108] is the first step in the fabrication of RPC gas gaps. The procedure is well established and includes the following main steps – production of the HPL foils, quality check for resistivity measurement, check for the surface quality, cutting of the foils to the requested size and finally surface cleaning of the obtained components.

The raw material production is done at the Puricelli firm (Milan) [116], where about six hundred of 1620 x 3200 mm^2 sheets for a total of 3110 m^2 are manufactured. Specifications for the HPL bakelite sheets, required by CMS, are very detailed. One of the major requirements is high uniformity in resistivity across the surface of the sheets, as well as between the sheets. Another one is a resistivity value of 2–5*10^{10} Ωcm (at 20° C).

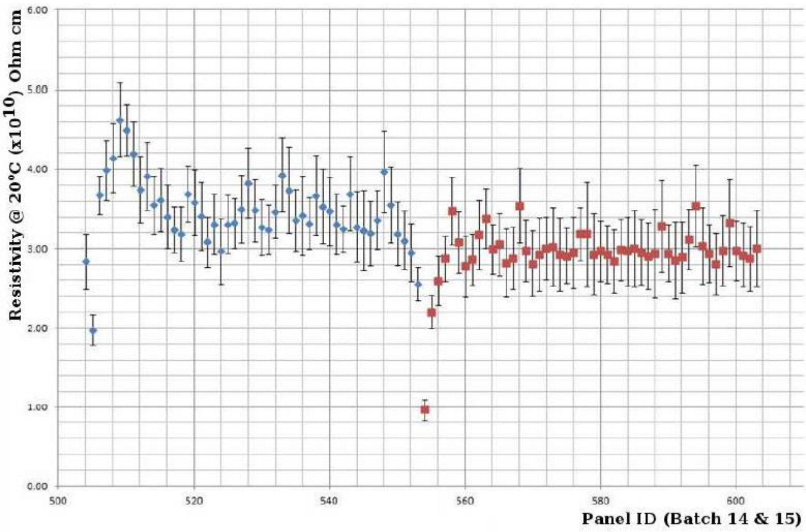

Figure 5.5: Measured resistivity for production batches of HPL sheets. The spread in the resistivity values measured at different points along the surface of the sheet is indicated by the error bars.

In figure 5.5 the resistivity values measured for two production batches are displayed. The data shows the average resistivity value and spread, which are measured across the sheet surface at nine different positions. There are 50 panels produced per batch and it can be easily seen that the obtained resistivity values are well inside the CMS requirements.

Next step is the quality control of the HPL sheets, done by the Pavia INFN site. After passing this control the sheets are cut by Riva (Milan), shown in figure 5.6 and the final procedure is the cleaning of the surface, done by General Tecnica (Frosinone).

Figure 5.6: Bakelite sheets cut for the RE4/2 top narrow and top wide gaps (a) and bottom gaps (b).

5.3.2 Gap production

The gas gaps are produced by the Korea Detector Laboratory (KODEL) at Korea University, where the HPL sheets are sent after being tested and approved. A standard CMS RPC for the forward region consists of 3 gaps forming double layers. This means that for 144 RE4 RPCs to be produced, a total number of 432 gaps are required. However, 200 gaps more are additionally produced for the contingency and repairs of any damaged in future RPC modules. The RPC detectors for the LS1 upgrade are mounted in two concentric rings RE4/2 and RE4/3, which requires the shapes of the gaps to be trapezoidal with heights of 1663 mm and 1930 mm, respectively [76].

There are several major steps in producing RPC gaps [117] – graphite coating, PET film coating, spacer bonding and gas leak test, linseed oil treatment and high voltage (HV) test, where dark currents are measured and monitored.

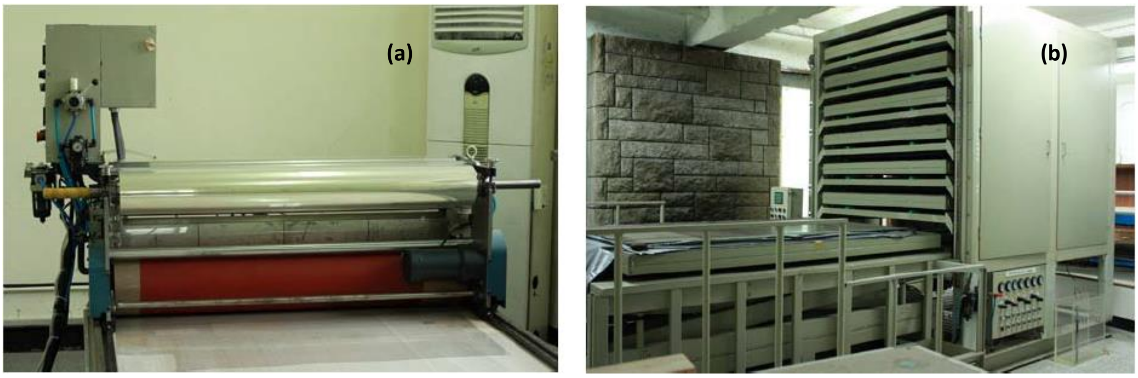

Figure 5.7: Electrode insulation machine (a) and gap assembly machine (b).

Once arrived at KODEL, the HPL sheets are inspected for defects in color, scratch on the surface and mechanical damages on the edges and corners. All selected HPLs are cleaned with Isopropyl Alcohol (IPA). The electrodes of the gaps are produced with a thin layer of graphite, which is coated on the bakelite sheets. The surface resistivity of the electrodes ranges from 100 to 250 kΩ/square [118]. Next is insulating of the graphite surface with PET (Polyethylene Terephthalate) film. The machine used to glue the PET film is shown in figure 5.7a. Then the gaps are assembled with two electrodes and spacers. The spacers are coin shaped and placed between the electrodes to achieve a 2 mm homogeneous separation and secure the uniform electric field within the gap. The edge of the gap is sealed with an edge strip. The spacers are placed 10 cm apart from each other in orthogonal directions to provide the mechanical support of the gap, while the edge strip, sealing the edge of the gap, makes the gas volume leak-tight. This configuration of the gap is placed under a special pressing machine, where epoxy is used to glue all components together. The glue hardening takes 24 hours (figure 5.7b).

Once produced, all gaps go through testing of the mechanical stability. First check is done to the secure bonding of the spacers on the surface of the electrodes. As shown in figure 5.8, the spacers are pressed by a KODEL robot and the pressure variation is used as an effective indicator of the good bonding [117]. Another check is done to the gas leakage rate. The leakage rate measurement is performed within the frame work of the bonding test. Figure 5.8b shows the results for the pressure variation when the spacers are pressed, while the differences of the pressure measurement at the beginning and the end of the test include the gas leak rate of the gas gaps. If the gap has small leakage rate, the curve shows a gradual decrease in pressure. The allowed maximum leakage rates for 10 min [117] are 0.2, 0.3 and 0.4 hPa for RE4/2 Top Wide (TW), Top Narrow (TN) and Bottom gaps, respectively, while for RE4/3 gaps they are 0.3, 0.4, 0.5 hPa.

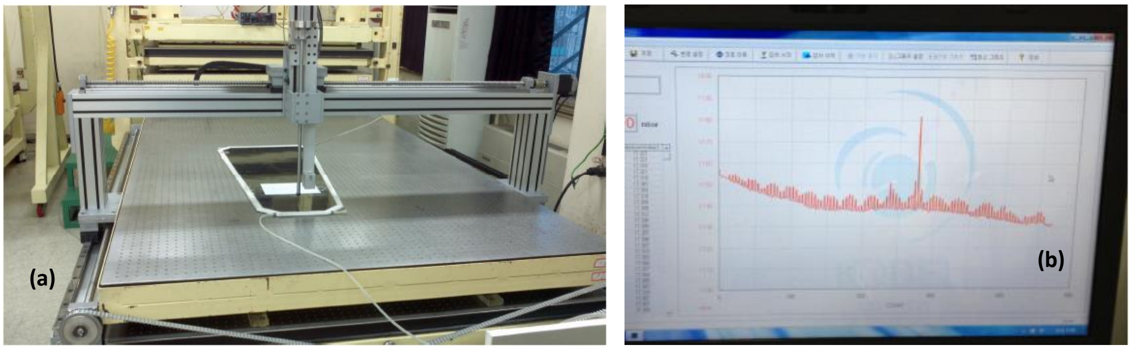

Figure 5.8: KODEL robot performing the pressure test (a) and the control console of the pressure test (b).

Next step for all gaps without loosen spacers and gas leak within the acceptable range is the linseed-oil procedure. During this process, the entire gas volume of the gaps is filled with linseed oil. The rate of administration of the oil into the gas gap is 100 cm/hour. Once finished with filling the entire volume of the gaps, the remaining oil is immediately removed by a small compressor. Then the surface is left to dry with circulating air of 30˚C. The dried oil surface forms a polymerized layer on the bakelite inside the gas volume, which reduces the spurious noise by a factor of 10 in the avalanche operation mode [119]. This is a very specific procedure, which needs a cautious preparation, due to the pressure built up by the linseed oil filling of the gas gaps. In order to ensure that the gas gap is not over-pressured to the limit of the epoxy bonding strength, the pressure within the gap should remain less than 20 hPa over the atmospheric pressure.

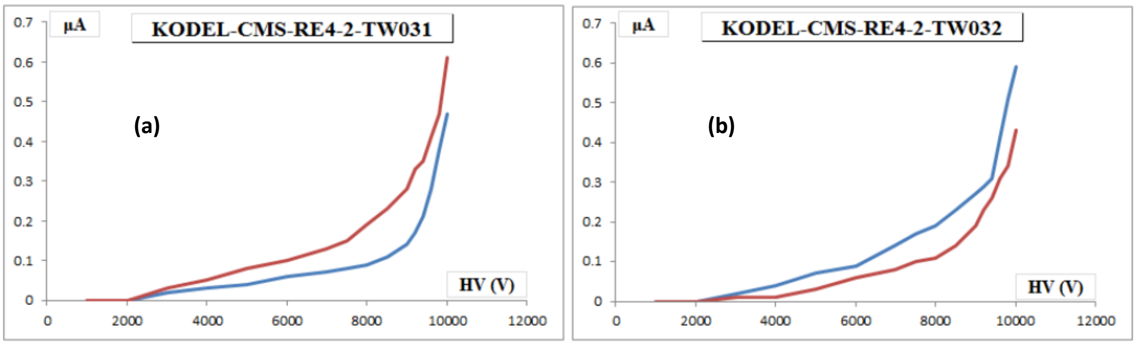

Figure 5.9: Dark currents of gaps as a function of HV up to 10 kV before (blue) and after a 120-hour long test (red). Two example behaviors are shown – one for a gap with higher current after the 120-hour test (a) and one for a gap with higher current before the 120-hour test (b).

The final step in checking the gas gaps is the electrical test. This test is done by measuring the dark current and has three steps. First the dark current is measured as the HV increases up to 10 kV [117]. The amount of current drawn from gaps at 6 kV should not exceed 1.5 μA. The maximum allowed at 10 kV is 5 μA for smaller gaps and 10 μA for larger gaps. A closer look to the plots show that each one has two components – one linear rising from zero up to 7 kV and another one with an exponential rise from 8 kV up to 10 kV, as shown in figure 5.9. This is the characteristic curve in the HV scanning.

At 6 kV the dark current is not yet originated from the avalanche of the gas ionization, thus up to 7 kV the current is mainly the ohmic current that flows through the surface of the gaps. Above 8 kV the exponential rise of the currents is contributed by the avalanche of the gas ionization.

Second step in dark current measurement is a 120-hour long monitoring of the gas currents at 9.6 kV. Here a gradual decrease of the current during the initial 40 hours is expected, and thereafter, there is a slight increase in the current's value. Finally the electrical test of the gas gaps is finished with performing a second HV scan up to 10 kV. Figure 5.9 shows two different measurements of the dark currents before and after the 120-hour long measurement, which are plotted against each other to detect any significant variations. The shown examples are for approved gaps.

Figure 5.10: Specially designed wooden box for gaps transportation.

Gaps which pass all the tests are transported to the chamber assembly sites. Transportations are normally done via air-carrier for safety reasons. For the safety of the transportation, wooden boxes are specially designed, so that the gaps are stored vertically inside the box and are clamped by using partially pre-stressed bars, as shown in figure 5.10. All gas inlet and output pipes of the gas gaps are open in case of sudden change of the atmospheric pressure during the transportation.

5.3.3 Electronics

Front End Boards (FEBs) for the 2013-2014 muon upgrade are produced in Pakistan. They have four 8-channel ASIC Front End Chips (FEC), which consist of amplifier, discriminator, monostable and differential LVDS line driver [108]. The connection between the readout strips of the RPC detectors and the FEBS is made with 50-Ohm coaxial cables. These cables are soldered on small Adapter Boards for easy plugging to the FEBs. A picture of one 32 channel FEB is shown in figure 5.11a.

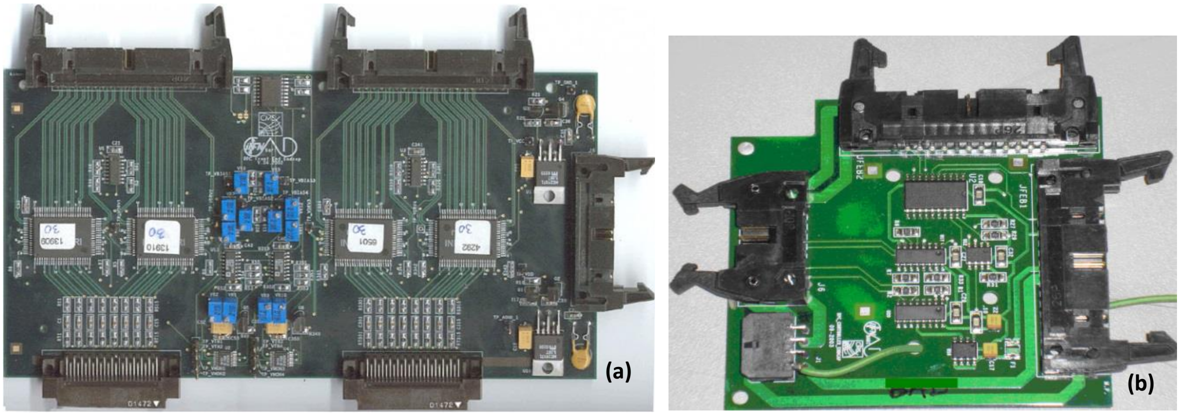

Figure 5.11: Frond End Board (a) and Distribution Board (b).

There is also one Distribution Board (DB) for each chamber (figure 5.11b), which receives power and slow control communication through I^2C bus and power cables and then distributes them to the FEBs via flat cables.

A total number of 650 FEBs, 1350 Adapter Boards and 250 DBs are produced including 10% of contingency [115]. All electronics before being shipped from Pakistan go through a series of validation tests, such as voltage threshold setting (VTH), voltage biasing setting (VBIAS), voltage monitoring (VMON) and I^2C for quality assurance.

The output signal from the FEBs is sent to the off detector electronics, i.e. the Link Board system, where are performed the synchronization with the LHC clock, the optical conversion and the transmission of the signal to the trigger electronics.

5.3.4 Chamber mechanics

The chamber mechanics have several components – honeycomb boxes, auxiliary parts, readout strip plane, cooling circuit with FEB support and screen box.

The honeycomb box is composed by Al top and bottom honeycomb plates and four edge bars. Layout of a typical RE honeycomb plate is shown in figure 5.12 [108]. The honeycomb plate is 6 mm thick and composed by 0.5 mm top and bottom Al covers sheets and 5 mm solid Al honeycomb core. At the four edges and few other positions where threaded holes are located, the honeycomb core is strengthened by insertion of 5 mm thick solid Al plates. For a better electronic protection, all slots and cut outs are filled up with foam. The cross section of the edge bars is 16 x 16 mm^2.

Production of honeycomb plates goes through several steps. First the 0.5 mm thick Al sheets are cut to the right shape. The additional 5 mm thick Al plates and the Al honeycomb cores are glued at the edges and at the necessary places in the middle is introduced foam. Next step is heating and pressing of the assembled plates at 120 ˚C in order to cure the glue and the foam. Finally all necessary slots and holes are machined.

The readout strip planes for the RE chambers are divided into three sections with 2 mm gap between the strips, as shown in figure 5.13. The plane is 0.3 mm thick and has a 0.035 mm thick copper cladding. An etching method is used to produce the strips. The strips planes are then covered with a 0.15 mm thick Mylar sheets for protection and insulation.

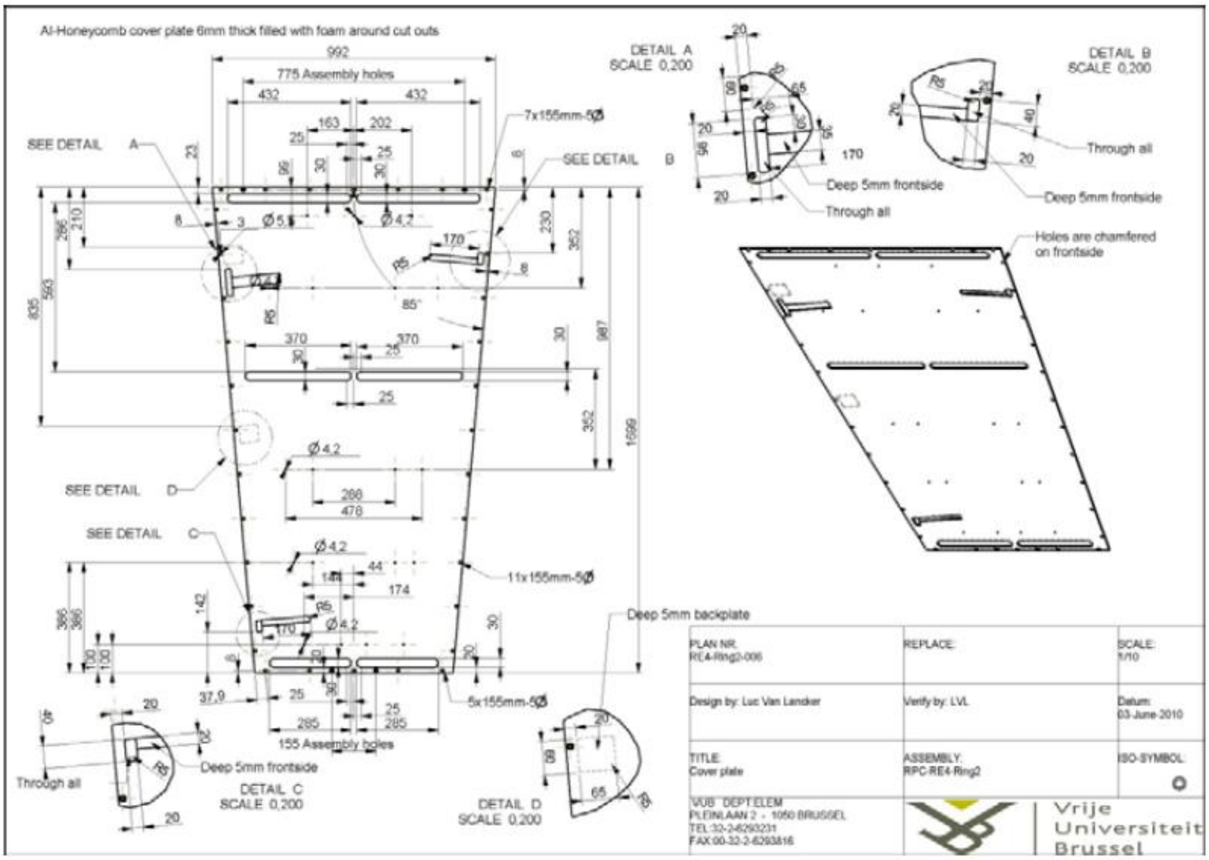

Figure 5.12: Layout of a typical RE honeycomb plate.

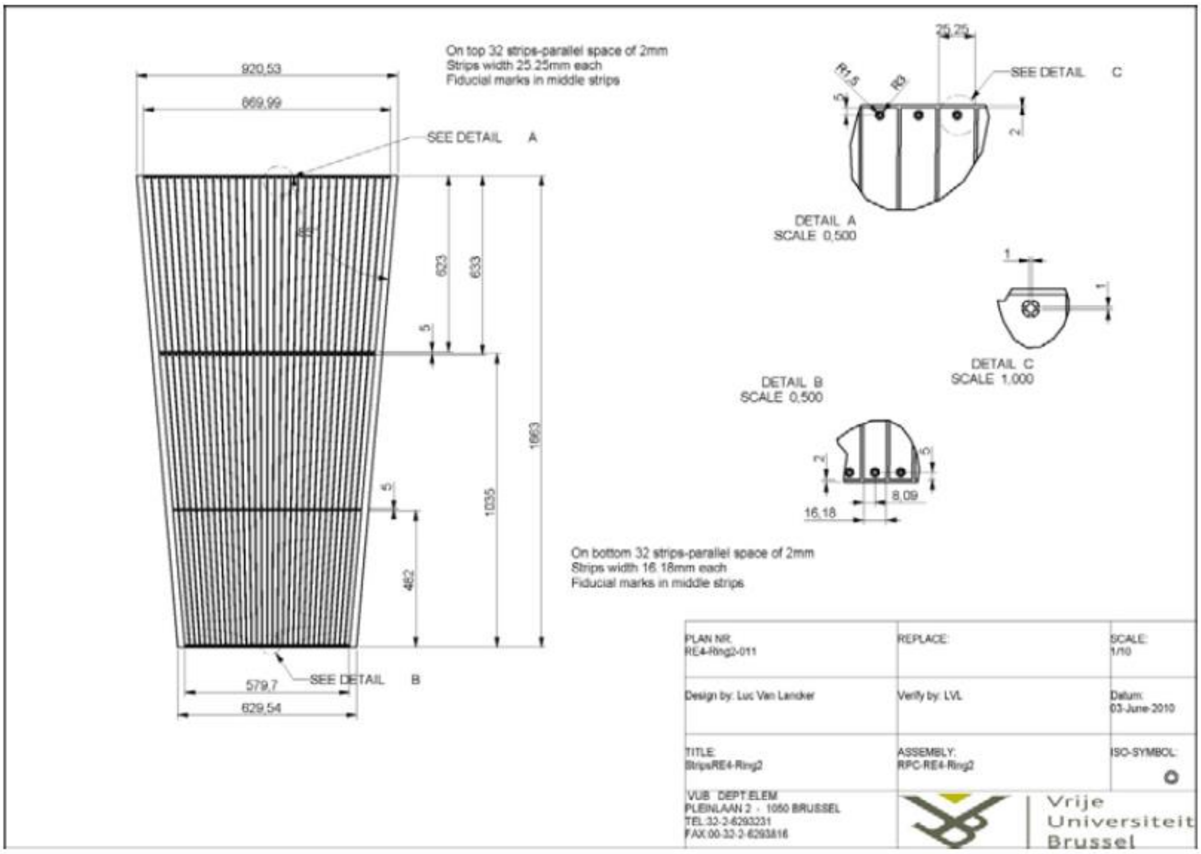

Figure 5.13: Layout of a typical RE readout strips plane [108].

The auxiliary parts include the front patch panel, the joined pieces for mounting the chamber in the yoke, the inside chamber fixation pieces, etc.

The cooling circuit [120] is made of copper pipes. FEBs are mounted onto copper plates which are are soldered to the pipes. A fully assembled Cu cooling circuit goes through series of leak tests with 20 bar of Argon gas. All approved cooling circuits are transported to the assembly sites, as shown in figure 5.14.

Final piece of the chamber mechanics is the screen box, which is made of 1 mm thick Al sheets and covers the entire cooling and FEB system.

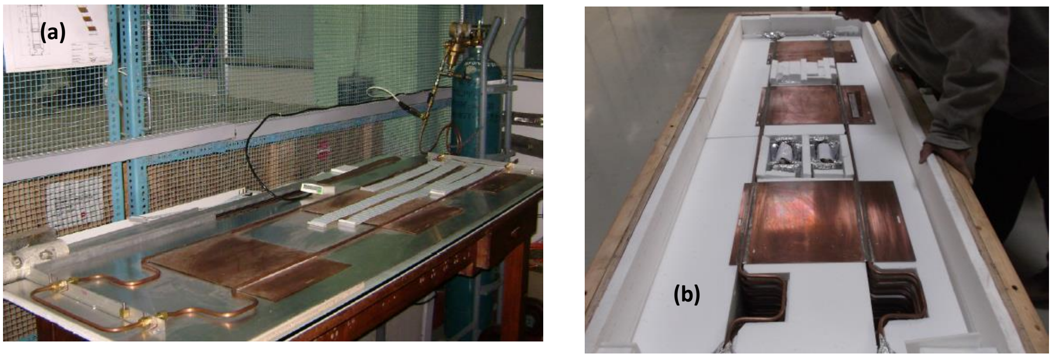

Figure 5.14: Cooling circuit for an RE4/3 RPC going through a leak test (a) and specially designed wooden box for cooling circuits' transportation (b).

5.3.5 Chamber assembly and test sites

There are three different assembly sites where the new RE4 chambers are built and tested – India (BARC), Belgium (Ghent University) and Switzerland/France (CERN). BARC and Ghent are in charge of 25% of the production each, respectively RE4/2 and RE4/3, while the remaining 50% of the production is carried out by CERN which work on both chamber types RE4/2 and RE4/3, as shown in figure 5.15. A detailed description of the CERN assembly facility is given, since the doctorate candidate is part of the team assembling the new RE4 chambers in CERN.

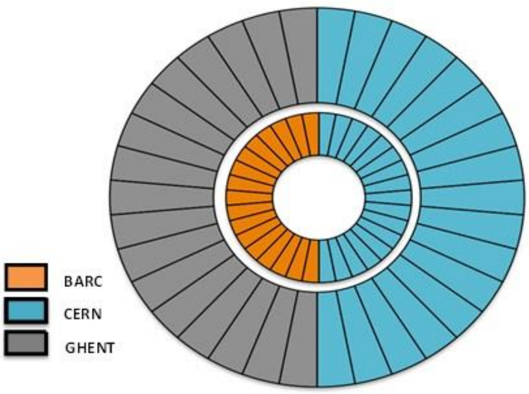

Figure 5.15: Schematic layout of one of the two new RE4 disks.

- **CERN 904 –** CERN assembly and test laboratory for the production of the new RE4 chambers is B904 [113], shown in figure 5.16. This facility includes the assembly tables and tooling for gas gaps quality control (QC) and quality assurance (QA), as leak tightness, popped spacers and HV behavior. There is also a cosmic telescope to test at once up to 10 detectors in order to determine all physical working chamber parameters.

Figure 5.16: CERN RPC assembly laboratory in B904.

The RPCs are assembled by filling the aluminum honeycomb box from the bottom up, starting with a Mylar sheet for insulation, copper sheet for ground, detecting gaps and readout strips, which are connected to the electronics. All these activities take place on specially designed tables – one granite and few other ones. Transportation of fragile or heavy materials from one part of the laboratory to the other is done with special scissor tables. All plastic and copper tubings for the gas and the cooling inside the detectors are first formed and then fitted.

The chamber assembly can start once all the predefined tasks (cable preparation, gas tube forming, honeycomb panel milling for HV connections and services, etc.) are done. Once assembled, chambers undergo cosmic tests at the specially designed test stand, which has the capacity to certify simultaneously 8/10 detectors. The complete cycle of producing and testing of an RPC is roughly 2 weeks. After passing the cosmic tests, chambers undergo long term current measurement under nominal operational voltage. A special area, separated from the cosmic telescope is instrumented for this purpose.

5.4 Quality control

The main aspects of the Quality Control (QC) protocols of producing and testing of the RPCs for the LS1 Upgrade of the CMS Muon system are described below.
The entire production QC is divided into 5 levels, depending on the required production procedures. Here are also specified the activities that the doctorate candidate took part in during her work.

5.4.1 Quality Control 1 (QC1)

QC1 refers to the fabrication of chamber components, i.e. the first step in production of RPCs. The first stage of the QC is performed at the production sites. It consists of the procedures and requirements that need to be followed and accomplished in order to certify the components good for chamber assembly.

At the HPL production site QC1 includes all the steps in the production of HPL sheets, i.e. production of the HPL foils, quality check for resistivity measurement, check for the surface quality, cutting of the foils to the requested size and surface cleaning (see sec. 5.3.1).

At the Gas Gaps production site (see sec. 5.3.2), QC1 procedures are also performed with inspecting of the arrived HPL sheets for defects in color, scratch on the surface and mechanical damages on the edges and corners.

All the quality procedures implemented in producing of the other components of the RPC chambers are also part of the QC1. These include producing and testing of the electronics (Frond End Boards and Distribution Boards), cooling systems, as well as mechanics and readout strips (see sec 5.3.3 and 5.3.4).

5.4.2 Quality Control 2 (QC2)

The QC 2 protocols refer to the RPC gas gaps. They include all the steps of producing, testing and certifying of the detecting elements of the RPCs.

At the Gas Gaps production site QC2 refers to gaps production procedures of graphite coating, PET film coating, spacer bonding and gas leak test, as well as linseed oil treatment and high voltage test for measuring and monitoring of dark currents (see sec 5.3.2).

Once finished all the checks the approved gas gaps arrive at the assembly sites. In CERN, BARC and Ghent University some of the tests performed in Korea are repeated in order to ensure the good quality of the detecting elements before assembling them in a chamber. This is required due to the large distance transportation of the gas gaps, which includes air flights and handling at the airports as well as delivery procedures to the respective assembly sites.

Here are described in details the quality control procedures followed by the doctorate candidate, during her work on assembling RPCs in CERN.

Figure 5.17: Taking the gas gaps out of the transportation boxes

First step of the quality check on assembly sites is taking the gas gaps out of the transportation boxes, shown in figure 5.17. Once taken out, each gap goes through visual inspection, which is the second step of the quality check. During the visual tests, as shown in figure 5.18, gaps are characterized with a detailed checklist, ensuring that no visual damages, such as bending, bubbles on the surface, neatness and shape of the corners etc., are present and gaps are eligible to be used for chamber assembly. Results written in the checklists are then written into database, so than all the history of the components is accessible at any time.

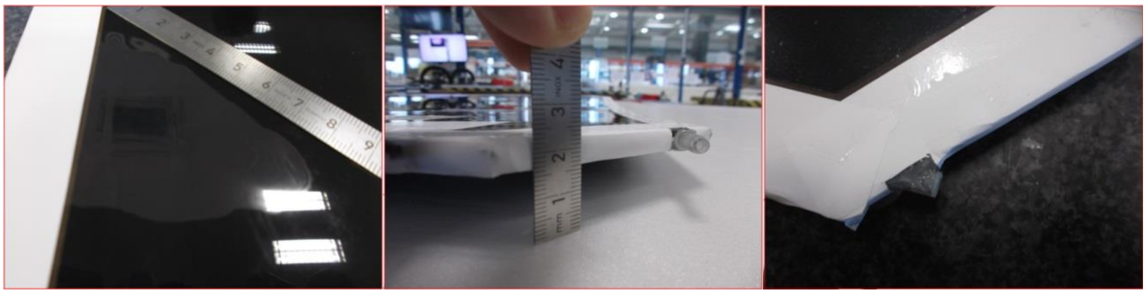

Figure 5.18: Visual test of the gas gaps, showing some problematic detecting elements.

Leak and spacer tests are then used to evaluate the mechanical properties of the gas gaps. The gas tightness test is performed using a pressure sensor and is controlled by measuring the stability of applied overpressure in a fixed time of 600s. Two leak tests at 15 mbar and 5 mbar are performed. The second measurement of the leak rate is used as a reference value for the final commissioning phase, since conditions are similar to the working environment in the CMS detector. Pressure drop should not exceed 0.4 mbar, and any gap having larger leak is rejected. Figure 5.19 shows a typical leak test and pressure change obtained at the performed spacer test for a given gap is shown in figure 5.20.

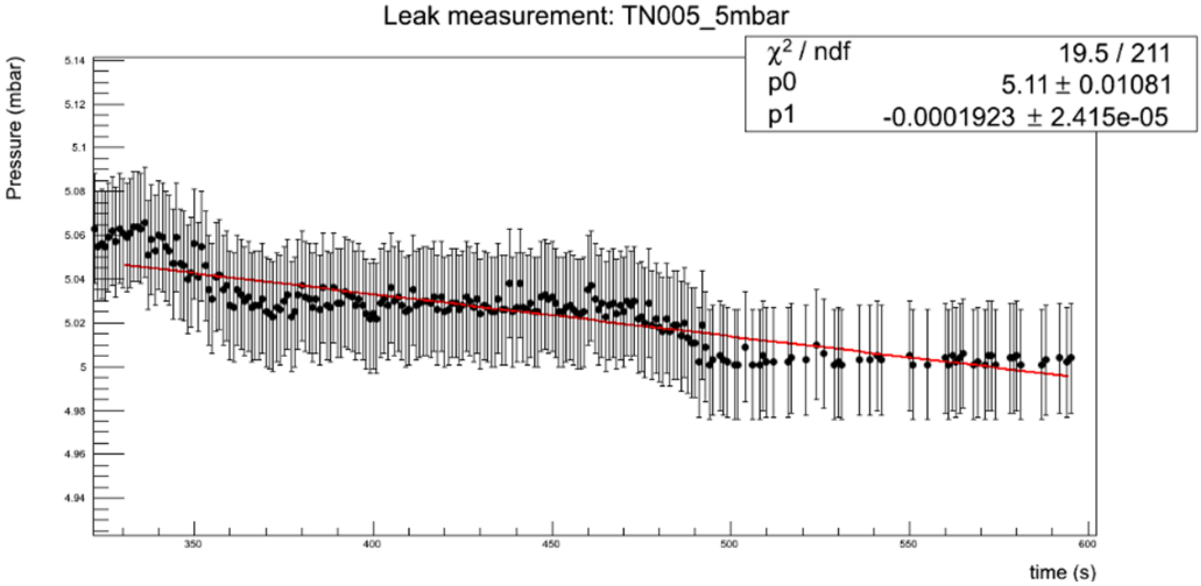

Figure 5.19: Typical leak test performed to the gas gaps.

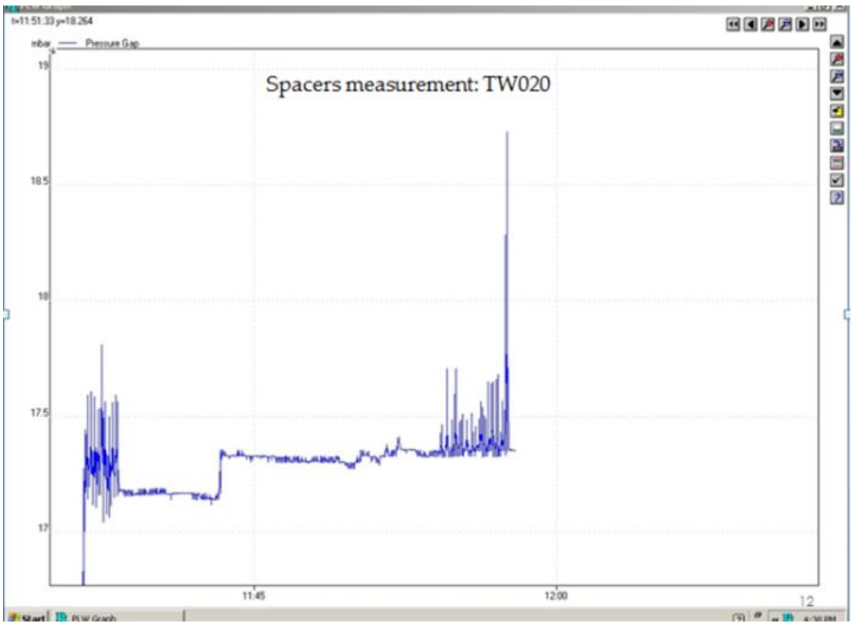

Figure 5.20: Typical spacer test performed to the gas gaps, where there are no detached spacers since the last peak in the pressure change is a non-spacer region used as a reference.

Spacer test is performed in order to determine the 2 mm uniformity between the bakelite sheets of gaps. This uniformity is maintained by a grid of (10cm x 10cm) button spacers between the bakelite sheets (see sec. 5.3.2). Though tested at the fabrication site, these spacers can get detached because of different reasons, such as insufficient bonding of the glue or mishandling of the gas-gap crates at the delivery. Even a single detached spacer is not accepted and leads to rejection of the tested gap.

Spacer test is performed at overpressure of 15 mbar [120]. A template of 0.2 mm thick PET (polyethylene terephthalate) film with known shape and positions of the spacers is placed over the gap. Each spacer is pressed and the results for pressure variation are recorded. The fluctuations in the pressure for intact spacers are in the range of ±0.5 mbar, while a popped up spacer is resembled by applying the same pressure in the non-spacer region, where the pressure change is much larger (±1 mbar and more), as shown in figure 5.20.

The last test in QC2 is the high voltage (HV) scan which main aim is measuring the dark current and its stability over a period of 3 days. The scan is performed by ramping the HV from 1 kV to 10 kV with steps of 1 kV up to 8 kV and a step of 100 V between 8 k V and 10 kV, while during the stability period, the HV is kept at an effective working point of 9.7 kV, correcting for pressure and temperature variations. Figure 5.21 shows a typical scheme of applied HV, while figure 5.22 shows the dark current measured during stability test at QC2.

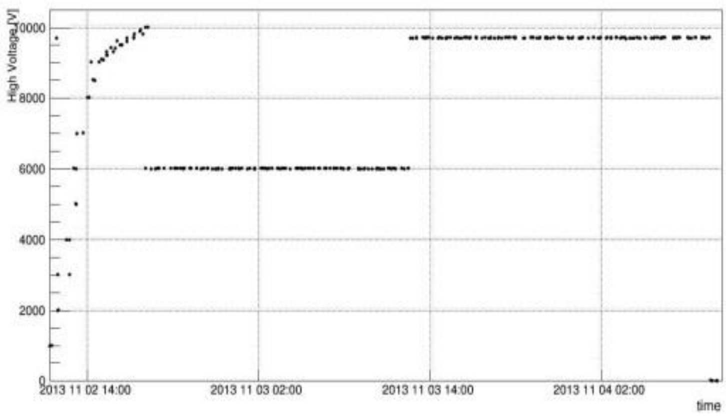

Figure 5.21: Scheme of the applied HV for a 3-day-period test at the QC2.

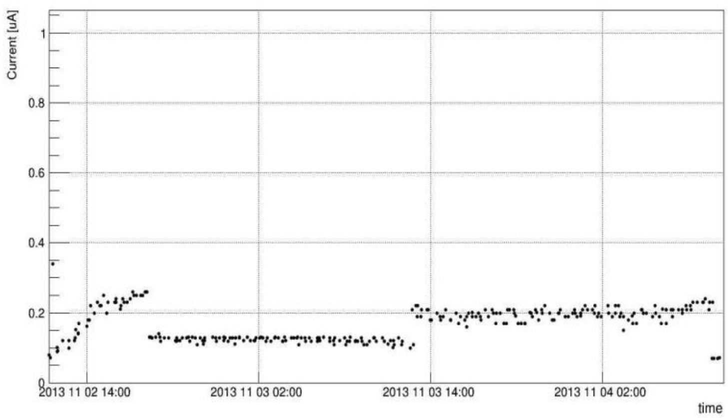

Figure 5.22: Sample of the current stability obtained after a 3-day-period test at the QC2.

Gas mixture used while performing the HV scan and stability test is the same as the one adopted by CMS – 95.2% $C_2H_2F_4$ (Freon), 4.5% iC_4H_{10} (Isobutane), 0.3% SF_6 (Sulfur hexafluoride) with 8000 ppm of water vapor added. Rejection limit for dark current is set to 5 μm. Once the gas gaps pass the mechanical and the electrical tests acceptance criteria, they are ready for assembly into an RPC. There has been found an overall rejection factor of 10% at QC2.

5.4.3 Quality Control 3 (QC3)

The third part of the quality control [115] requires the most sophisticated level of certification, since it is related to assembling and testing of the new RPC detectors. It is divided into two parts – QC3.1 considers the chamber assembly, and QC3.2 evaluates real physical parameters of the newly built chambers.

In this section a detailed description of all the QC3 steps is given, starting from assembling procedure to final decision of acceptance or rejection of a chamber. The doctorate candidate participated in all the described activities during her work in CERN.

When a set of three gaps with the required geometry is fully validated, these are used to start the chamber construction. The quality control at this stage of detector production goes through chamber visual inspection, gas tightness, electrical and dark current measurement (QC3.1), as well as cosmic muon commissioning by means of a dedicated cosmic ray stand (telescope) (QC3.2).

- QC3.1. Chamber assembly –

While under visual inspection, each chamber needs to pass through a detailed checklist for all its components in order to validate the manufacturing process of the chamber.

Figure 5.23: Mechanics preparation for chamber assembly – putting Mylar and insulation tape.

The assembly steps follow the standard procedure [76] – first the aluminium frame is prepared for gap installation using Mylar and insulation tape, as shown in figure 5.23. Then holding bars fixing the gaps into place are insulated using tape and put inside the frame, as shown in figure 5.24(a). Next a copper sheet is laid onto the frame and cleaned carefully with Isopropyl alcohol ($(CH_3)_2CHOH$), as shown in figure 5.24(b).

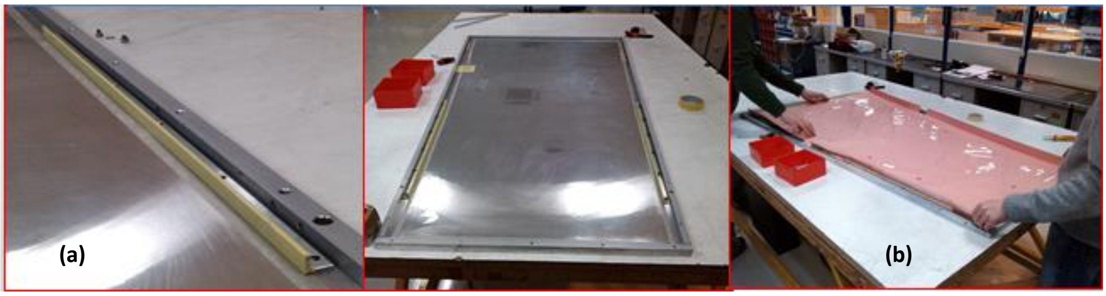

Figure 5.24: Mechanics preparation for chamber assembly – fixing insulated holding bars into place (a) and laying Copper sheet onto the frame (b).

When the frame is ready, preparation of the bottom gap begins. It is carefully cleaned and put inside with the HV cable at the bottom. Once it is sled into place, gas pipes are installed and read out strips are laid onto it. Top gaps are then cleaned and put onto the readout strips with the HV connection on top (figure 5.25). Gas pipers are installed and closing part of copper sheet is put to cover the top gaps.

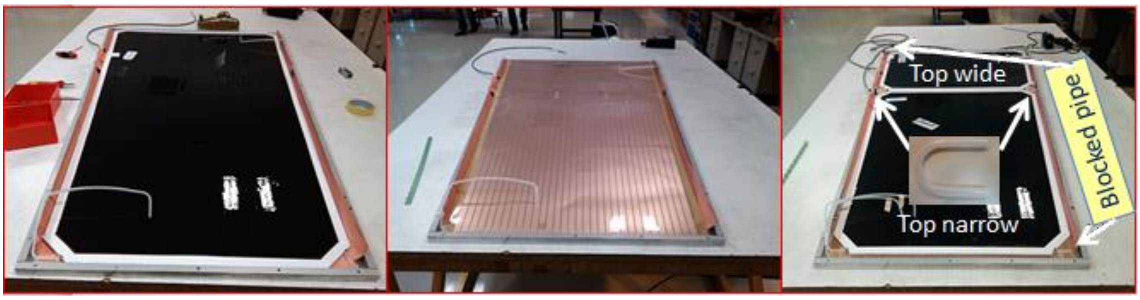

Figure 5.25: Chamber assembly – putting bottom gap and gas pipes (left), placing readout strips (middle) and top gaps with gas pipes (right).

Once the HV openings are cut, the copper sheet is closed. Next step is attaching the ground pins of cables to ground (copper sheet) and soldering them to the readout strips, as shown in figure 5.26(a). Strip connectivity test is performed in order to evaluate if signal cables are soldered correctly to the readout strips.

Aluminium frame cover also needs to be prepared before being laid onto the copper sheet. The cooling system is mounted into place and Mylar sheet of the same dimension as a Frond End Board (FEB) is cut and placed over its copper pads. Then FEBs and Distribution Board (DB) are installed onto it.

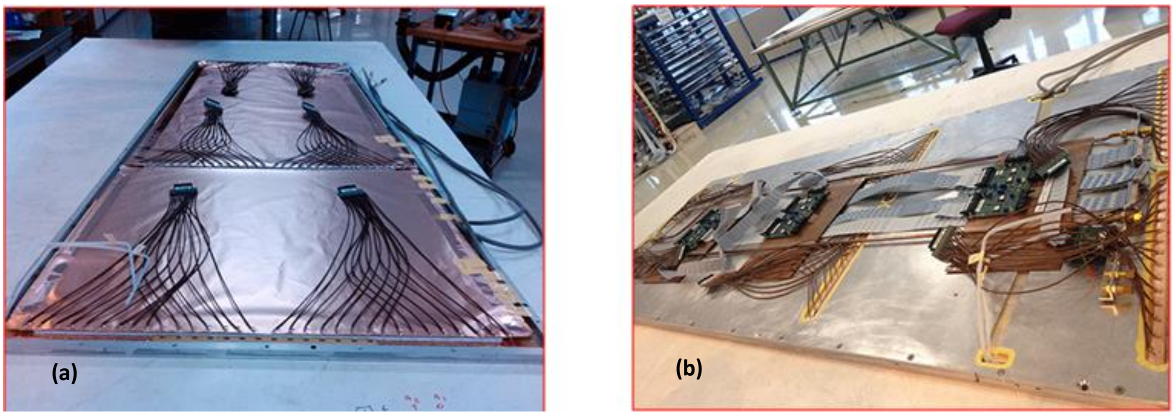

Figure 5.26: Chamber assembly – soldering signal cables (a) and closing the chamber with aluminium cover (b).

Final step in chamber assembly is placing the aluminium cover on top of gaps and carefully taking out all the gas inlets and signal cables (figure 5.26(b)). Frame is then closed with screws and patch panel is fixed (signal cables from FEB, gas pipes, HV cables are all fixed to the patch panel). Schematic view of the flat cables connecting FEBs is given in figure 5.27.

Once the chamber is closed, it's time for the leak test, which measures the chamber gas leak. This test is done in order to check whether, during chamber assembling, the gap gas inlets are correctly connected to chamber service panel. The procedure is the same as the one at the gaps leak test, so criteria for accepting the chamber is pressure drop to be less than 0.4mbar/10min (see sec 5.4.2).

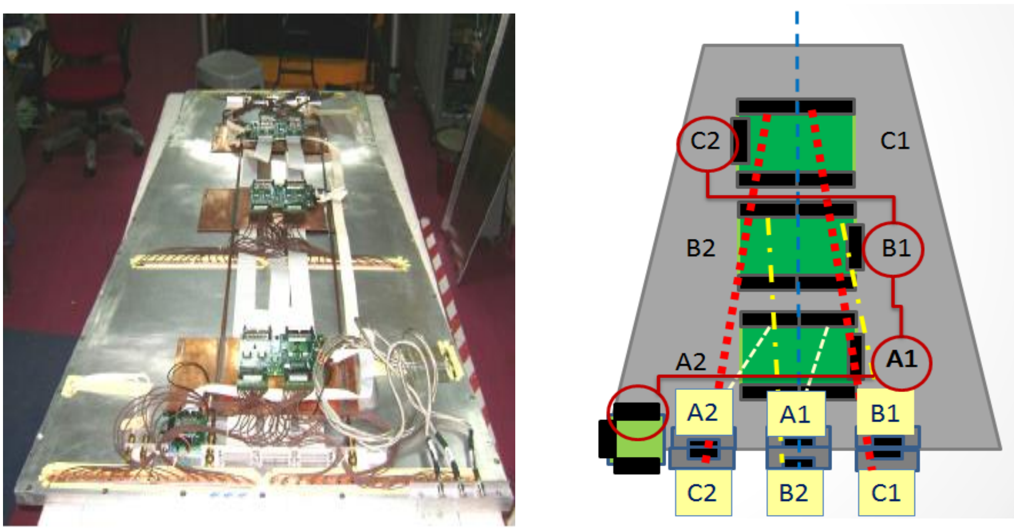

Figure 5.27: Real and schematic view of the cables connecting the FEBs on the cover of an RE4 chamber.

Next step is performing the electric test over the FEBs of the newly assembled chamber. It is done by powering and checking the thresholds of the Frond End Boards, while gaps are subjected to a high voltage scan. The threshold of the FEBs is set to 220 mV – 230 mV, which ensures that electronics accept only the signals from particles passing, thus limiting noise induced signals (see sec. 4.3.3). This test ensures that the RPC gaps operate without problems.

- QC3.2. Chamber performance evaluation with Cosmic rays –

The final procedure in the QC3 protocol is the chamber by chamber performed high voltage scan that aims at characterizing detector response while measuring main detector performance parameters such as efficiency, cluster size and noise [115]. This scan is performed at the RPC cosmic stand (telescope) [121] in each assembly site, shown in figure 5.28.

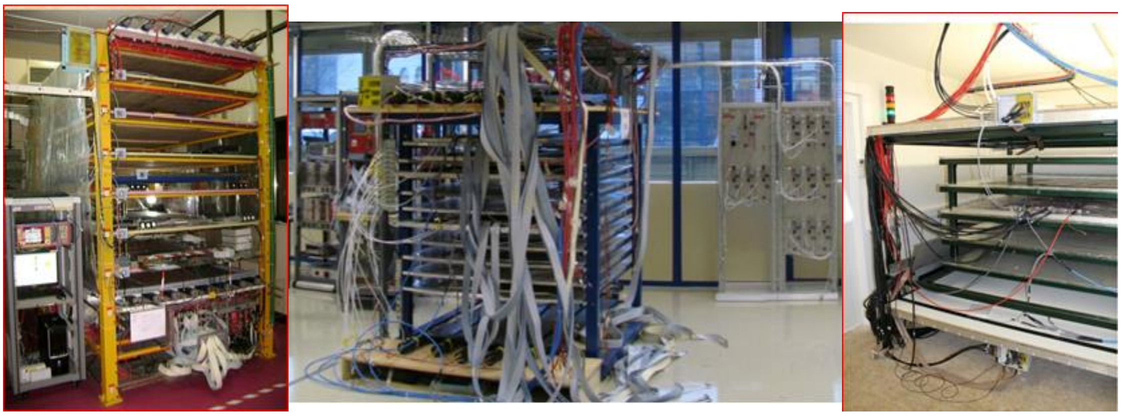

Figure 5.28: Cosmic ray stand (telescope) for chamber performance evaluation – BARC (right), CERN (middle) and Ghent (left).

The experimental setup used for cosmic rays (see sec. 1.4) tests is built up by a number of systems – high voltage power supplies, gas flow rate controller, gas mixture, trigger system and data acquisition system. Special devices are used to monitor the humidity and temperature in the laboratory, and air-conditioning systems are used to keep the temperature constant.

The cosmic rays stand consists of metallic towers where up to ten chambers can be placed horizontally and read out in coincidence with the passage of triggering muons. The trigger system is provided by two layers of scintillators [122] placed at the top and at the bottom of the test stand. In CERN where the doctorate candidate took part in this analysis, each scintillator layer is segmented in five readout active area with a total surface larger than the detectors under test. The data taking process begins when a cosmic ray is incident on both scintillator planes, and then efficiency can be calculated based on the detection of the cosmic ray in the chambers. The output of triggering layers is connected to chambers in a logical “AND” [123].

The gas mixture is composed of 95.2% $C_2H_2F_4$ (Freon), 4.5% iC_4H_{10} (Isobutane) and 0.5% SF_6 (Sulfur Hexafluoride), while the gas system is based on mass flow meters and controllers, which help monitoring the gas composition.

The high voltage power supply is provided by CAEN unit. Two VME crates built up the DAQ system. They are housing 15 TDC modules, which process the LVDS signals after amplification and discrimination.

When charged particles (mostly muons) ionize the gas of the RPC, an avalanche is formed in the gas by multiplication. The induced charge on the external readout electrode is produced by the anode-collected avalanche charge and represents the prompt signal of the RPC. The RPC readout strips are connected to the FEBs by co-axial cables via the Adapter Boards. FEBs are then connected with the TDCs, which open a 25ns window and readout all the signals coming from the readout strips and then transfer this information to the computer.

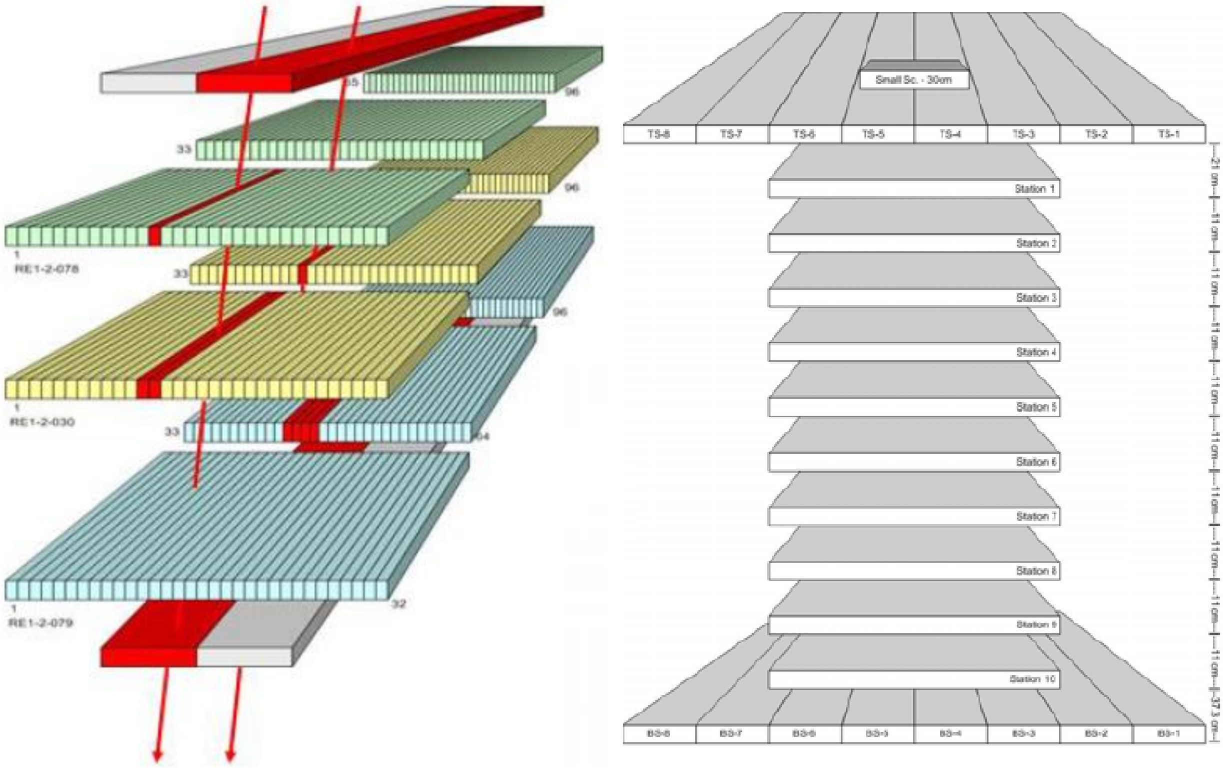

Figure 5.29: Schematic view of a cosmic test stand [124].

Three reference chambers installed at the stand are used by the analysis routine to perform a tracking algorithm in order to reconstruct cosmic muon tracks. The adoption of three RPC detectors allows the removal of any fake trigger given by the larger scintillator area, to reject cosmic showers and to reconstruct muon tracks. An offline analysis routine performs a tracking algorithm fitting the position of the fired strips of the three detectors in the 3D space. Only events with a track in both scintillator layers are taken into account. These events are then reconstructed using the signals from the hits in the reference chambers and based on these – a track of the passing particles is built.

A cosmic muon track is taken as correctly reconstructed only if there are hits corresponding to its track in at least 2 of the reference chambers, apart from both scintillator layers. Summary plots are displayed using different scripts and the summary of the chamber performance is kept in the RPC Production Database, so that data for each chamber is accessible through web interface. A schematic view of a typical cosmic stand is given in figure 5.29.

Each detector is subjected to three independent efficiency scans using three different configurations – double-gap, top single-gap and bottom single-gap, shown in figure 5.30. This is done because the RE4 chambers are based on double-gap RPCs. During each efficiency scan, there are 7 runs taken at different effective HV, from 8.5 to 10 kV. In each run there are 10k events collected in approximately 2 hours.

Each RPC chamber gain should be maintained constant against environmental changes. This is done by using air conditioning systems for maintaining a constant temperature in test facility. Yet, in order to be completely sure there is no environmental dependence on the chamber performance, the HV scan is performed using the effective high voltage HV_{eff} to correct the applied one on the chamber.

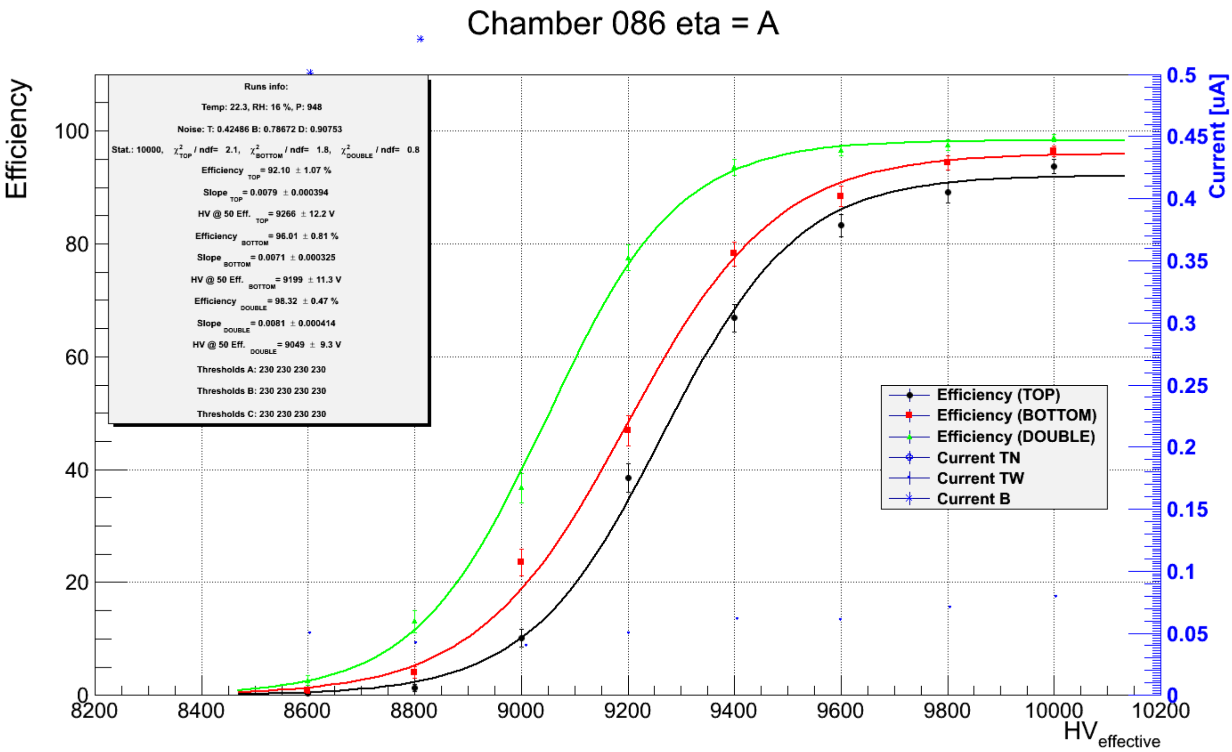

Figure 5.30: A typical HV efficiency scan performed at the Cosmic rays stand.

This is done according to the correction given by Eq. (5.1) [125]:

$$HV_{eff} = HV \frac{p_0}{p} \frac{T}{T_0} \quad (5.1),$$

where $T_0 = 293^{\circ}$C and $p_0 = 965$ mbar are the reference temperature and pressure.

A summary of the chamber performance (efficiency, dark current, cluster size, noise rate, etc.) obtained after the final Cosmic rays test is accessible through web interface, as it is stored in the RPC Production Database together with all the information about the environmental conditions at which the test was taken (see sec. 5.5). A typical HV efficiency scan is shown in figure 5.30.

Finally, after passing the Cosmic rays test, connections for each chamber are double checked and the Frond End panel is covered with the aluminium cover. Chambers are ready for the next step of the quality control – QC4.

5.4.4 Quality Control 4 (QC4)

The last stage of quality control on chamber level for the newly built RE4 detectors is the QC4. This quality control is performed in CERN, where all the newly built chambers from all the three assembly sites are transferred. At QC4 the quality certification is divided into two stages.

- QC4.1. Chamber parameters evaluation –

This stage of the quality control refers to double-checking all chamber parameters in order to ensure they are still in the required range [126]. It includes Connectivity test, Electrical test and Leak test.

In the beginning of the connectivity test, a visual inspection of all chamber electronics is performed. Frequency meter is used to check for bad or disconnected strips, to make sure there are no dead or too noisy chambers. The proper working of the strips is checked by sending a direct signal from the frequency meter to the strips and then reading it back.

The electrical test is performed in two steps – by sending analog and digital signals to Front-End Boards (FEBs) and by checking their thresholds. For analog signals the current should be less than 0.42A, while for digital ones it should not exceed 0.91A [126]. Each chamber should draw about 0.36A from the analog power supply (PS) and 0.75A from the digital PS, adding about 50-100mA for the Distribution Board. Chambers, which fail to pass these criteria, are not taken into the next step of production – assembling of Super Modules. The second step in the electrical test is performed by checking the thresholds of the FEBs, which should be 215mV. In case some difference is found, the threshold is then adjusted and chambers are ready for next tests.

The gas leak of the RPCs is classified in four kinds in the Gas Leak test – Large, Normal, Acceptable and No gas leak. The test is performed by measuring the pressure drop for each chamber in a time interval of 10 minute, accepting that conditions are stable. Measurements are then taken by a special tool provided by the CERN Gas group – Gas Leak Box. All chambers which pass this test are then submitted to HV scan, which is the next step in the quality control.

- QC4.2. Long Stability test –

After passing QC3 tests, all chambers have three HV jupiter connectors – one for each gap accordingly. One of the procedures that RPCs undergo during QC4 is changing the HV jupiters by a tripolar connector. This requires performing a new HV scan in order to make sure chambers are working within expectations after this procedure. The HV scan test begins with applying 1kV to each gap, so that broken connections and electrical short circuits are detected. Then the high voltage is raised every 10 minutes by 1 kV until it reaches 8kV. The gas avalanches begin to develop at 9 kV, which is reached by changing the raising step to 0.5kV (after passing 8 kV). Finally, the high voltage is raised up to 10kV in steps of 0.1kV. Figure 5.31 shows an example of the response of an operational chamber to the HV scan test.

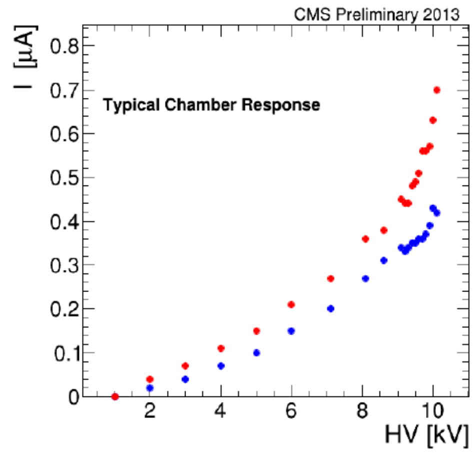

Figure 5.31: A typical chamber response in HV scan test.

After passing this HV scan, chambers are then submitted to the Long Stability test, which is the main accent of the QC4 control procedures [126]. This test is performed for 4 continuous weeks with a constant monitoring of the chamber current at 2 HV values. The test is performed at cycles of 12 hours, where chambers are kept at 9.7 kV for 10 hours and then at 6 kV for 2 hours in order to observe the behavior of the ohmic dark currents of the gas gaps. The chamber is rejected and not used for further assembly if the dark current is too high or has a rising trend over the test period. This cycle is repeated more than 5 times for the 4 weeks of testing.

During this stage, the chambers are connected with CMS mix gas at 1 atm pressure, which requires a correction of the value of the HV according to the pressure of the CMS mix gas – when the pressure of the gas increase, the HV is increased, and when the gas pressure is decreased, the HV is also decreased.

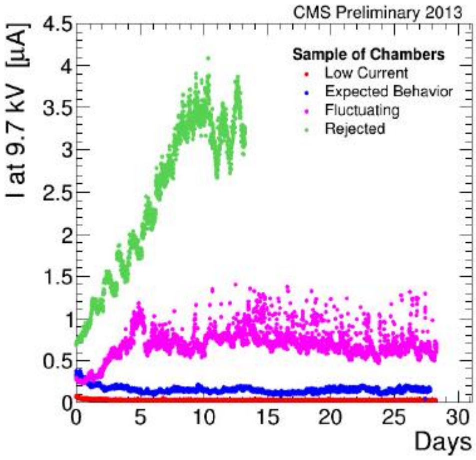

Figure 5.32: Different typical behaviour for chambers under Long Stability test.

Figure 5.32 shows the four main behavior trends of the chambers undergoing Long Stability test. The case of high resistivity is shown in red – here the current in the chambers is very small, but different than zero. The expected behaviour, when the current of the chamber is within a well-defined interval is shown in blue. The nervous behaviour is shown in purple – the current in the chambers is dispersed within a wide interval, and the rejection behaviour is shown in green – here the current is always increasing, which indicates there is something wrong with the chamber.

5.4.5 Quality Control 5 (QC5)

After passing the QC4 Long Stability test, the RE4 chambers are integrated into 10 degree sector units called Super Modules (SM). The process of assembling these Super Modules refers to the last stage of the quality control.

Each Super Module consists of two RPCs – one small (RE4/2) and one big one (RE4/3). They are connected together to form a 10 degree sector of the RE4 Endcap disks, shown in figure 5.33. There is a total number of 72 Super Modules – 36 per each disk, which are assembled and tested before their actual installation on CMS.

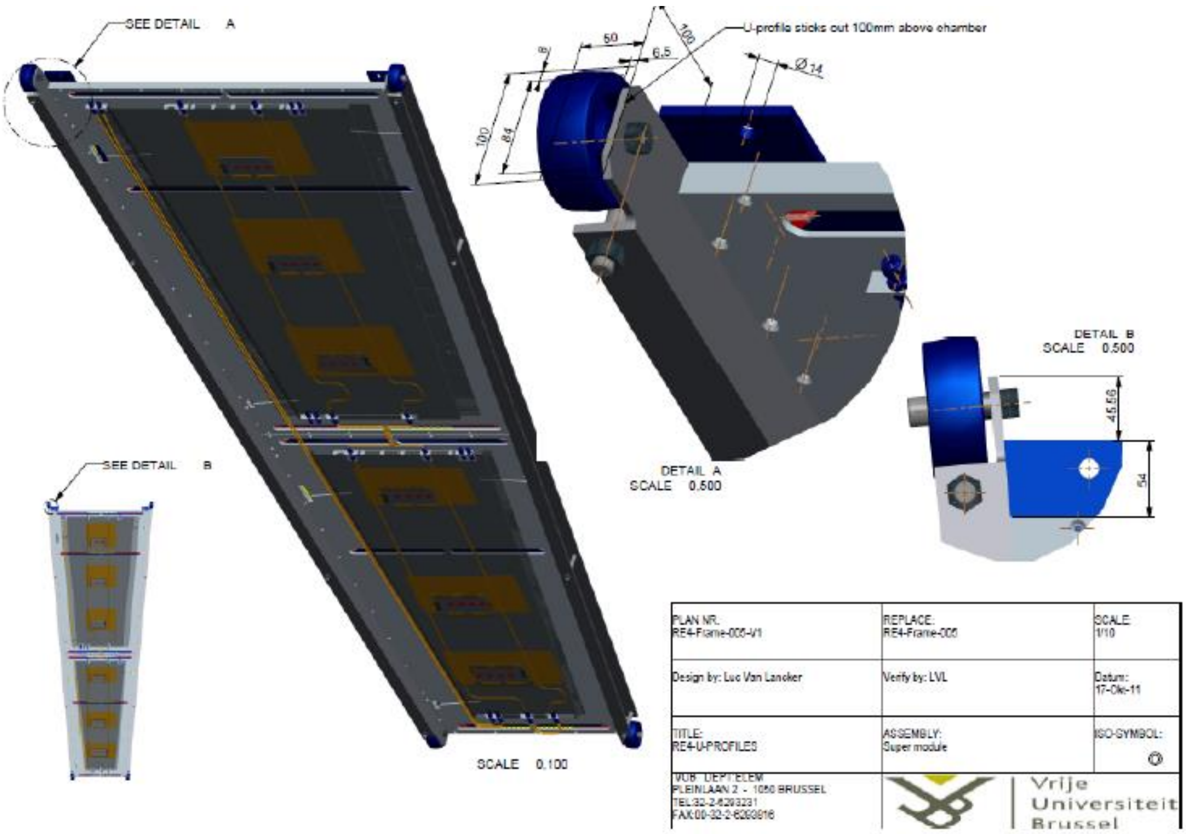

Figure 5.33: Schematics of an RE4 Super Module covering a 10 degree sector with handling frame.

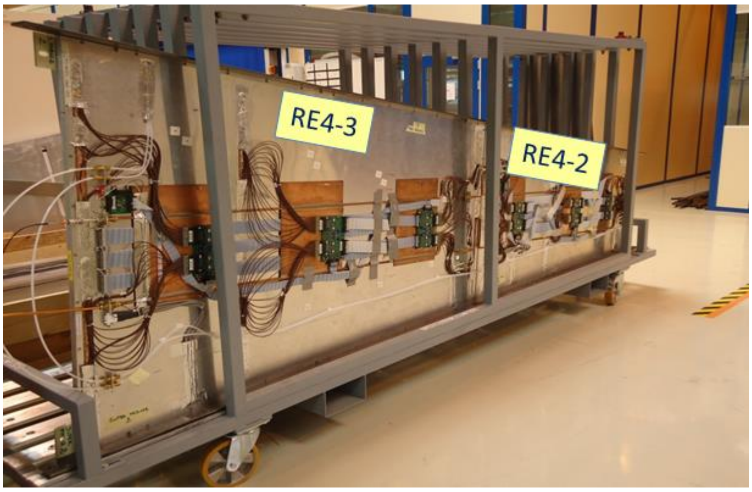

Figure 5.34: RE4 Super Module ready for installation on the CMS Endcap disks.

Last of the quality control procedures, after integrating the two chambers into one SM, is the test of the Cooling system. It is performed by filling up the cooling tubes with water at high pressure, in order to ensure there are no leaks either in the tubes (some damage can occur during the transportation), or in the connectors joining the coolings of both chambers. Figure 5.34 shows a Super Module, which is ready for installation after passing the cooling system test.

5.5 Performance and installation

Storing the full history of every component and each assembled chamber in the RPC Construction Database is useful not only for tracing back all the assembly steps, but also for evaluating the overall performance of the newly built RE4 chambers.

5.5.1 Chambers performance

The summary of the RPC detector performance [115] starts at assembly sites with evaluating the overall gap performance during QC2.

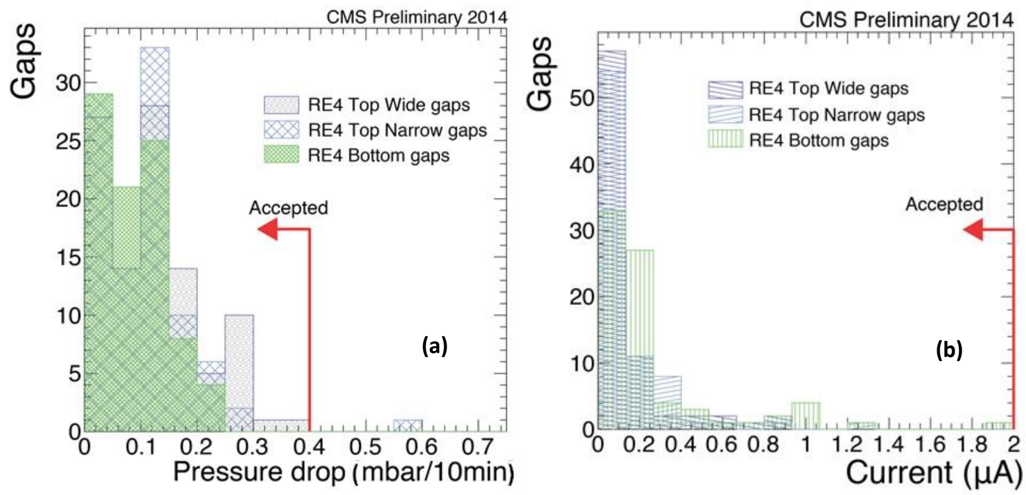

Figure 5.35: Leak rate (a) and dark current (b) distributions of gaps adopted for the RE4 detector construction

Figure 5.35 shows the overall distributions of the gaps performance after the QC2 Leak and Dark Current tests, which are obtained at 20 mbar and 10kV accordingly (see sec. 5.4.2). The Leak test is performed measuring the leak drop in time for each gap, which should be less than 0.4 mbar/10 min, while the dark current is measured while performing an HV scan to the tested gaps. Limit for dark current rejection is 5 μA. At QC2 an overall rejection factor of ∼10% has been found. It is due to irreparable damages which have occurred during chamber construction and gap transportation.

After the gap performance evaluation is the turn of QC3 where the assembly sites have to fully commission each detector. The full evaluation of the performance of the newly built RPC detectors under test is done using the cosmic rays telescope, where the first physical data is taken. On the basis of the cosmic muon data it is decided whether the chamber is accepted to be prepared for installation on the CMS detector or it should be rejected. The main parameters, which are evaluated and measured at this stage of control, are chamber efficiency, mean cluster size and noise rate, while dark current is monitored.The dimension of the cluster formed by all simultaneously fired adjacent strips is called **cluster size**. The cluster size of a chamber is defined as the sampled average value of the cluster size distribution in the first 25 ns of the trigger window of 100 ns.

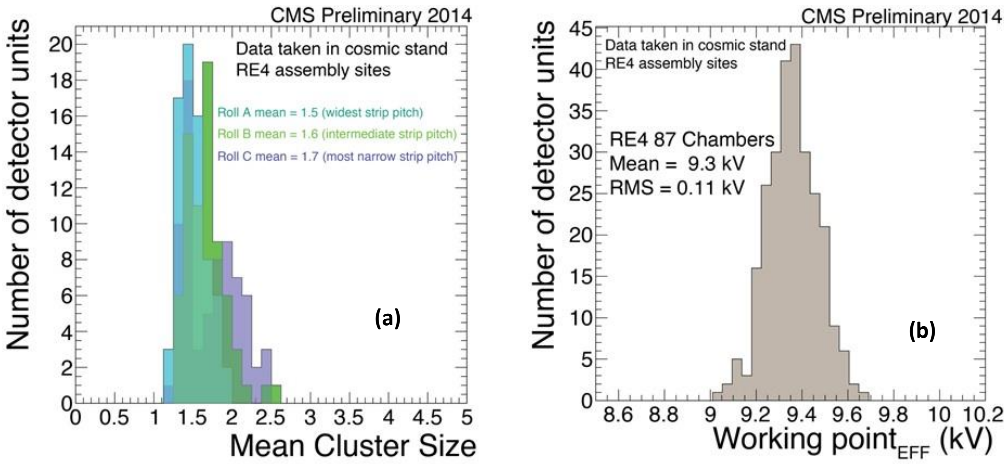

Figure 5.36: Mean cluster size (a) at the expected nominal HV working point (b) of commissioned RE4 detectors.

The average cluster size distribution, evaluated at three different η segments at the expected working point is shown in figure 5.36(a). The distribution of the expected working point is shown in figure 5.36(b). The expected working point is defined by adding 150 V to the measured efficiency at 95% in respect to the high voltage scan results (see figure 5.29).

The algorithm for obtaining **chamber efficiency** is based on the “coincidence” method – an evaluation on the ratio between the number of events in which RPC has at least one fired strip in the trigger window (100 ns) and the total number of recorded events is done [85]. There is also a correction for spurious hits. Chambers with efficiency less than 90% are rejected.

The efficiency along the high voltage scan and the fitting of the data points are described by the following equation (5.2) [85]:

$$\in = \frac{\in_{\max}}{1+e^{-\lambda\left(HV_{eff}-HV_{50\%}\right)}} \quad (5.2).$$

Figure 5.37 shows the overall average maximum efficiency in double gap mode (ε_{max}), while the high voltage at 50% efficiency ($HV_{50\%}$) and the slope distribution at

$HV_{50\%}$ are reported in figure 5.38. The slope is the derivative of the sigmoid HV function (see figure 5.30).

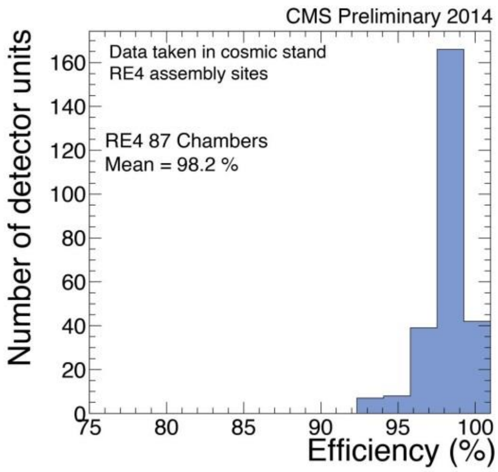

Figure 5.37: Average maximum RE4 chambers efficiency, extrapolated from the plateau curve (see eq. 5.2).

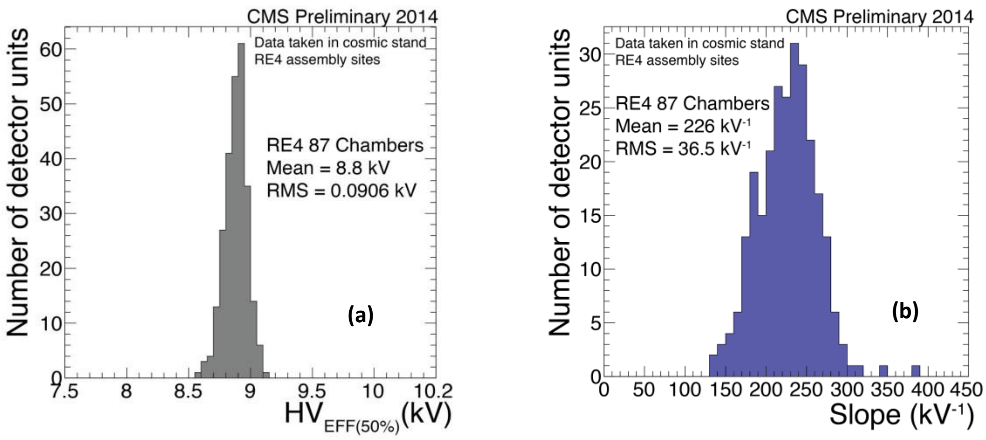

Figure 5.38: High voltage distribution at 50% efficiency (as defined in eq. gornoto) (a) and slope distribution (calculated at 50% efficiency) (b) for the produced RE4 chambers.

Another important parameter of the chamber performance is the **noise rate**. It is defined as the number of fired strips per second outside the trigger window, normalized to the surface of the strips. The noise rate is automatically measured in all the runs using an additional gate to the TDCs, delayed from the cosmic muon trigger. Efficiency and noise rate are kept in the proper limits using the threshold control on front-end electronic discriminators. The acception criterion for noise rate is less than 10 Hz/cm^2. Having a high rate only for a few strips in a chamber leads to a careful investigation, which often results in substitution of a faulty FEB. Evaluating the average chamber noise rate is done by masking the strips with hit rate larger than 20 Hz/cm^2. A sample noise distribution measured during an HV scan is shown in figure 5.39.

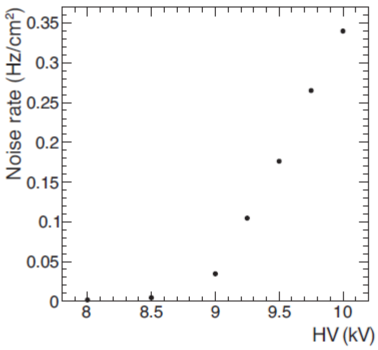

Figure 5.39: Sample noise rate measured during an HV scan of one of the detectors under test [114].

Less than 5% of the tested chambers are rejected for low efficiency and high current. All accepted after this stage detectors show high efficiency (> 95%), acceptable cluster size (average value ~ 2.5 strips) and low noise rate (< 5Hz/cm^2) [114].

Once fully commissioned all RE4 chambers from the three assembly sites go to QC4 tests, where their overall performance is monitored in time. The quality control procedures start with electrical test of the FEBs. Both analog and digital signal currents are measured (see sec. 5.4.4) and the response of a sample of the tested chambers is shown in figure 5.40. The current must be less than 0.42A for analog and less than 0.91A for digital signals. All tested chambers are in range.

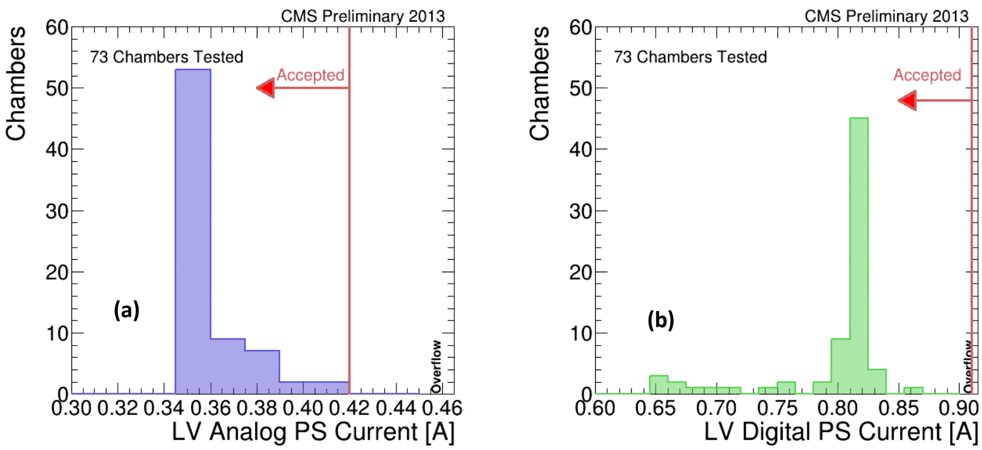

Figure 5.40: Signal current for analog (a) and digital (b) signals sent to Front-End Boards (FEBs).

Results from the performed QC4 gas leak test are shown in figure 5.41. The pressure drop is measured for each chamber in stable conditions for a time interval of 10 min. All tested chambers are in range – therefore all of them are accepted at this stage.

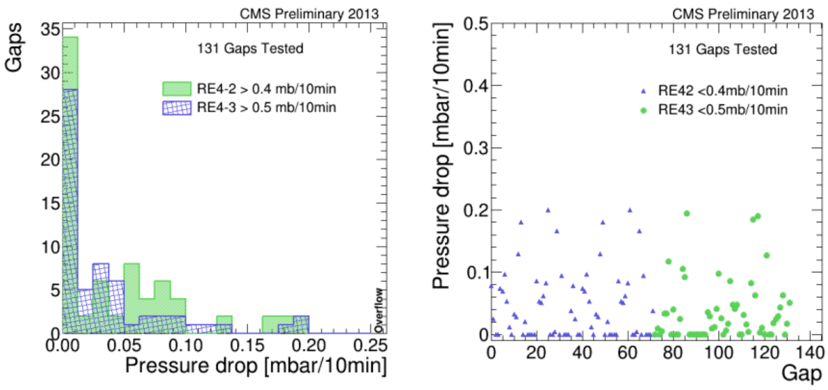

Figure 5.41: Pressure drops measured for RE4/2 and RE4/3 chambers.

The Long Stability test is the main accent of QC4. After three weeks of constant monitoring at two HV values (see sec. 5.4.4), chambers are accepted only if the ohmic dark current doesn't have a rising trend, isn't too high or its maximum fluctuation is less than 50%. Results are shown in figure 5.42.

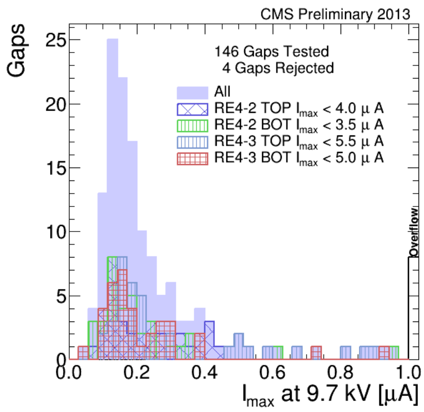

Figure 5.42: Pressure drops measured for RE4/2 and RE4/3 chambers.

All the chambers passing the QC4 Longevity test are mounted together as Super Modules. Once all connections on the gas tubes and the coolings are double-checked, the newly built RPC detectors are installed on the CMS experiment.

5.5.2 Installation and Commissioning

The RE4 project consists of 72 Super Modules (SM), each made by two RPC chambers – a total of 144 double-gap RPCs. The new detectors instrument two disks, called RE+ and RE-, located on the opposite endcaps of the CMS detector.

Installation of these Super Modules at the experimental site follows special protocols. These refer to SM orientation at the trolley coming from the construction site, storage space allocation at the experimental site, SM lifting, workforce, logistics and most importantly – teamwork.

SMs are transported from CERN construction site (building 904) down to the experimental shaft in specially designed trolleys – six SMs per a trolley. Each SM weights about 230 kg, which requires a special crane for lifting and positioning them on the detector, as shown in figure 5.43.

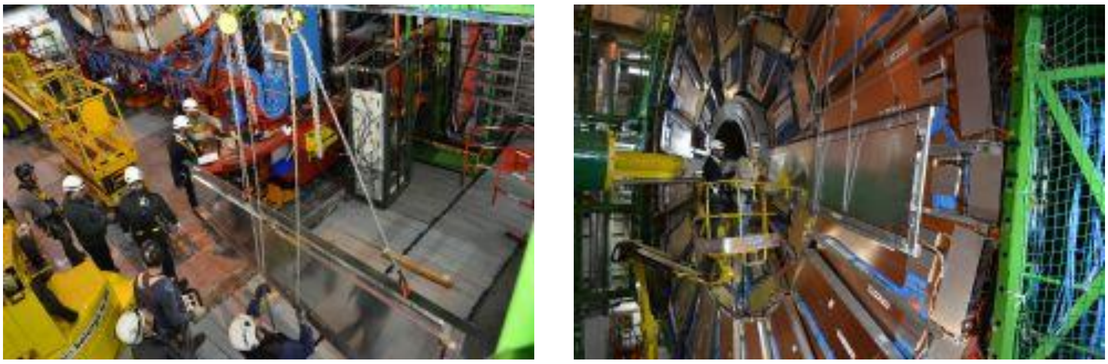

Figure 5.43: Lifting and positioning the first Super Module for the RE negative disk.

Once at place SMs are connected to the power and readout systems, as well as the gas and the cooling systems. A full disk is connected to the power and readout systems by using about 13 km of cable and more than 14000 connectors. The gas and cooling pipes are about 2.5 km long and their proper work is ensured by full testing before being connected to the chambers. Figure 5.44 shows a close view of the disk covered with RPC detectors.

Figure 5.44: Zoom of the RE4 negative disk, covered with RPC detectors.

The first disk is fully installed in December 2013, while the installation of the second one is done in the beginning of May 2014. Both disks fully covered with RPCs can be seen in figure 5.45. After the installation both disks are commissioned successfully in the beginning of RUN2 data taking – 2015.

Figure 5.45: Overview of the RE4 positive and RE4 negative disks fully covered with RPC detectors.

5.6 Conclusions

The RE4 project is multi-national collaboration project with more than 50 physicists and technicians from Belgium, Bulgaria, China, Colombia, Egypt, Finland, India, Italy, Korea, Mexico, Pakistan, Poland and Switzerland contributing in it. All of them have done their work, so that all the required RPCs are built, tested, transported and installed on the fourth endcap disks of the CMS experiment on time.

The doctorate candidate is part of the CERN team working on this project.

The tasks with the significant contribution of the doctorate candidate are:

1. Evaluation of the detecting elements (RPC gaps) in QC2 stage of production – visual test, leak and spacer tests.
2. Dark current test.
3. Chamber assembling during QC3 stage of production
4. Test of the newly built chambers at the cosmic rays telescope.

Work done by the doctorate candidate for the LS1 RE4 production is highly appraised by the RPC community. It is presented by the doctorate candidate in two conference talks, one poster awarded with the best poster prize and one scientific publication.

6. Performance of the RPC system during RUN2 at 13TeV

After a two-year technical stop during LS1, in May 2015, the Large Hadron Collider (LHC) at CERN collides for the first time protons at record-breaking center-of-mass energy of 13 TeV. This is the beginning of the high luminosity RUN2, which is still ongoing for the last three years. The LS1 is used by the Compact Muon Solenoid (CMS) detector for performing crucial tasks necessary for detector operation at higher energies. One of the main upgrades is done at the Muon system of the detector with servicing, re-commissioning and upgrading of the Resistive Plate Chamber (RPC) system with 144 new chambers to enhance the muon trigger efficiency.

This chapter presents the main concepts behind the new high-energy data analysis done by the CMS RPC collaboration. Obtained results on the system performance over time are also shown. Special focus is given to the RPC performance studies in which the doctorate candidate participate during RUN2 – monitoring of the main system performance parameters like efficiency, cluster size, working point calibration, etc.

6.1 Data analysis

Here are presented the steps of the data analysis in which the doctorate candidate is taking part during RUN2 data taking.

6.1.1 Data selection

One of the major components of data analysis is data selection. At the CMS experiment, data taken at the same conditions is grouped in separate sets called runs. A given run is stopped whenever there is a problem with data collecting – either a detector one (hardware or software), or due to beam dump at the LHC. Once the problem is solved and data collecting starts again, a new run is started. Due to simplicity and convenience, runs are numbered in succession.

It is important to have a specific data selection for evaluation of RPC system performance due to some requirements in data analysis algorithm, as well as statistical reliability of the final results [127]. Current analysis is performed over data from collision runs taken in 2015, 2016 and 2017 at 13 TeV. The presence of stable beams is one of the major requirements. Runs under analysis are at least one hour long and have all CMS Muon systems (DTs, CSCs and RPCs) (see sec. 3.6) collecting data in the Global data taking and working at their optimal working points. This is required due to different data taking conditions, when one or more sub-systems have some problems and are taken into local running for calibration and diagnostics.

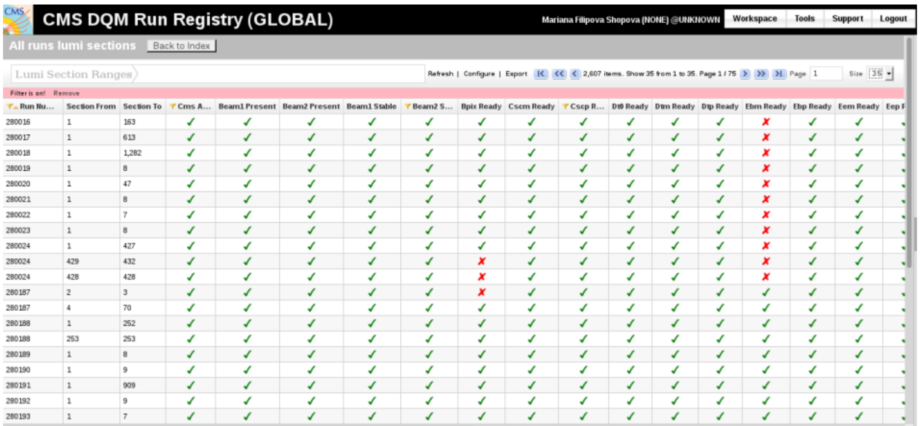

Figure 6.1: A view of the CMS Run Registry (RR) with possibility of applying different selection criteria over data.

The CMS detector should be active and the magnetic field is required to be at 3.8 T. A special CMS tool, where all the data taking conditions are stored is used for data selection – the Run Registry (RR). Figure 6.1 shows a view of how different data selection criteria are done in RR.

Once the selection is applied, the required analysis information is written in text files in JSON format. The analysis code then uses these files to enter the data of interest. In the JSON files is stored information on the run number and the good Lumi-Sections (LS) which make all the criteria. A lumi-section is a unit of accounting for integrated luminosity. It is a sub-section of a run during which time the instantaneous Luminosity is unchanging (2^{20} orbits ~23 seconds) [128].

6.1.2 Data analysis algorithm

The data used for physics analysis can be stored in different data formats with a great variety on the information included in each of them. The most commonly used one for data storage in CERN is the ROOT-file format. This file format allows a tree-based structure of the data, which makes the further analysis much easier.

For the RPC system analysis, the input data is taken from a special data stream – RPCMonitor stream [129], where different information is stored, in particular information on already reconstructed muon segment – on their quality, their direction and also where they are detected. Here also a very preliminary assessment on the particles momentum can be found. This input data is divided in different segments, which are then written in ROOT-file format.

The analysis code is using the segment extrapolation method (see sec. 6.1.1) to extrapolate the muon segments to the RPC plain. The entire code package is written, tested and enriched during a period of a few years by the RPC collaboration [130] and is used by the doctorate candidate, as well as the other scientists participating in RPC system performance analysis. Data processing is done using the CERN Worldwide LHC Computing Grid (WLCG) network, which allows quick obtaining of the required results.

The WLCG [90] is a specially designed hierarchy-like computing network, which has four levels ("Tiers"), called 0, 1, 2 and 3. Each Tier is a network of several computer centers providing a specific set of services. The Tiers process and store all data coming from the CERN experiments (see sec. 2.4) and can analyze a lot of different tasks in an approximately short time, or a lot of identical tasks in parallel. The WLCG main advantage is that each computer connected to the network is given a certain part of the entire task and all of them are computing simultaneously, which results in a significantly shorter processing time.

Using the WLCG network requires maintaining a few obligatory protocols. For the CMS experiment, each user should have a few software packages installed in order to be able to run the analysis:

- CMSSW – special software package for CMS data processing and analysis [131];
- ROOT – software package which specializes in processing of large high-energy physics (HEP) data volumes [132, 133];
- CMS Remote Analysis Builder (CRAB) – special software for submitting CMSSW jobs to WLCG computing sources [134];
- A few other packages, depending on the CMSSW version and the required analysis.

The analysis is performed in a few steps, which need to be followed strictly to ensure the proper running of the code and the reliability of the obtained results. The WLCG resources are used to obtain the necessary results. Acquiring the results from the submitted jobs can take from a few hours to a few days, depending on the amount of data to be processed and the availability of the WLCG resources. The resulting data, which is transferred back after being analyzed with WLCG, is written in form of histograms, kept in ROOT files format, which contain information on the luminosity, the efficiency, the cluster size, etc., for a given analyzed run. Finally out of those files, the information for different RPC system performance parameters is taken and plotted for further investigation (if needed).

A total amount of more than 249 TB of physics data is analyzed over the period of three years during the RUN2. The doctorate candidate is part of the analysis team contributing both in running the analysis steps, as well as new members' supervising.

6.2 Performance of the system

During the period of RUN2, the RPC system is running smoothly and collecting data for physics analysis. The performance of the system is closely monitored and studied. Here the results for the main RPCs performance parameters are shown, as well as their behavior in time. Special focus is given to the efficiency studies in which the doctorate candidate is participating.

6.2.1 Efficiency studies

This chapter presents a brief description on the used methodologies for RPC parameter monitoring. Results on the efficiency, cluster size, time and special resolution for the entire system are shown, as well as results on the performance of the newly built RE4 chambers. The doctorate candidate main contribution is in these efficiency studies.

6.2.1.1 Segment extrapolation method

The RPC efficiency is measured using the segment extrapolation method [130]. The idea is that detector efficiency can be measured by comparing its response to passing particles with that of another detector. The essence of the method comes from the specific geometry and design of the CMS muon system, which uses alternating layers of different gaseous muon detectors – DTs and RPCs in the central region and CSCs and RPCs in the endcap regions [76]. Having another muon detector next to each RPC chamber allows the use of local reconstruction in different muon sub-systems in order to define muon registration efficiency. Figure 6.2 shows the basic principle of segment extrapolation.

All starts at local reconstruction level in a DT or a CSC chamber, where the segment is defined. Standalone muon tracks are reconstructed without taking into account RPC hits in order to avoid biases. Only segments from DT in the barrel and CSC in the endcap, that belong to a standalone muon track are then selected and extrapolated to the plane of a given RPC. Each extrapolated hit is matched with a signal from the closest cluster of a few consecutive fired strips (only within the range of ± 4 strips). The RPC detector is considered efficient if an RPC reconstructed hit is found within ±4 strips from the position extrapolated from the DT/CSC segment. In order to avoid or reduce the fake events due to radiation background or wrongly reconstructed segments, additional condition is set – only segments associated with reconstructed muon tracks are used for extrapolation.

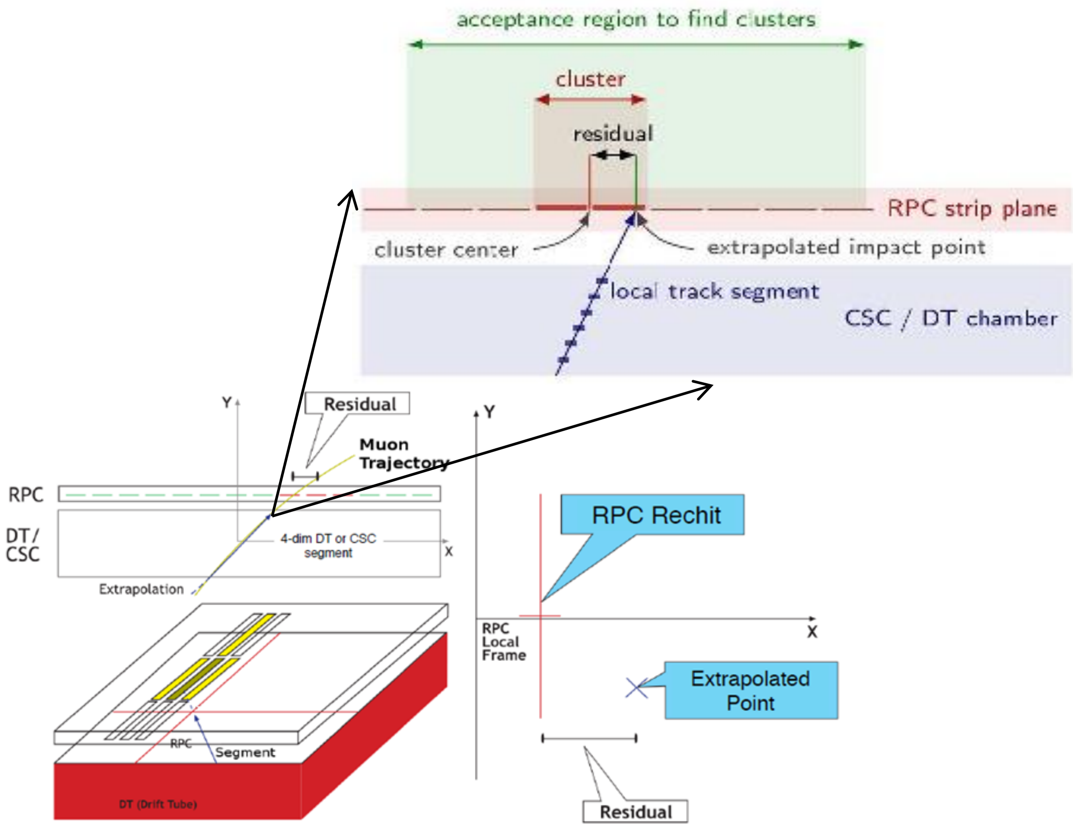

Figure 6.2: Scheme of the segment extrapolation method

6.2.1.2 Spatial resolution

The segment extrapolation method, described in the previous sub-chapter, is used also for estimating of the RPC spatial resolution. The main parameters defining the RPC spatial resolution are the residuals and the cluster size.

A consecutive set of strips, each collecting an induced charge, defines a cluster, while the number of the strips in the cluster gives the **cluster size**. The cluster size depends on the strip pitch and because of this it is higher for the innermost eta partitions and smaller for the outermost ones. An example is given in figure 6.3, where the plot shows the RPC cluster size for each roll of the newly built endcap Disk-4. The X-axis corresponds to the 36 sectors, and the 6 η partitions are shown on the Y-axis.

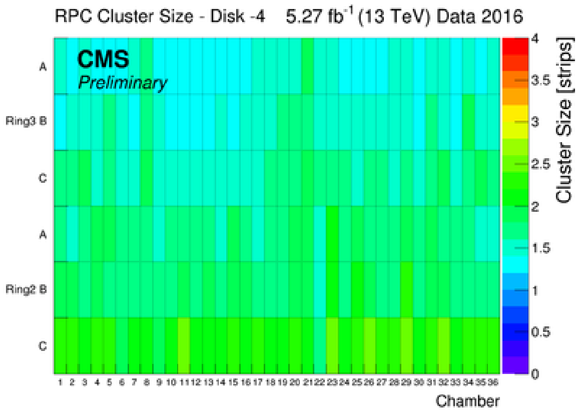

Figure 6.3: RPC cluster size map for endcap Disk-4.

Cluster size distributions for the both the barrel and the endcaps for 2017 13 TeV data are shown in figure 6.4. They are obtained using the Tracker extrapolation method (see sec. 6.2.1.6)

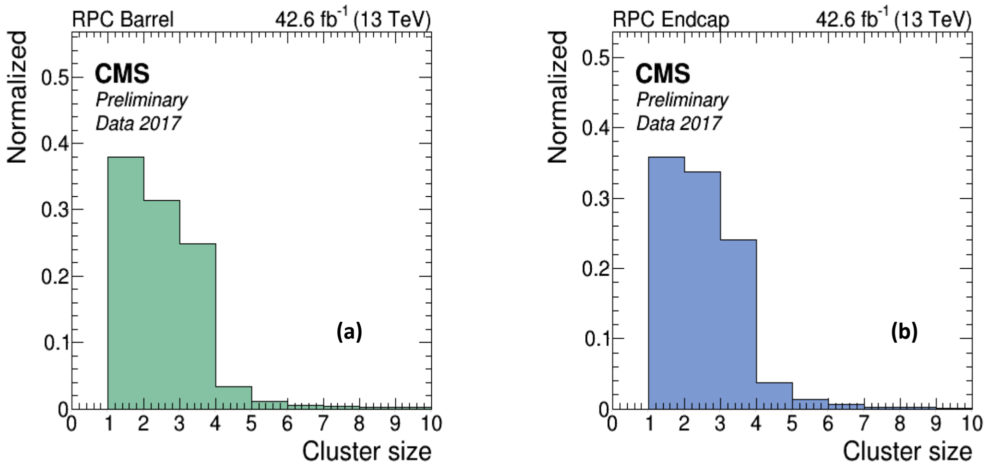

Figure 6.4: RPC cluster size distribution for the barrel (a) and the endcap (b).

Performed studies show that during RUN2 the mean value of the RPC system cluster size is ~ 2 strips, acting up to the trigger requirements for ≤ 3 strips included in the algorithm [76].

Residuals are calculated as the difference between the local x coordinates (transverse view of the RPC detection plane) of the extrapolated point and the center of the matched RPC reconstructed cluster, as shown in figure 6.3. Studying the residuals is important, since they are directly correlated to the azimuthal angle ϕ resolution. Any misalignment of the layers can affect the estimation of the bending angle of muon tracks.

Figure 6.5 show the residuals for all RPC barrel layers. The order of the layers is that layer 1 is the closest to the beam pipe, and layer 6 is the furthest from it. The residual distributions are fit to Gaussian distributions and the resulting values for the mean and the standard deviation σ are in agreement with expectations [76] and less than one strip pitch of the strip for a given layer.

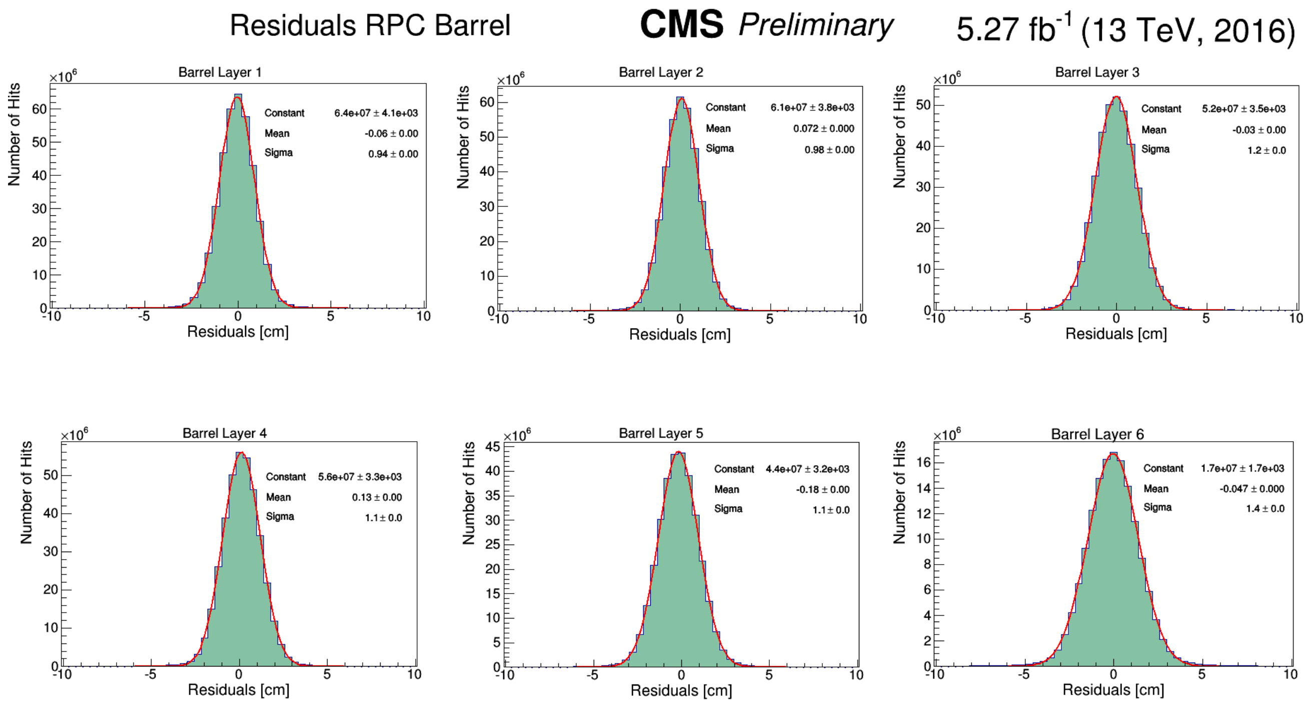

Figure 6.5: RPC barrel residuals for each layer.

6.2.1.3 Time resolution

The good synchronization between sub-detector systems and LHC is very important for the good quality of the recorded physics data. The time measuring unit, used by LHC and CMS is called Bunch Crossing (BX), which corresponds to a 25-ns time window. Figure 6.6 is a typical example of the time distribution of RPC hits from muons. The plot is obtained with 2017 p-p 13 TeV collisions data. The peak in the central bin corresponds to data, which is synchronized with the RPC Level-1 trigger. As seen from the plot, apart from the central BX, RPCs can collect data in one or two neighboring BX windows, i.e. hits which are recorded earlier or later in time with respect to the central BX. Part of the those hits are due to intrinsic noise in the electronics, radiation background or events which happen in a slightly shifted time window than the central event of colliding bunches. Shown results are obtained using the Tracker extrapolation method (see sec. 6.2.1.6)

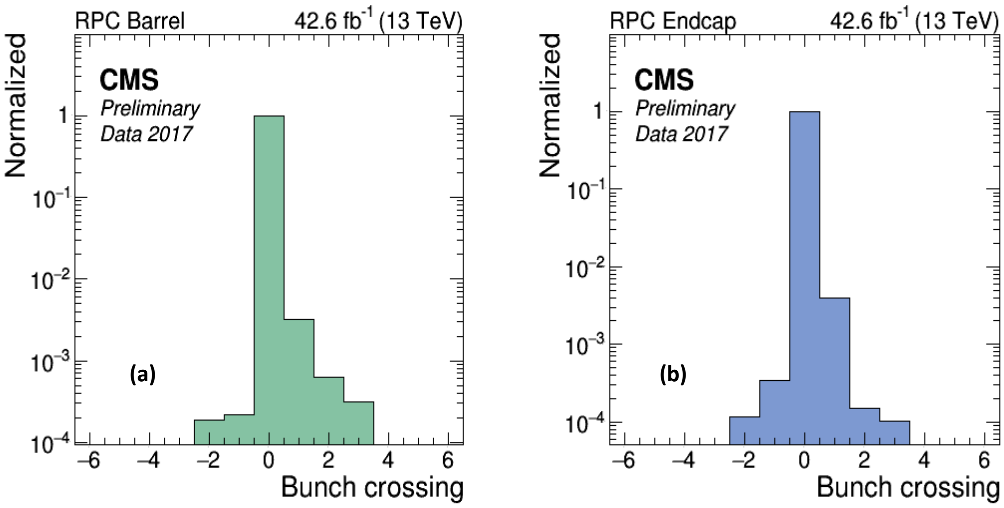

Figure 6.6: RPC bunch crossing distribution for barrel (a) and endcap (b).

The results are in agreement with the ones obtained in 2016 [135] and show stable performance of the RPC system.

6.2.1.4 Efficiency

The RPC efficiency is calculated using the segment extrapolation method (see sec. 6.2.1.2) as the ratio between the number of detected and matched hits and the number of expected hits:

$$RPC_{eff} = \frac{N_{hit}}{N_{ext}}.100\% \tag{6.1}$$

The number of extrapolated segments depends mostly the amount of collected data. Provided the statistics is large enough, the efficiency estimation error is given by:

$$\Delta RPC_{eff} = \sqrt{\frac{RPC_{eff}(1-RPC_{eff})}{N_{ext}}}.100\% \tag{6.2}$$

Analyzing smaller data samples requires a special selection procedure. In order to have enough statistics, only events with at least a minimum of 10^2 extrapolated segments are taken into account for physics analysis.

The RPC system is a very dynamic working system, with constantly changing working conditions during data taking periods. RPC efficiency studies allow monitoring the system performance in a lot of different levels and quickly identifying and fixing any possible operational problems – high voltage (HV) or low voltage (LV) off, gas leaks, gas disconnected chamber, etc.

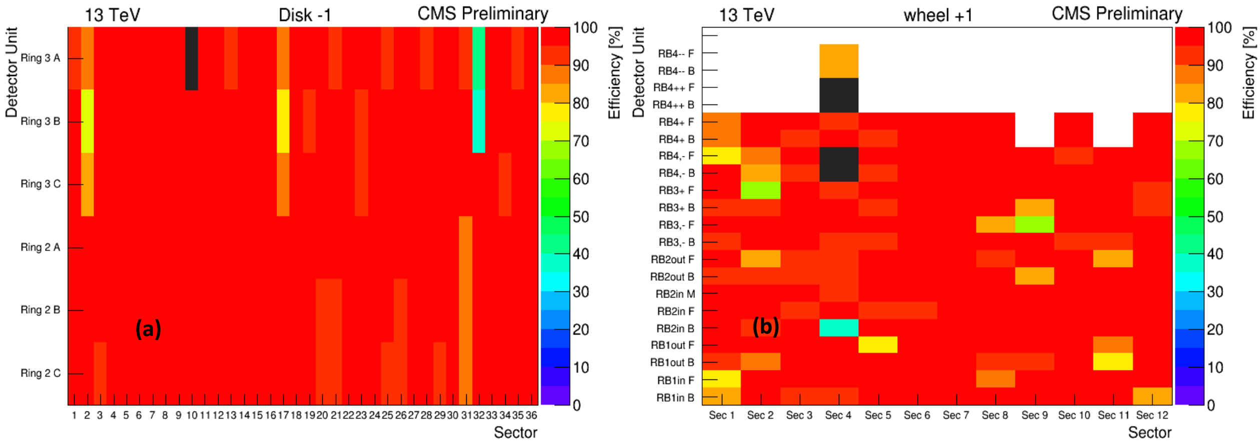

Figure 6.7: Chamber efficiency maps for Disk-1 (a) and for Wheel+1 (b).

Figure 6.7 shows the chamber efficiency map for one wheel and one disk as measured with 2015 data at 13 TeV. Such maps are periodically obtained for each part of the RPC system, as they allow quick and accurate detection of possible operational problems (gas leaks, noisy strips, etc. In figure 6.7(a) the X-axis corresponds to the 36 sectors, and the 6 η partitions are shown on the Y-axis. In figure 6.7(b) the 12 sectors are shown on the X-axis, while the Y-axis corresponds to the 6 RPC layers (RB1in, RB1out, RB2in, RB2out, RB3, RB4) sections. For both plots the black entries correspond to the detector units which are switched off due to known hardware problems. Blue and green colors correspond to the lower efficiency values measured for detector units which have noisy strips that have been masked.

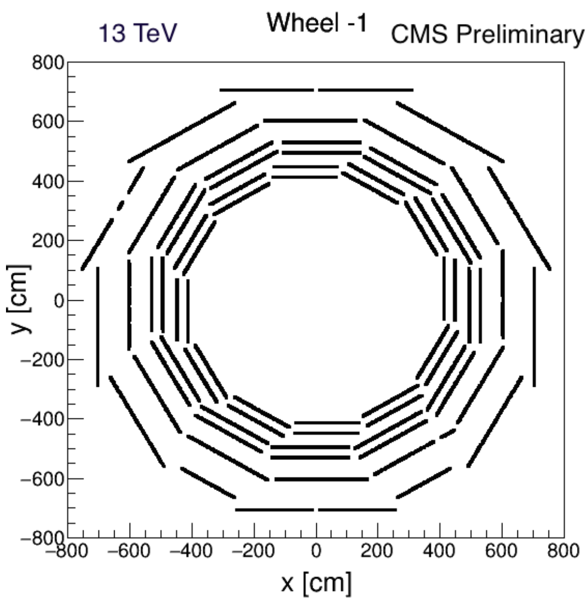

Figure 6.8: Reconstructed muon hits (XY view occupancy) on one of the barrel wheels.

Cross-sectional view of one of the barrel wheels (Wheel-1) is shown in Fig. 6.8. Such plots allow monitoring the exact position and fraction of inactive channels. In the shown example, it is evident that only a few channels in Sector 6 have masked strips (see sec. 4.2.1).

Mapping the efficiency of each sub-detector unit versus the local impact point on the RPC surface is a very fast and easy way to detect possible problematic areas, caused by inactive or noisy strips, as well as possible gas leaks. This analysis is also used for searching for aging effects. In figure 6.9 is shown an example for one of the rolls in the first layer of Barrel Wheel-1 (W-1_RB1in_S08_Backward), which is working with no problems during RUN1 (2010-2012), but a gas leak problem appears in beginning of the 2015 data taking. Despite the encountered problem, the efficiency of the considered RPC is still high enough and it is fully operational. The lower efficiency spots in the plot are due to the dead regions induced by spacers on a 10 x 10 cm^2. The Y-axis is along the strip length. The vertical green line corresponds to a masked readout strip, while the green horizontal spot needs further investigating, since it can be an evidence of possible aging effects.

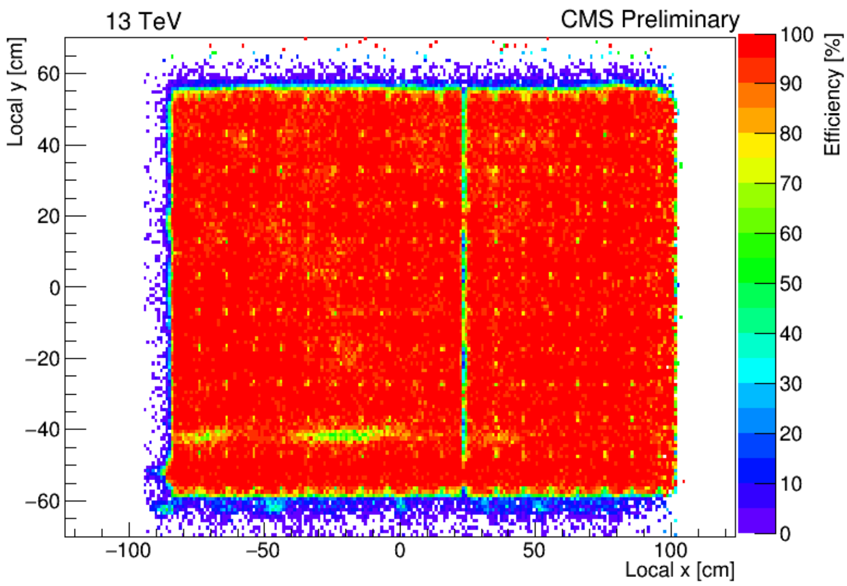

Figure 6.9: Efficiency vs. local impact point on the RPC surface of a roll in the first layer in the Barrel Wheel-1.

6.2.1.5 Performance

Monitoring the overall RPC efficiency as well as the run-by-run efficiency over time is one of the most important RPC system studies. It allows good understanding of how the system operates during different data taking periods, as well as what impact different changes in the operational conditions have over its performance.

As the first data taking after LS1 starts, a problem with the Helium liquefaction system for the CMS solenoid is found – it cannot sustain proper running for extended periods of time [136]. Thus data taking is kept within shorter periods, which leads to lowering the operational time for different systems' scans and maintenance to minimum in order to gain as much physics data as possible. As a result, the RPC system despite performing a good HV scan (see sec. 6.2.2), applies new Working Points only to the newly installed during LS1 RPC chambers in the fourth edncap disks. The other part of the system chambers are kept working with the WP values from 2012.

The overall efficiency distribution for the Disks±4 is shown in figure 6.10 [137]. It is obtained using 2015 p-p collision data at sqrt(s) = 13TeV and B = 3.8T. Few chambers with low efficiency in the distribution correspond to known hardware problems.

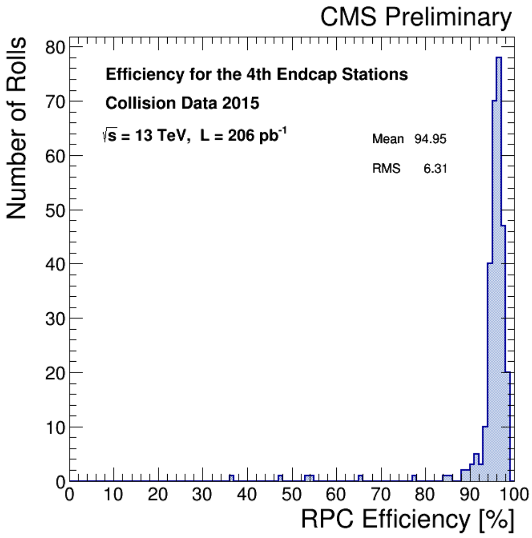

Figure 6.10: Overall efficiency distribution of the fourth endcap stations at 3.8 T.

The efficiency history of the newly installed RE4s during their first year of data taking as part of the RPC system is shown in figure 6.11. The fluctuations in the middle of June, which can be seen in the figure, are due to the performed HV scan, while the ones in the beginning of October are due to the performed threshold scan. The system has higher efficiency (~0.7%) and its performance becomes more stable after deploying the new HV working point (October 2015). The RE4 cluster size history for 2015 is shown in figure 6.12.

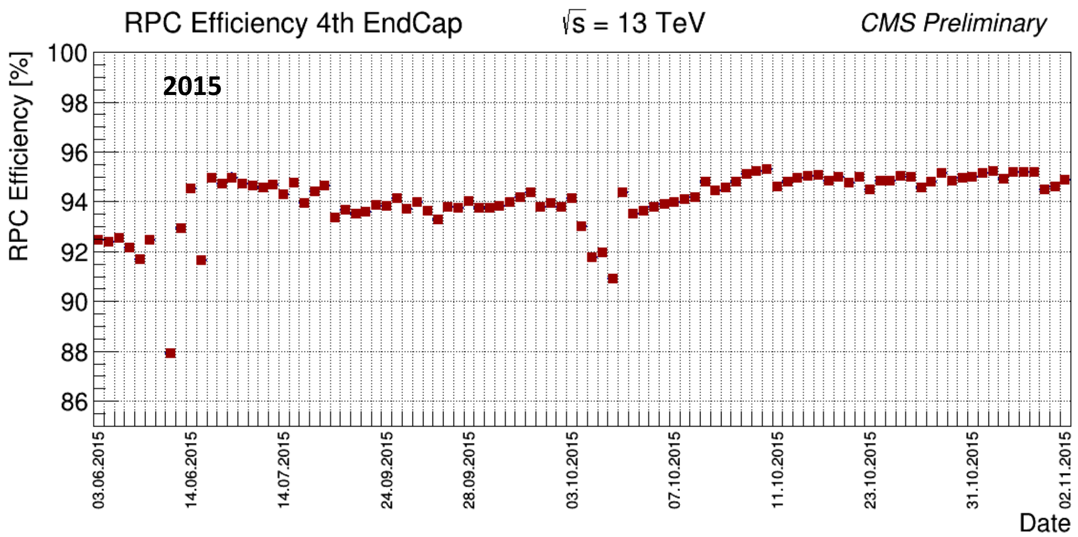

Figure 6.11: History of the RPC Efficiency of the newly installed RPCs on the forward and backward endcaps for the 2015 physics data taking.

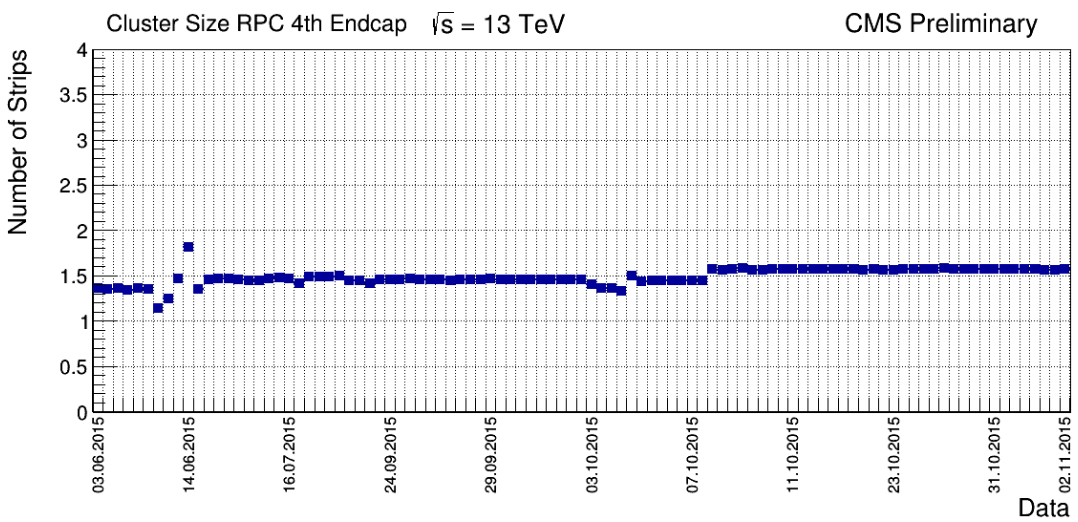

Figure 6.12: History of the cluster size of the newly installed RPCs on the forward and backward endcaps for the 2015 physics data taking.

The RE4 chambers performance during 2015 show good agreement with the expectations and the other parts of the RPC system. During their first year of work as part of CMS, their efficiency average value is ~95% and the cluster size is persistently below 2.

In the process of the system performance analysis during 2016, a dependence of the segment extrapolation method on the instantaneous luminosity is observed, as well as an increase in the number of fake rates. The reason for this is the LHC BX spacing schema changing from 50 ns to 25ns in the end of 2015. This change allows instantaneous luminosity increase, but also leads to higher number of pile up events - ~ 15 in average in RUN1 and between 30 and 45 in average in RUN2. Given the relatively lower instantaneous luminosity and lower number of PU events, such problem is not observed in RUN1 and 2015. The spotted problem is a problem of the algorithm, not of the detectors, i.e. it doesn't have any physical impact on operational level. Yet, in order to fix it, the preliminary selection applied to the data of interest for the system performance analysis is reconsidered. Stronger criteria are applied to standalone muon tracks, which are now required to have transverse momentum $p_T > 7$ GeV and normalized chi2 < 8. The second selection parameter gives the quality of the muon track. The selection of $p_T > 7$ GeV is based on the lowest unprescaled L1 muon trigger, i.e. in order to avoid any trigger bias. The lowest unprescaled trigger for muon in 2016 is with $p_T > 3$ GeV, but since it is changed in 2017, the entire 2016 dataset is reanalyzed using the new selection in order to be able to compare the system performance results. Such selection criteria are not applied in 2015.

As gaseous detectors RPCs are quite sensitive to any changes in the gas mixture ingredients. The standard CMS gas mixture is composed of 95.2% $C_2H_2F_4$ (Freon), 4.5% iC_4H_{10} (Isobutane) and 0.3% SF_6.

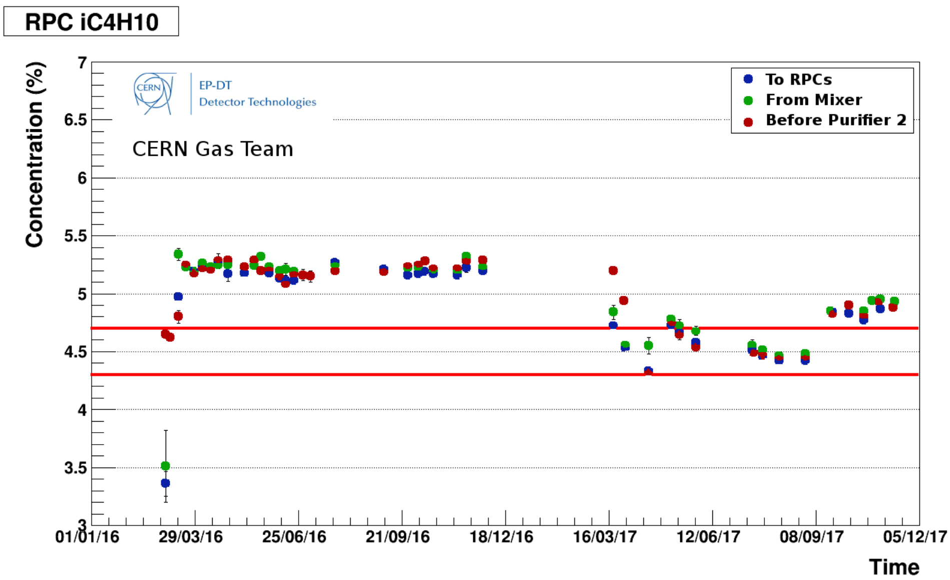

Figure 6.13: Isobutane concentration in the RPC gas working mixture.

During 2017 a mass flow controller problem is discovered, which results in higher Isobutane concentration (5.3%) in the RPC gas working mixture. Figure 6.13 shows the Isobutane concentration history over 2016 and 2017. The two red lines on the plot mark the limits for optimal performance of the CMS RPCs. With green color is given the Isobutane concentration from the mixer. The gas coming from the system before purifier 2 is shown with red color. The blue dots represent the gas going back to RPCs.

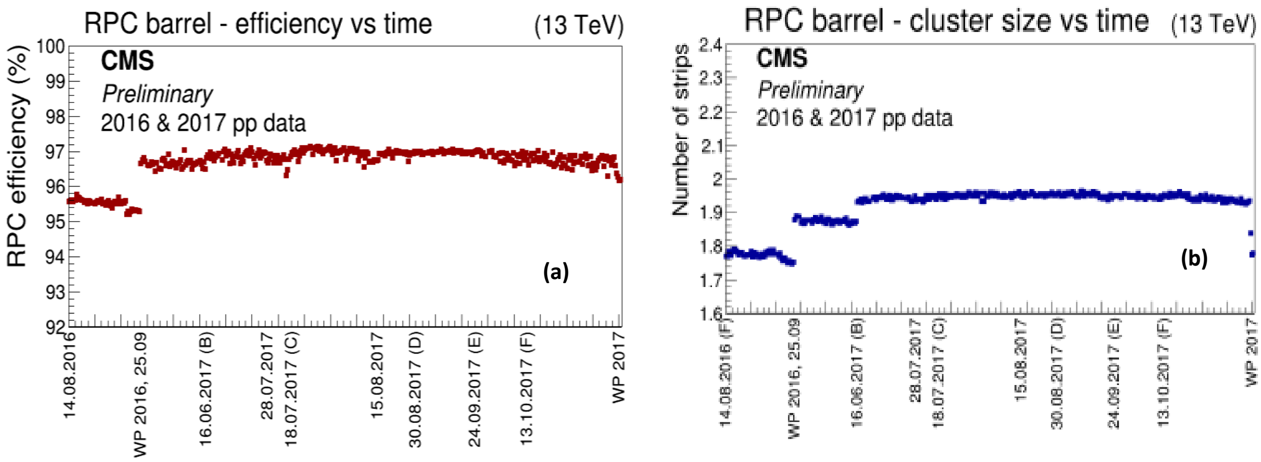

Figure 6.14: The plot represents the history of the RPC efficiency (a) and cluster size (b) for the barrel for 2016 and 2017 p-p collisions at 13 TeV.

Figure 6.14 and figure 6.15 show the history of the RPC efficiency for the barrel and for the endcap respectively for the last two years of RUN2 data taking. These analysis results are very useful when monitoring the RPC system response to different operational and environmental changes.

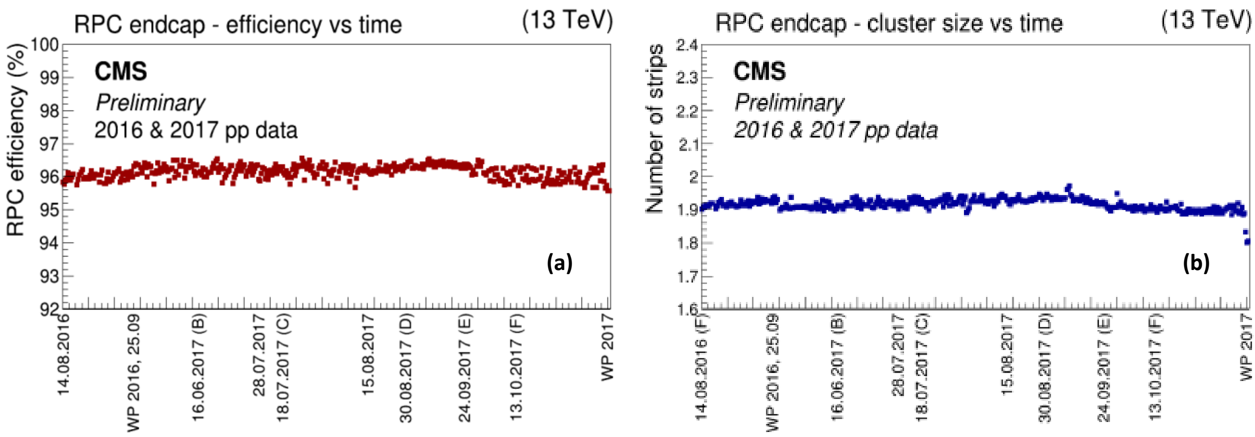

Figure 6.15: The plot represents the history of the RPC efficiency (a) and cluster size (b) for the endcap for 2016 and 2017 p-p collisions at 13 TeV.

The efficiency of the system is lower in 2016, since no change in the HV working points of the detectors is done in order to compensate the wrong gas mixture with higher Isobutane concentration. More details on the HV working points calibration is given in sec. 6.2.2. The new WPs (evaluated with the wrong gas mixture) are deployed in September 2016, leading to increase in the efficiency of ~1%, and sharp increase in the cluster size. Once the gas mixture problem is fixed, the gas concentration is back to standards in 2017, but no change in the WP is done. Although the efficiency of the system remains unchanged (still in the efficiency plateau), a new increase in the cluster size is observed. WPs are changed once more in the end of 2017, this time being evaluated with the correct gas mixture. The applied HV is reduced, which allows to not over-stress the chambers, but also to decrease the average cluster size within the trigger requirements.

As already explained, the new restrictions put on the standalone muon tracks used in the data selection are only algorithm tunes. Further studies on the eventual dependence of the detector performance on the instantaneous luminosity are required. Figure 6.16 represents the RPC barrel efficiency as a function of the instantaneous luminosity measured in proton-proton collision runs in 2016 and 2017 data taking. The instantaneous luminosity is calculated per every analyzed run with the help of the brilcalc tool. In figure 6.17 and figure 6.18 the same comparison is shown, but in respect to the RPC endcap.

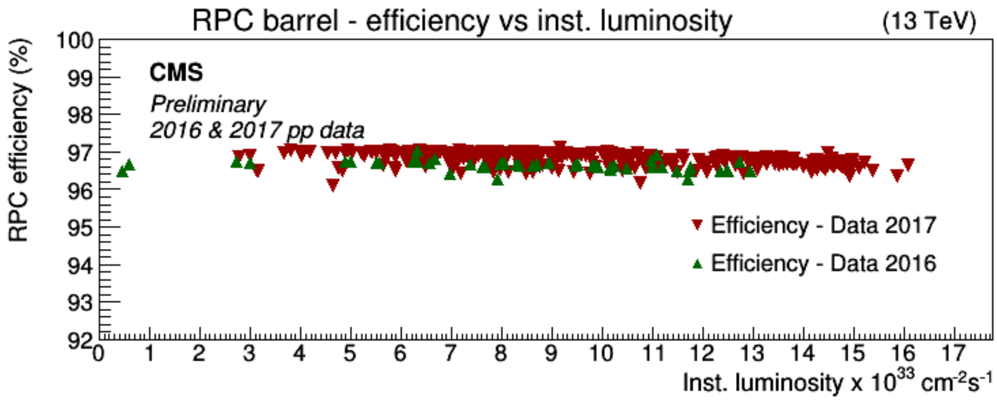

Figure 6.16: RPC barrel efficiency vs. instantaneous luminosity for 2016 and 2017 pp data.

The lower efficiency in 2016 is caused by the higher concentration of Isobutane in the gas working mixture in 2016. Nevertheless the comparison results between the 2016 and 2017 show very stable performance of the RPC system with average efficiency of ~96% and cluster size persistently below 2.

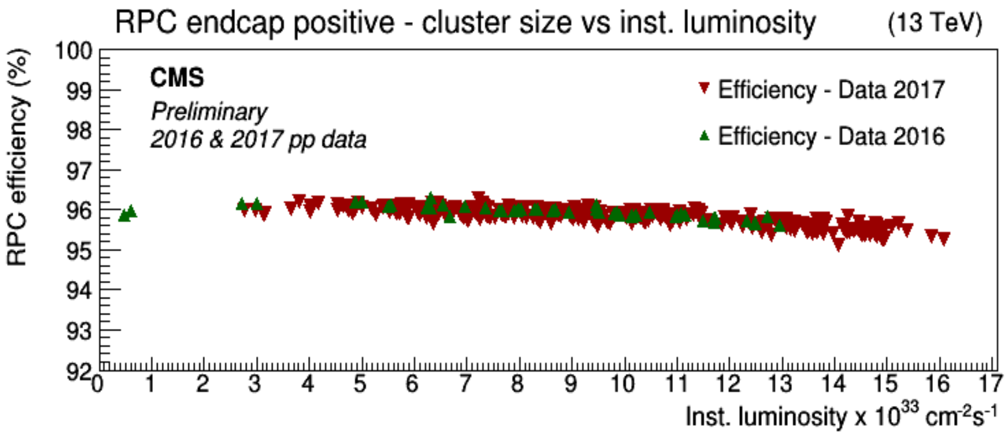

Figure 6.17: RPC positive endcap efficiency vs. instantaneous luminosity for 2016 and 2017 data.

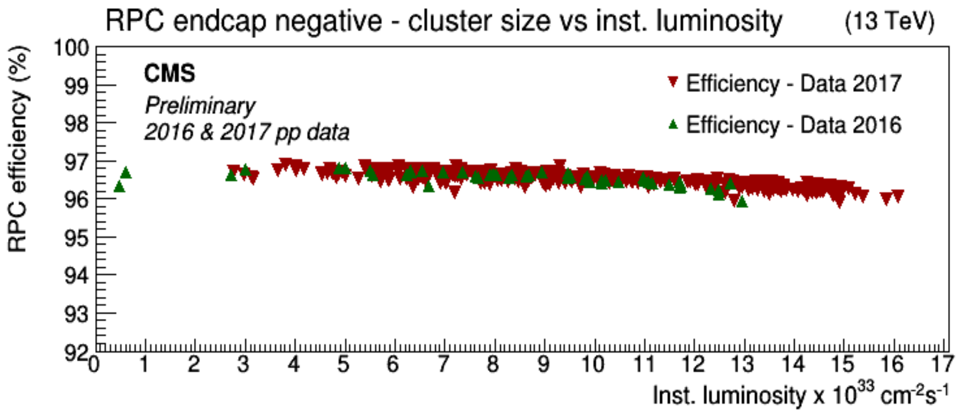

Figure 6.18: RPC negative endcap efficiency vs. instantaneous luminosity for 2016 and 2017 data.

Another way to measure the RPC efficiency is by using the Tracker extrapolation method, which is described briefly here for complicity.

The RPCMuon reconstruction algorithm [138] is included in the standard reconstruction from the RUN2. At standard reconstruction, the algorithm starts from the inner track and finds matched RPC hits (RPCRecHits) along its trajectory. In this step the track extrapolation is done and the results are stored in the muon objects.

The efficiency measurement using the track extrapolation in the RPCMuons, requires TrackerMuon [139] identification on the muons. It is done by extrapolating inner tracks to muon systems in order to find matching DT/CSC segments. The TrackerMuon algorithm is used for reconstructing probe muons, requiring at least one segment to be matched in local x position within 3 cm and pull ≤ 3. Probe muons are also required to have at least 10 GeV in transverse momentum. Both the TrackerMuon and the RPCMuon reconstruction are designed to run independently and to be complementary algorithms to each other. Efficiency is obtained using the tag-and-probe method [140] with single muon triggered dataset.

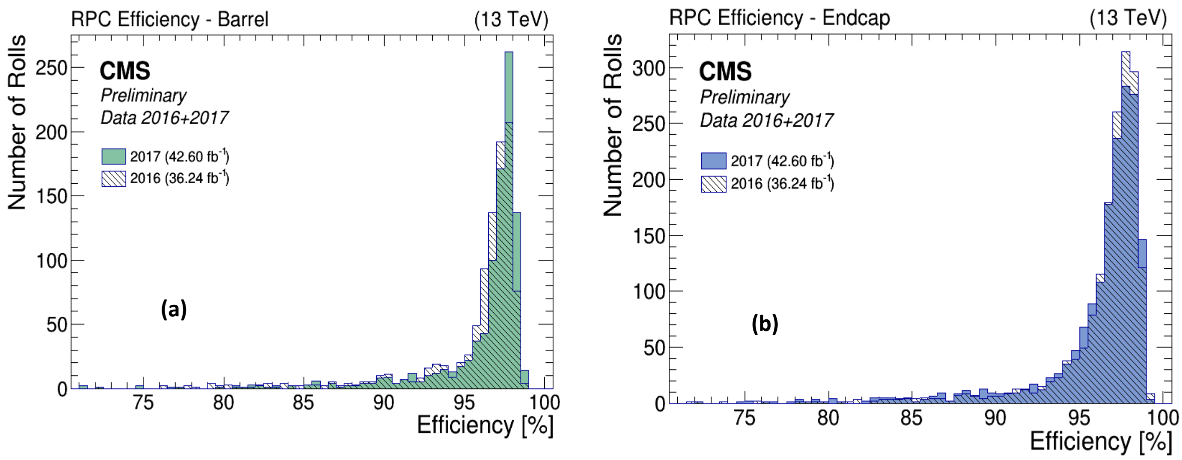

Figure 6.19: Comparison of RPC overall efficiency distributions in 2017 to 2016 in barrel chambers (a) and endcap chambers (b).

Comparison of the overall RPC efficiency distributions for 2016 and 2017 for the barrel (a) and the endcap (b), obtained with the tracker extrapolation method, can be seen in figure 6.19. The underflow entries in the plots are from rolls with efficiency lower than 70%, caused by known hardware problems – chambers with gas leak problems in the barrel and low voltage problems in the endcap. These rolls are 1.8% of all barrel rolls and 1.2% of all endcap rolls. Average RPC efficiency during 2016 and 2017 is ~ 96% for the entire system.

6.2.1.6 Conclusions

All results on the RPC system performance shown in the chapter so far are obtained after three years of constant work of the RPC performance analysis team, with the analysis directly done or supervised by the doctorate candidate. These include all the data analysis steps, space and time resolution studies, as well as efficiency studies.

Results from analysis done by the doctorate candidate are also used for further precision studies on the RPC detectors, such as Working Point calibration, explained in the next subchapter.

6.2.2 Working Point calibration

The efficiency of the RPC detectors depends strongly on the applied high voltage (HV) [95]. In order to optimize the detectors performance, special high voltage (HV) calibrations (scans) are done at least once per year during data taking. The need of such scans comes from the constant increase of instantaneous luminosity and the increase of the energy of the colliding particles. The main goal of the HV scan is to determine the optimal operating voltage for each chamber [85, 141]. HV scan results are also used for studying the system operation parameters over the years and detecting possible aging effects on the chambers.

Collision data is recorded at several effective, equidistant voltages in the working range of 8600–9800 V, during a special sequence of runs. The collected data is used to determine the nominal operational high voltage for each chamber, called Working Point (WP).

In order to take into account the dependence of the RPC avalanche production on the environmental pressure *p*, the temperature T and the applied HV, a correction defining the effective HV (HV_{eff}) for detectors in the RPC system is applied using the equation [82]:

$$HV_{eff}(p,T) = HV_{app}\frac{p_0}{p}\frac{T}{T_0} \qquad (6.3),$$

where HV_{eff} is effective high voltage, HV_{app} is applied high voltage, and the reference temperature and pressure are T_0 = 293 K and p_0 = 965 mbar (reference pressure in the cavern).

The result from the HV scan shows the obtained efficiency as a function of the effective high voltage, as shown in figure 6.20. The efficiency along the HV scan can be described by the sigmoid function given by equation:

$$\in = \frac{\in_{max}}{1 + e^{-\lambda\left(HV_{eff} - HV_{50\%}\right)}} \quad (6.4),$$

where $\in_{max}$ is the maximum efficiency, λ is the slope defining factor ($slope = \left(\lambda \in_{max}\right)/4$), and $HV_{50\%}$ is the high voltage at which a chamber reaches 50% of the plateau efficiency.

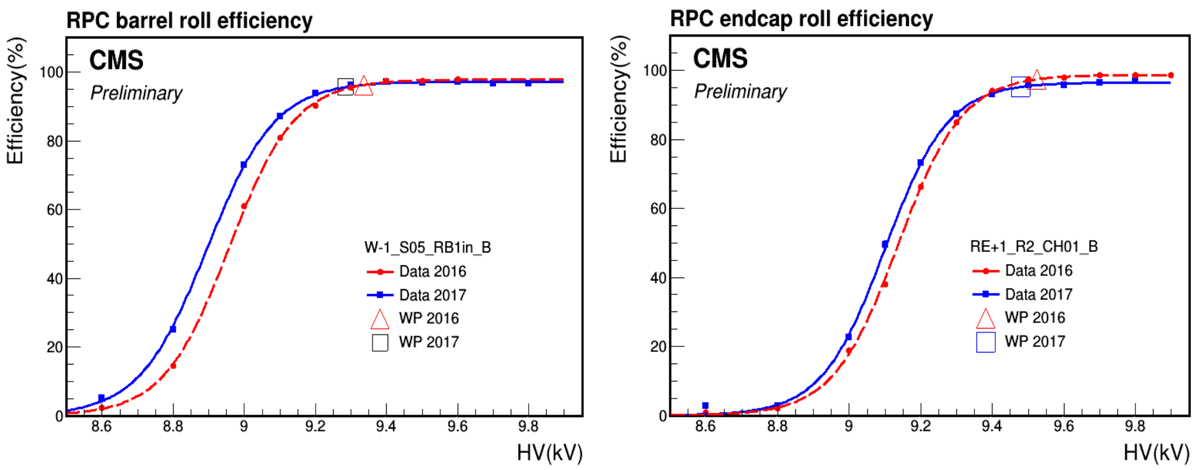

Figure 6.20: RPC HV scans in 2016 and 2017 showing the evaluated WPs.

The shifts of the 2016 (red) curves to higher HV values are caused by the higher Isobutane concentration in 2016. The Knee voltage is defined as the high voltage at which the efficiency is 95% of the maximum efficiency. When deploying the WP, several things are taken into consideration – the barrel and the endcaps have different geometrical designs for the RPC detectors, the cluster size is required to stay within accepted limits of ≤ 2 (cluster size increase with applying higher voltage), and the number of detector layers in the barrel is higher than the one in the endcap. After a detailed study, considering all these requirements, the optimal Working Point is defined as WP = Knee + (100/120) V for every chamber from the barrel/endcap [136]. Because of this, both working points (evaluated at 2016 and 2017) are in the plateau of the curves. The difference in the WP definition allows the endcap, working at higher HV to provide similar global efficiency as the barrel.

During 2017 two HV scans are taken – the first one in May at relatively low instantaneous luminosity of 0.15-0.17 x 10^{34} $cm^{-2}s^{-1}$, while the second one in September at very high instantaneous luminosity of 1.2-1.3 x 10^{34} $cm^{-2}s^{-1}$. This is done to optimize the HV working conditions of the RPC detectors in respect to the increasing luminosity, as well as study the effect of wrong gas mixture operation. Results shown in figure 6.21 and figure 6.22 are obtained with data from the first HV scan, performed in May.

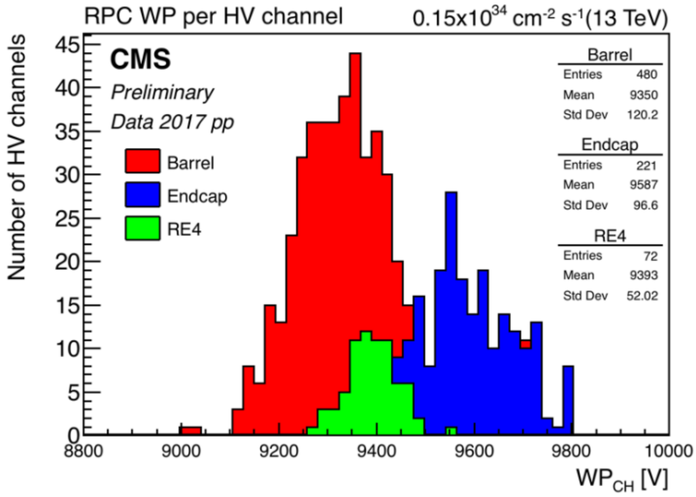

Figure 6.21: Distribution of the new HV working points per HV channel

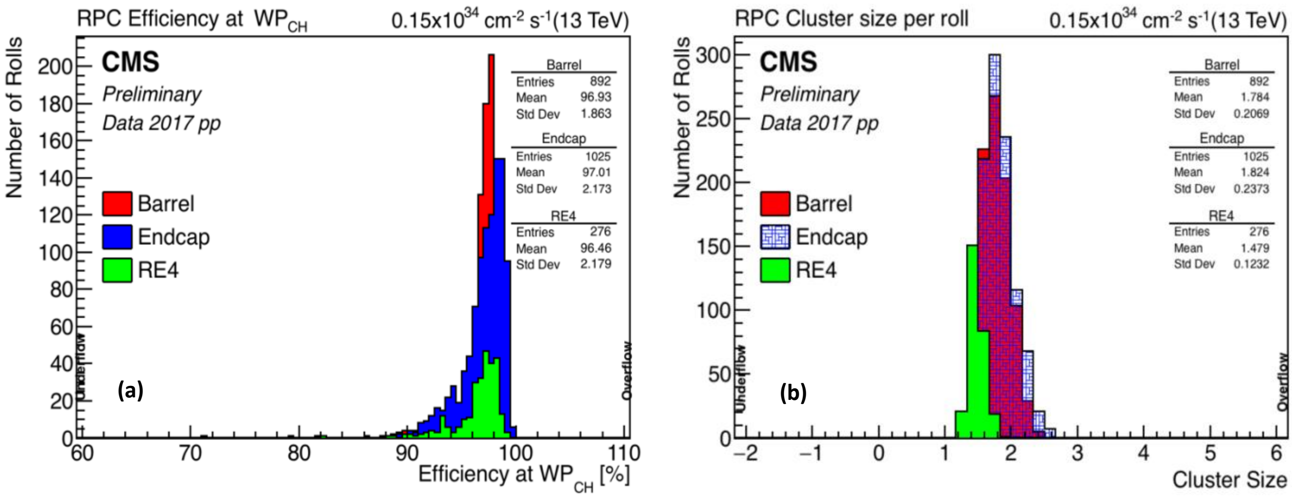

Figure 6.22: RPC efficiency (a) and cluster size (b) at WP.

The new WPs per HV channel are shown in figure 6.21, while figure 6.22 shows the efficiency and the cluster size at WP, as derived from the 2017 HV scan analysis. The two innermost RPC rolls for RE4 are excluded from the analysis due to the lack of muon segment statistics. This explains the lower average cluster size for RE4 with respect the rest of the endcap.

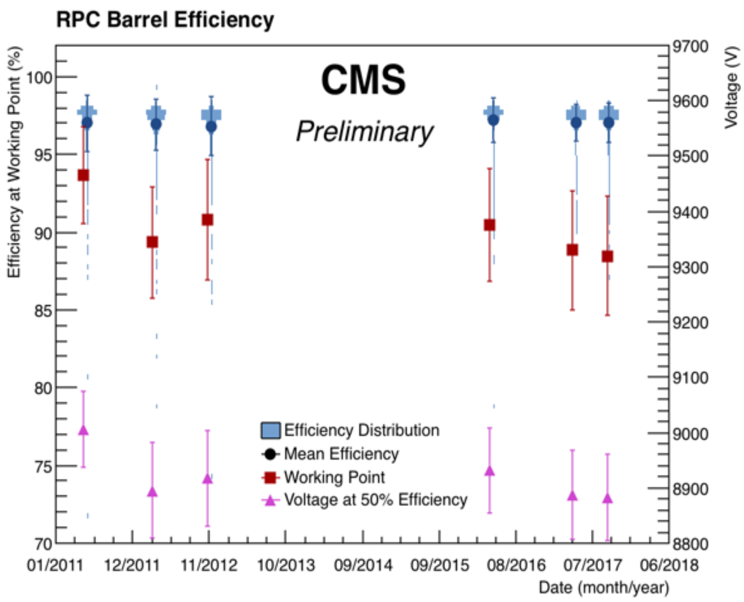

Figure 6.23: CMS RPC HV scans per year for the barrel showing the evolution of the WP, the efficiency at WP and the $HV_{50\%}$.

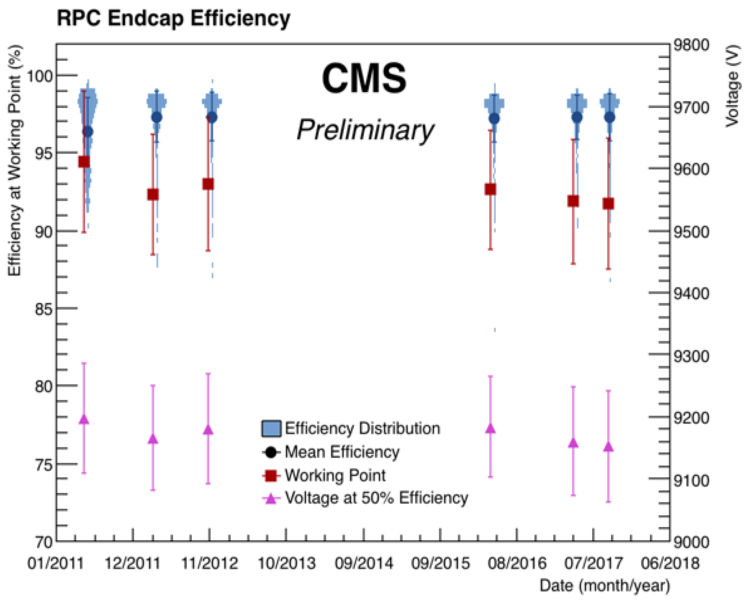

Figure 6.24: CMS RPC HV scans per year for the endcap showing the evolution of the WP, the efficiency at WP and the $HV_{50\%}$.

The evolution during all periods of data taking of the WP, the efficiency at WP and the $HV_{50\%}$ for the barrel and the endcap are shown in figure 6.23 and figure 6.24. The efficiency at WP is presented with a light blue color, while the mean efficiency at WP for each of the HV scans is shown with a blue full circle. By red full squares the mean of the WP distribution for each HV scan is represented along with their Standard deviations. The mean of the high voltage at 50% efficiency distribution for each HV scan with their standard deviations is represented in magenta full triangles. The higher isobutene concentration in the CMS RPC standard gas mixture during 2016 is the reason for the shift of around 40 V to lower values, which is observed in 2017 with respect to 2016. However the lowering of the HV WP does not affect the chamber efficiency since chambers are already working at efficiency plateau.

6.2.3 Hit rate and Background

The overall performance of the CMS RPC system depends also on the background radiation levels as it gives the main contribution in the measured RPC rate. Background radiation is induced mostly by the collisions – particles leak through forward shielding, scatter around in the cavern and reflect back to the muon system [142]. The main background sources are low energy neutrons, photons produced in de-excitation of nuclei and punch-through hadrons. All these can have an impact on trigger performance and pattern recognition of muon tracks. Excessive radiation levels can also cause premature ageing of the detectors.

The background in the cavern is studied in terms of RPC hit rate and HV currents as a function of the instantaneous luminosity. Rates and currents are measured during the proton-proton collision data taking and including the instantaneous luminosity are averaged per run. The hit rates are measured directly from the link-board counts, while the obtained results for the RPC currents are based on the analysis of a set of specially selected runs, which have identical running parameters like LHC energy, LHC bunch schema, number of colliding bunches, β^*, beam crossing angle and declared stable beam.

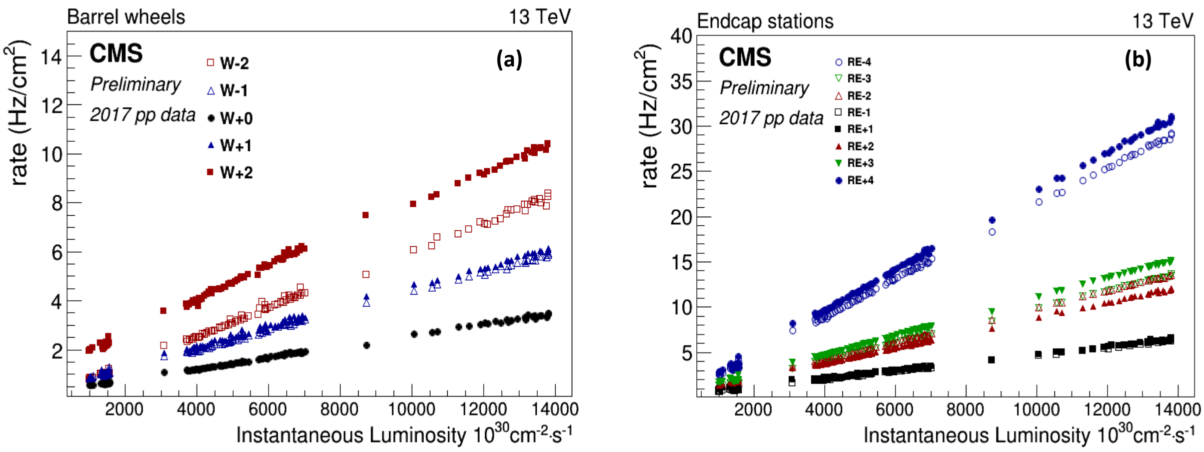

Figure 6.25: RPC hit rate vs. instantaneous luminosity distributions for barrel wheels (a) and endcap stations (b).

Figure 6.25 shows RPC barrel and endcap hit rate vs instantaneous luminosity measured with 2017 data. Highest hit rates are measured in the fourth positive and negative endcap stations RE4, which are furthest from the interaction point and are mostly affected by the background in the cavern.

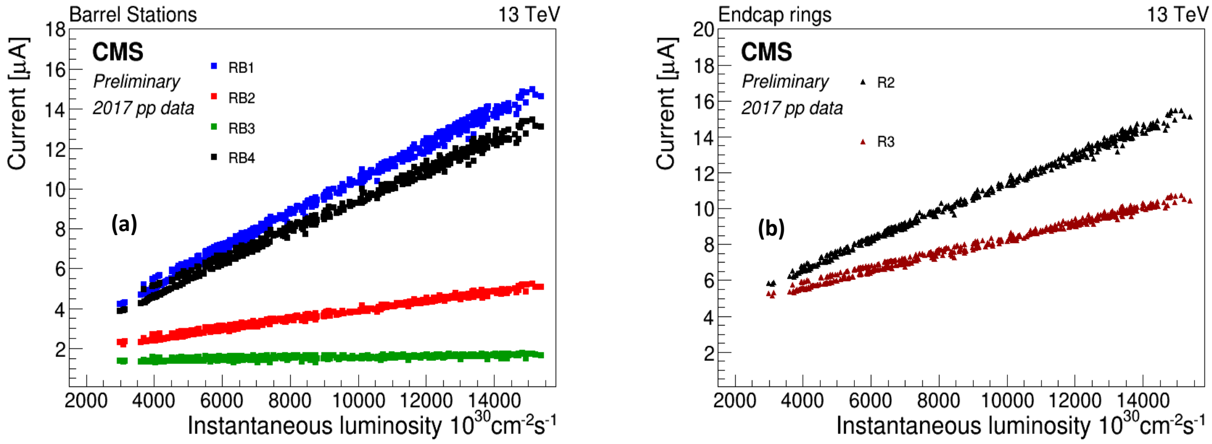

Figure 6.26: RPC currents vs. instantaneous luminosity distributions for barrel (a) and endcap (b).

RPC barrel and endcap currents vs. instantaneous luminosity distributions for 2017 are shown in figure 6.26(a) and figure 6.26(b). The barrel distributions are from the 4 barrel stations, while the results for the endcap show the 2 rings where there are RPCs installed. The highest current is measured in the innermost barrel station RB1, caused mainly by primary interactions passing particles, and also in the outermost barrel station RB4, caused mainly by the background in the cavern. In the endcap the highest current are measured in Ring 2, which is closer to the beam pipe and the interaction point.

6.3 Conclusions

This chapter gives detailed insight on the performance analysis of the RPC system during RUN2 data taking. A total amount of more than 249 TB of physics data is collected, preselected and analyzed by the doctorate candidate or under her supervision over the period of three years during 2015 – 2017. The newly built RE4 RPCs are successfully integrated within the RPC system and show good and stable performance. Detailed analysis on the entire RPC system as well as each individual chamber are performed and results on the efficiency and cluster size as function of the time and the instantaneous luminosity are obtained. The impact of the different gas mixture on the system performance is studied.

Obtained results show smooth and stable performance of the RPC system with no significant issues detected in respect to maintenance, operation and data acquisition.

After 8 years from the end of the RPC construction, three years from the end of the LS1 muon upgrade and three years of running at increasing instantaneous luminosity, the system is running and collecting successfully good quality physics data with average efficiency of ~96%, average cluster size persistently below 2 and average rate of ~10 Hz/cm^2.

Results from the shown analysis over RUN2 data are presented by the doctorate candidate in four conference talks, one poster and two scientific publications.

The doctorate candidate is part of the RPC Offline Analysis team during RUN2.

The tasks with the significant contribution of the doctorate candidate during 2015 – 2017 are:

1. **Evaluations of collected data –** specially designed selection criteria are applied and pre-selection is obtained for every run taken by the CMS experiment – physics as well as special calibration runs taken for different scans.
2. **Offline Analysis running** – all consecutive steps of the analysis algorithm are run using the software packages CMSSW, ROOT and CRAB and results are obtained with the WLCG network.
3. **System performance evaluation** – results from the analysis steps are gathered and evaluated and the results on the main system performance parameters such as efficiency, cluster size, residuals, bunch-crossing, etc. are obtained. Their behavior in time and in respect to the increasing instantaneous luminosity is also examined.
4. **Evaluation of the LHC conditions** – special criteria are applied on the LHC energy, LHC bunch schema, number of colliding bunches, β^*, beam crossing angle and stability of the beams in order to preselect identical conditions for RPC Background studies.
5. **Online & Offline system monitoring and data certification** – direct participation in the data certification process as a Data Manager on shift, as well as Detector O&M; direct participation in the system online monitoring and maintenance as Detector-On-Call (DOC) shifter.
6. **New colleagues' supervision** – introducing new colleagues to the performed analysis tasks, as well as proper interpretation and evaluation of obtained results.

Work done by the doctorate candidate for the RPC system operation during RUN2 is highly appraised by the RPC community and the doctorate candidate is chosen as one of the Detector O&M supervisors during 2018-2019.

7. Scientific contribution

7.1. Obtained results and personal involvement

Subject of this scientific thesis is the work done by the doctorate candidate for the CMS RPC system during the last five years. It can be considered in two main aspects - LS1 muon upgrade and RUN2 data taking.

The main obtained results from all performed studies are:

1. **During the LS1 Upgrade (2013 - 2014)** –
   - RPC detecting elements (gaps) for the LS1 Muon system upgrade RPC chambers are evaluated using QC2 protocols (visual tests, leak and spacer tests and dark current test).
   - A total of 200 new RPC detectors for the new RE4 system are assembled during QC3 stage of production.
   - Working parameters (efficiency, cluster size, noise rate, and optimal working point) for all RE4 chambers are evaluated at specially designed telescopes using cosmic rays.
   - A new robust and **stable** RE4 system is built, installed and commissioned successfully on the fourth disks of the CMS muon endcaps.

2. **During RUN2 data taking (2015 – 2017)** –
   - A total amount of more than 249 TB good experimental data is certified, pre-selected and analyzed on a run basis.
   - Results on the distributions of the main RPC system performance parameters such as efficiency, cluster size, residuals and bunch crossing are obtained.
   - Efficiency and cluster size behavior as a function of time is evaluated and also their behavior as a function of increasing instantaneous luminosity is examined.
   - Special pre-selection on LHC operational parameters (the LHC energy, LHC bunch schema, number of colliding bunches, β^*, beam crossing angle, stability of the beams) is done to ensure identical conditions for RPC background studies.
   - The RE4 system is successfully integrated in the CMS experiment, contributing to the good and stable performance of the entire RPC system.

The tasks with the significant contribution of the doctorate candidate during 2013 – 2017 are:

1. **During LS1 Upgrade (2013 – 2014**) –
    - Evaluation of the detecting elements (RPC gaps) in QC2 stage of production – visual test, leak and spacer tests.
    - Dark current test.
    - Chamber assembling during QC3 stage of production
    - Test of the newly built chambers at the cosmic rays telescope.

2. **During RUN2 data taking (2015 - 2017)** –
    - Evaluations of collected data – specially designed selection criteria are applied and pre-selection is obtained for every run taken by the CMS experiment – physics as well as special calibration runs taken for different scans.
    - Offline Analysis running – all consecutive steps of the analysis algorithm are run using the software packages CMSSW, ROOT and CRAB and results are obtained with the WLCG network.
    - System performance evaluation – results from the analysis steps are gathered and evaluated and the results on the main system performance parameters such as efficiency, cluster size, residuals, bunch-crossing, etc. are obtained. Their behavior in time and in respect to the increasing instantaneous luminosity is also examined.
    - Evaluation of the LHC conditions – special criteria are applied on the LHC energy, LHC bunch schema, number of colliding bunches, β^*, beam crossing angle and stability of the beams in order to preselect identical conditions for RPC Background studies.
    - Online & Offline system monitoring and data certification – direct participation in the data certification process as a Data Manager on shift, as well as Detector O&M; direct participation in the system online monitoring and maintenance as Detector-On-Call (DOC) shifter.
    - New colleagues' supervision – introducing new colleagues to the performed analysis tasks, as well as proper interpretation and evaluation of obtained results.

Following the good work over the years, the doctorate candidate is chosen as one of the RPC Detector O&M supervisors for the period of 2018-2019.

7.2. Scientific publications connected to the thesis

1. M. Shopova, R. Hadjiiska et al., **"Study of the performance of RPC system installed at the CMS experiment" –** C. R. Acad. Bulg. Sci. Vol 70 (2017), No1, pp.41-44.
2. M. Shopova, M.A. Shah, M. I. Pedraza-Morales, …, et al., **"First results of CMS RPC performance at 13 TeV"**, JINST 11 (2016) no.09, C12003, doi:10.1088/1748-0221/11/12/C12003
3. M. Shopova, M.S. Kim, …, et al., **"Resistive plate chambers for the LS1 muon upgrade in CMS experiment at LHC",** Bulgarian Chemical Communications, Volume 47, Special Issue B (pp. 185–191) 2015
4. S. Colafranceschi, …, M. Vutova,…, et al., **"Resistive plate chambers for 2013-2014 muon upgrade in CMS at LHC",** 2014 JINST 9 C10033, DOI: 10.1088/1748-0221/9/10/C10033
5. A. Cimmino, …, M.Vutova et al., **CMS RPC commissioning of the existing detector during the long shutdown,** 2014 JINST 9 C10043, doi:10.1088/1748-0221/9/10/C10043
6. S Costantini, …., M.Shopova, …., et al., **Uniformity and stability of the CMS RPC detector at the LHC,** 2013 JINST 8 P03017, DOI: 10.1088/1748-0221/8/03/P03017

7.3. Conference presentations connected to the thesis

1. M. Shopova on behalf of the CMS collaboration, **Performance of Resistive Plate Chambers installed during the first long shutdown of the CMS experiment**, XIX Winter seminar "Interdisciplinary Physics", December 2016, Koprivshtica, Bulgaria – talk.

2. M. Shopova on behalf of the CMS collaboration, **Bulgaria in the CMS muon system**, SCIENCE FORUM "YOUNG SCIENTISTS 2016", November 2016, Pamporovo, Bulgaria – talk.

3. M. Shopova on behalf of the CMS collaboration**, Bulgaria in the CMS experiment**, V National Student Conference on Physics, 16-18 November 2016, Plovdiv, Bulgaria – talk.

4. M. Shopova on behalf of the CMS muon group, **Study of the performance of RPC system installed at the CMS experiment**, Third National Congress on Physical Sciences, 29 Sep-2 Oct 2016, Sofia, Bulgaria – talk.

5. M. Shopova on behalf of the CMS collaboration, **Performance of Resistive Plate Chambers installed during the first long shutdown of the CMS experiment**, RPC2016 – The XIII Workshop on Resistive Plate Chambers and related detectors, 22-26 February 2016, Ghent, Belgium – poster.

6. M. Shopova on behalf of the CMS collaboration, **RPCs for the CMS experiment LS1 muon upgrade**, CMS Physics and Upgrade week, 7-11 September 2015, Ischia(Napoli), Italy – poster **– BEST POSTER AWARD.**

7. M. Shopova on behalf of the CMS collaboration, **Assembling and testing of Resistive Plate Chambers for the LS1 muon upgrade of the CMS experiment**, Bulgarian National Conference in Physics, 10-12 Oct 2014, Plovdiv, Bulgaria – talk**.**

8. M. Shopova on behalf of the CMS collaboration, **Resistive Plate Chambers for the LS1 muon upgrade in CMS Experiment**, Trends in Particle Physics, Primorsko 2014, Bulgaria – talk.

7.4. Scientific publications as part of the CMS Muon RPC collaboration

The doctorate candidate is a **member of the CMS Muon RPC collaboration since 2010.**

1. M. I. Pedraza-Morales, …, M. Shopova et al, **Offline Data Quality Monitoring for the RPC of the CMS Detector**, J. Phys.: Conf. Ser. 761 (2016) 012054
2. J. R. Pilot, …, M. Shopova et al., **Future of the CMS Muon System Upgrades and Aging**, PoS: ICHEP2016 (2016) , pp. 281
3. CMS Collaboration, **R and D towards future CMS RPC upgrades**, *JINST* 11 (2016) C09017
4. M. S. Kim,…, M. Vutova, et al., **Web-based monitoring tools for Resistive Plate Chambers in the CMS experiment at CERN**, *JINST* 9 (2014) C10031
5. G. Pugliese, …, M. Vutova et al., **CMS RPC muon detector performance with 2010-2012 LHC data,** 2014 JINST 9 C12016, doi:10.1088/1748-0221/9/12/C12016

6. M. Tytgat, …., M. Shopova et al., **The Upgrade of the CMS RPC System during the First LHC Long Shutdown,** PoS RPC2012 (2012) 063 JINST 8 (2013) T02002, DOI: 10.1088/1748-0221/8/02/T02002
7. P. Paolucci, M. Vutova et al., **CMS Resistive Plate Chamber overview, from the present system to the upgrade phase I,** 2013 JINST 8 P04005 doi:10.1088/1748-0221/8/04/P04005
8. CMS Collaboration, **The performance of the CMS muon detector in proton-proton collisions at √ s = 7 TeV at the LHC**, *JINST* 8 (2013) P11002
9. M. S. Kim, …, M. Vutova et al., **The CMS RPC system - detector performance and upgrade**, PoS: EPS-HEP2013 (2013) , pp. 123
10. J. Eysermans, …, M. Shopova et al., **Operation and performance of the CMS Resistive Plate Chambers during LHC run II**, 2017 J. Phys.: Conf. Ser. **912** 012015, doi: 10.1088/1742-6596/912/1/012015
11. A. Madorsky,…., M. Shopova et al., **Electronics for CMS Endcap Muon Level-1 Trigger System Phase-1 and HL LHC Upgrades Summary**, 2017 JINST **12** C07010, doi: 10.1088/1748-0221/12/07/C07010
12. A. Triossi, …, M. Shopova et al., **The CMS Barrel Muon Trigger Upgrade**, JINST 12 (2017) C01095
13. A. L. Cabrera, …, M. Shopova et al., **CMS Resistive Plate Chambers performance at √s =13 TeV**, 2016 IEEE NSS/MIC/RTSD, pp. 1-3., 2016, doi: 10.1109/NSSMIC.2016.8069690
14. G. Gonzalez, …, M. Shopova et al., **Detector control system and efficiency performance for CMS RPC at GIF++,** 2016 JINST 11(10):C10013-C10013, DOI: 10.1088/1748-0221/11/10/C10013
15. CMS Collaboration, **Preliminary results of Resistive Plate Chambers operated with eco-friendly gas mixtures for application in the CMS experiment,** 2016 JINST 11 C09018, doi: 10.1088/1748-0221/11/09/C09018
16. K. S. Park, …, M. Shopova et al., **Charge distribution dependency on gap thickness of CMS endcap RPC**, 2016 JINST 11 C11034, doi: 10.1088/1748-0221/11/11/C11034
17. D. S. Rabady, …, M. Shopova, et al., **Upgrade of the CMS muon trigger system in the barrel region**, *Nucl. Instrum. Methods Phys. Res., A* 845 (2016) 616-620
18. R. Kumar, …, M. Sopova et al., **Assembly and Characterization of Resistive Plate Chambers in India for the CMS Detector**, *Springer Proc. Phys.* 174 (2016) 553-557
19. S. K. Park, …, M. Vutova et al, **RPC Gap Production and Performance for CMS RE4 Upgrade**, 2014 JINST 9 C11009, doi: 10.1088/1748-0221/9/11/C11009

20. K. S. Lee, …, M. Vutova et al, **Rate-capability study for a four-gap phenolic RPC with a Cs-137 source**, *JINST* 9 (2014) C08001
21. J. Seo, …, M. Vutova et al., **Optimization of the gas system in the CMS RPC Detector at the LHC**, 2013 IEEE NSS/MIC doi: 10.1109/NSSMIC.2013.6829814
22. S. K. Park, …, M. Vutova et al., **Production and Performance of RE4 Resistive Plate Chambers for CMS experiments upgrade**, 2013 IEEE NSS/MIC, DOI: 10.1109/NSSMIC.2013.6829571
23. M. S. Kim, …, M. Vutova et al., **Role of the RPC Detector in the CMS Muon System for tracking and trigger**, 2013 IEEE NSS/MIC, DOI: 10.1109/NSSMIC.2013.6829812
24. J. Duarte Campderros, …, M. Vutova et al., **Alignment of the CMS muon detectors**, PoS: EPS-HEP2013 (2013) , pp. 104
25. D. E. Acosta, …, M. Vutova et al, **The CMS Modular Track Finder Boards, MTF6 and MTF7**, *JINST* 8 (2013) C12034
26. M. Abbrescia, …, M. Vutova et al., **Operation, performance and upgrade of the CMS RPC muon system at LHC**, Nucl. Instrum. Methods Phys. Res., A 732 (2013) 195-198, doi: 10.1016/j.nima.2013.05.150
27. H. Seo, …, M. Vutova et al., **RPC hit contribution to CMS muon Reconstruction at LHC**, Nucl. Instrum. Methods Phys. Res., A 718 (2013) 437-439, doi: 10.1016/j.nima.2012.08.056
28. F. Thyssen, …, M. Vutova et al., **Front-End Control and Monitoring System for the Resistive Plate Chambers at the CMS Experiment**, 2011 IEEE NSS, pp. 1119-1123, doi: 10.1109/NSSMIC.2011.6154585
29. F. Thyssen, …, M. Vutova et al., **Performance of the Resistive Plate Chambers in the CMS experiment**, 2012 JINST 7 C01104, doi: 10.1088/1748-0221/7/01/C01104
30. S. K. Park, …, M. Vutova et al., **CMS muon detector and trigger performances**, *Nucl. Phys. B, Proc. Suppl.* 215 (2011) 356-358

7.5. Scientific publications as part of the CMS collaboration

The doctorate candidate is a **member of the CMS collaboration since 2010** and by the time of finishing her PhD thesis the doctorate candidate is in the list of the CMS authors in **581 publications**. A link to the publications is given here:

- http://inspirehep.net/search?ln=en&ln=en&p=find+a+mariana+vutova+AND+collection%3Apublished+AND+cn+CMS&of=hb&action_search=Search&sf=&so=d&rm=&rg=25&sc=0 – 523

- http://inspirehep.net/search?ln=en&ln=en&p=find+a+mariana+shopova+AND+collection%3Apublished+AND+cn+CMS&of=hb&action_search=Search&sf=&so=d&rm=&rg=25&sc=0 – 58

Bibliography

[1] P. Langacker, Introduction to the Standard Model and Electroweak Physics, arXiv:0901.0241v1 (2009).

[2] A.Salam, Elementary particle Theory, Ed. N. Svarholm (1968).

[3] H. Fritzsch and M. Gell-Mann, Proc. XVI Int. Conf. on High Energy Physics, Batavia 1972, Vol. 2, p. 135.

[4] S. Gariazzo et al., “Neutrino masses and their ordering: Global Data, Priors and Models”, arXiv:1801.04946 (2018).

[5] G. Kane, “The dawn of physics beyond the standard model”, Scientific American, vol. Sp 15, pp. 4–11, 2006. doi:10.1038/scientificamerican0206-4sp

[6] K. Nakamura et al. (Particle Data Group). Review of particle physics. J. Phys. G: Nucl. Part. Phys., 37:075021, 2010.

[7] F. Halzen and A. D. Martin, “Quarks and Leptons: An Introductory Course in Modern Particle Physics”, John Wiley & Sons Inc., New York, USA, 1984. ISBN-9780471887416.

[8] F. Englert and R. Brout. Broken Symmetry and the Mass of Gauge Vector Mesons. Phys. Rev. Lett., 13:321-323, Aug 1964. doi:10.1103/PhysRevLett.13.321

[9] P.W. Higgs, Broken symmetries, massless particles and gauge fields. Phys. Lett. 12, 132 (1964). doi:10.1016/0031-9163(64)91136-9

[10] Peter W. Higgs. Broken Symmetries and the Masses of Gauge Bosons. Phys. Rev. Lett., 13:508-509, Oct 1964. doi:10.1103/PhysRevLett.13.508

[11] G.S. Guralnik, C.R. Hagen, T.W.B. Kibble, Global conservation laws and massless particles. Phys. Rev. Lett. 13, 585 (1964). doi:10.1103/PhysRevLett.13.585

[12] P.W. Higgs, Spontaneous symmetry breakdown without massless bosons. Phys. Rev. 145, 1156 (1966). doi:10.1103/PhysRev.145.1156

[13] Y. Nambu, G. Jona-Lasinio, Dynamical model of elementary particles based on an analogy with superconductivity. I. Phys. Rev. 122, 345 (1961). doi:10.1103/PhysRev.122.345

[14] Y. Nambu, Spontaneous Symmetry Breaking in Particle Physics: A Case of Cross Fertilization (The Nobel Foundation, 2008)

[15] M. Gell-Mann, M. Levy, The axial vector current in beta decay. Nuovo Cim. 16, 705 (1960). doi:10.1007/BF02859738

[16] CMS collaboration, “Observation of a new boson at a mass of 125 GeV with the CMS experiment at the LHC”, Physics Letters B, 716:30–61, September 2012. doi:10.1016/j.physletb.2012.08.021. arXiv:1207.7235

[17] ATLAS collaboration, "Observation of a new particle in the search for the Standard Model Higgs boson with the ATLAS detector at the LHC", Physics Letters B, 716:01–29, September 2012. doi:10.1016/j.physletb.2012.08.020. arXiv:1207.7214

[18] CMS Collaboration, Observation of a new boson with mass near 125 GeV in pp collisions at $\sqrt{s}$ = 7 and 8 TeV. J. High Energy Phys. 06, 081 (2013). doi:10.1007/JHEP06(2013)081. arXiv:1303.4571

[19] CMS Collaboration, Search for the standard model Higgs boson produced in association with a W or a Z boson and decaying to bottom quarks. Phys. Rev. D 89, 012003 (2014). doi:10.1103/PhysRevD.89.012003. arXiv:1310.3687

[20] ATLAS Collaboration, Search for Higgs boson decays to a photon and a Z boson in pp collisions at $\sqrt{s}$ = 7 and 8 TeV with the ATLAS detector. Phys. Lett. B 732, 8 (2014). doi:10.1016/j.physletb.2014.03.015. arXiv:1402.3051

[21] ATLAS Collaboration, Evidence for the spin-0 nature of the Higgs boson using ATLAS data. Phys. Lett. B 726, 120 (2013). doi:10.1016/j.physletb.2013.08.026. arXiv:1307.1432

[22] CMS Collaboration, Constraints on the spin-parity and anomalous HVV couplings of the Higgs boson in proton collisions at 7 and 8 TeV, (2014). arXiv:1411.3441. Submitted for publication in Phys. Rev. D

[23] CMS Collaboration, Precise determination of the mass of the Higgs boson and tests of compatibility of its couplings with the Standard Model predictions using proton collisions at 7 and 8 TeV, Eur. Phys. J. C (2015) 75: 212. doi:10.1140/epjc/s10052-015-3351-7. arXiv:1412.8662v2

[24] ATLAS Collaboration, Measurements of Higgs boson production and couplings in the four-lepton channel in pp collisions at center-of-mass energies of 7 and 8 TeV with the ATLAS detector, Phys. Rev. D 91, 012006 (2015). doi:10.1103/PhysRevD.91.012006. arXiv:1408.5191v3

[25] CDF and D0 Collaborations, Evidence for a particle produced in association with weak bosons and decaying to a bottom-anti-bottom quark pair in Higgs boson searches at the Tevatron. Phys. Rev. Lett. 109, 071804 (2012). doi:10.1103/PhysRevLett.109.071804. arXiv:1207.6436

[26] CDF and D0 Collaborations, Higgs boson studies at the Tevatron. Phys. Rev. D 88, 052014 (2013). doi:10.1103/PhysRevD.88.052014. arXiv:1303.6346

[27] N. Cabibbo (1963). "Unitary Symmetry and Leptonic Decays". Physical Review Letters. **10** (12): 531–533, doi:10.1103/PhysRevLett.10.531

[28] M. Kobayashi, T. Maskawa; Maskawa (1973). "CP-Violation in the Renormalizable Theory of Weak Interaction". Progress of Theoretical Physics. **49** (2): 652–657. doi:10.1143/PTP.49.652

[29] Beringer, J,…, et al. (2012). "Review of Particles Physics: The CKM Quark-Mixing Matrix" (PDF). Physical Review D. **80** (1): 1–1526 [162]. doi:10.1103/PhysRevD.86.010001
[30] Tegmark, M. et al., Cosmological parameters from SDSS and WMAP, Phys. Rev. D 69 (2004) 103501. doi:10.1103/PhysRevD.69.103501. arXiv:astro-ph/0310723v2
[31] H. Murayama, "Supersymmetry phenomenology", arXiv:hep-ph/0002232.
[32] P. G. O. Freund, "Introduction to Supersymmetry". Cambridge University Press, 1986. Cambridge Monographs On Mathematical Physics. ISBN-9780521356756.
[33] C. T. Hill and E. H. Simmons, Phys. Rept. 381 (2003) 235-402. doi: 10.1016/S0370-1573(03)00139-X.
[34] K. D. Lane, Technicolor 2000, arXiv:hep-ph/0007304v1.
[35] N. Arkani-Hamed, A. G. Cohen, and H. Georgi, Electroweak symmetry breaking from dimensional deconstruction, Phys. Lett. B513 (2001), 232-240. doi:10.1016/S0370-2693(01)00741-9. arXiv:hep-ph/0105239v4
[36] K. Nakamura et al. (Particle Data Group). COSMIC RAYS. Chin. Phys. C, 40, 100001 (2016)
[37] A Haungs et al., KCDC — The KASCADE Cosmic-ray Data Centre, J.Phys.Conf.Ser. 632 (2015) no.1, 012011, doi:10.1088/1742-6596/632/1/012011. arXiv:1504.06696v1
[38] Morison, Ian (2008). Introduction to Astronomy and Cosmology. John Wiley & Sons. p. 198. ISBN 978-0-470-03333-3.
[39] Street, J.; Stevenson, E. (1937). "New Evidence for the Existence of a Particle of Mass Intermediate Between the Proton and Electron". Physical Review. 52 (9): 1003. doi:10.1103/PhysRev.52.1003
[40] Einstein A. (1916), Relativity: The Special and General Theory (Translation 1920), New York: H. Holt and Company
[41] CMS Collaboration, Measurement of the charge ratio of atmospheric muons with the CMS detector, Phys.Lett.B692:83-104 (2010), doi: 10.1016/j.physletb.2010.07.033.
[42] S. Cecchini, M. Sioli, Cosmic Ray Muon Physics, DFUB 99-26, arXiv:hep-ex/0002052
[43] A.H. Maghrabi, H. Al Harbi, Z.A. Al-Mostafa, M.N. Kordi, S.M. Al-Shehri, The KACST muon detector and its application to cosmic-ray variations studies, Advances in Space Research 50(6),2012, doi:10.1016/j.asr.2011.10.011
[44] CMS Collaboration, Performance of CMS Muon Reconstruction in Cosmic-Ray Events, JINST 5:T03022 (2010), doi:10.1088/1748-0221/5/03/T03022. arXiv:0911.4994v2

[45] Kunihiro Morishima et al., Discovery of a big void in Khufu's Pyramid by observation of cosmic-ray muons, Nature volume 552, 386–390 (2017), doi:10.1038/nature24647.
[46] The Large Hadron Collider Project, http://lhc.web.cern.ch/lhc/.
[47] O. S. Brüning et al., LHC Design Report. Geneva: CERN, 2004.
[48] J. Stirling, "Tevatron and lhc parton luminosity comparison plots." http://www.hep.ph.ic.ac.uk/~wstirlin/plots/plots.html.
[49] CERN Document Server, "LHC Project Illustration: Cross section of LHC dipole". http://cdsweb.cern.ch/record/842530.
[50] O. Br¨uning and P. Collier, "Building a behemoth", Nature Insight: The Large Hadron Collider 448 (2010), no. 7151, 285–289. doi:10.1038/nature06077.
[51] CMS Collaboration, "The CMS Experiment at the CERN LHC," *Journal of Instrumentation*, vol. 3, no. 08, p. S08004, 2008.
[52] ATLAS Collaboration, "The ATLAS Experiment at the CERN LHC," *Journal of Instrumentation*, vol. 3, no. 08, p. S08003, 2008.
[53] ALICE Collaboration, "The ALICE experiment at the CERN LHC," *Journal of Instrumentation*, vol. 3, no. 08, p. S08002, 2008.
[54] LHCb Collaboration, A. A. Alves, et al., "The LHCb detector at the LHC," Journal of Instrumentation 3 no. 08, (Aug., 2008) S08005. http://iopscience.iop.org/1748-0221/3/08/S08005.
[55] L. Evans and P. Bryant, "LHC Machine," Journal of Instrumentation, vol. 3, no. 08, p. S08001, 2008.
[56] TOTEM Collaboration, "The TOTEM Experiment at the CERN LHC," Journal of Instrumentation, vol. 3, no. 08, p. S08007, 2008.
[57] CMS Collaboration, The Compact Muon Solenoid - Technical Proposal, CERN/LHCC 94-38, 1995.
[58] M. Pimiia, M. Della Negra, K. Eggert et al., "Compact Muon Solenoid". CERN, Geneva, 1990. Proceedings of the Large Hadron Collider Workshop Aachen, 4-9 October 1990, p.547. CERN-90-10-V-3. ECFA-90-133-V-3.
[59] http://cdsweb.cern.ch/record/215299.
[60] CMS Collaboration, "CMS Expression of Interest". CERN, Geneva, 1992. Proceedings of the General Meeting on LHC Physics and Detectors, Evian-les-Bains, France, 5-8 Mar 1992, pp.165-217. http://cdsweb.cern.ch/record/247455.
[61] CMS Collaboration, "Technical proposal". LHC Tech. Proposal. CERN, Geneva, 1994. CERN-LHCC-94-38. LHCC-P-1. http://cdsweb.cern.ch/record/290969.
[62] CMS Collaboration, "The CMS magnet project: Technical Design Report". Technical Design Report CMS. CERN, Geneva, 1997. CERN-LHCC-97-010. CMS-TDR-001. http://cdsweb.cern.ch/record/331056.

[63] CMS collaboration, The CMS tracker system project: technical design report, CERN-LHCC-98-006, http://cdsweb.cern.ch/record/368412.
[64] CMS collaboration, The CMS tracker: addendum to the technical design report, CERN-LHCC-2000-016, http://cdsweb.cern.ch/record/490194.
[65] Aaron Dominguez. The cms pixel detector. Technical Report, CMS-CR-2009-142. CERN-CMS-CR-2009-142, CERN, Geneva, Jun 2009.
[66] CMS Collaboration, "The CMS Experiment at the CERN LHC", Journal of Instrumentation 3 (2008), no. 08, S08004. doi:10.1088/1748-0221/3/08/S08004.
[67] CMS Collaboration, "CMS Tracking Performance Results from Early LHC Operation", Journal of High Energy Physics 70 (2010), no. 4, 1165–1192, arXiv:1007.1988.
[68] J. Sharka et al., Construction of the CDF silicon vertex detector., IEEE Transactions on Nuclear Science 39 (1992).
[69] A Satpathy, Overview and status of the CMS silicon strip tracker, J.Phys.Conf.Ser.110:092026, 2008 , arXiv:0709.3612.
[70] CMS Collaboration, CMS ECAL Technical Design Report, CERN/LHCC 97-33 CMS TDR 4, http://cmsdoc.cern.ch/ftp/TDR/ECAL/ecal.html
[71] CMS Collaboration, "Measurement of the Differential Cross Section for Isolated Prompt Photon Production in pp Collisions at 7 TeV", Phys. Rev. D84 (2011) 052011, arXiv:1108.2044. CMS-QCD-10-037. CERN-PH-EP-2011-128.
[72] CMS Collaboration, Performance, Calibration and Alignment of the CMS Preshower Detector, https://doi.org/10.1016/j.nuclphysbps.2011.03.153
[73] CMS Collaboration. CMS: The Hadron Calorimeter. Technical Design Report., CERN-LHCC-97-31.
[74] CMS Collaboration, "Measurement of energy flow at large pseudorapidities in pp collisions at $\sqrt{s} = 0.9$ and 7 TeV", JHEP 1111 (2011) 148, arXiv:1110.0211.
[75] L. Evans and P. Bryant, "LHC Machine," JINST 3, S08001 (2008).
[76] CMS collaboration (1997) The Muon Project, CMS Technical Design Report, CERN/LHCC 97-32, CMS-TDR-003.
[77] ATLAS, CMS collaboration, Combined Measurement of the Higgs Boson Mass in pp Collisions at $\sqrt{s} = 7$ and 8 TeV with the ATLAS and CMS Experiments, Phys. Rev. Lett. 114 (2015) 191803, arXiv:1503.07589
[78] CMS Collaboration, "CMS Physics, Technical Design Report, Volume I: Detector Performance and Software", CERN/LHCC 2006-001, CMS TDR 8.1.
[79] W. Blum, L. Rolandi, and W. Riegler, "Particle detection with drift chambers". Berlin, Germany: Springer, 2008. ISBN-9783540766834.
[80] S. Chatrchyan et al., "The performance of the CMS muon detector in proton-proton collisions at $\sqrt{s} = 7$ TeV at the LHC," Journal of Instrumentation, vol. 8, p. P11002, 2013. doi:10.1088/1748-0221/8/11/P11002

[81] M. C. Fouz, ”The CMS muon system”, Nucl. Instr. and Meth. in Physics Research A 446 (2000) 366-372.
[82] H. Wells Wulsin, Performance of the Cathode Strip Chamber endcap muon detectors in Run 2, arXiv:1510.08908.
[83] CMS Collaboration, Fast algorithm for track segment and hit reconstruction in the CMS Cathode Strip Chambers, https://doi.org/10.1016/j.nima.2008.02.096
[84] G. Wrochna, “The RPC System for the CMS Experiment at LHC,” No. CMS TN- 1995/182 , Dec 1995
[85] Abbrescia M. et al. (2005) Cosmic ray test of double-gap resistive plate chambers for the CMS experiment, Nucl. Instr. Meth. A., 550, 116.
[86] CMS collaboration (2000) The TriDAS Project, CMS Technical Design Report, CERN/LHCC 2000 - 38CMS TDR 6.1
[87] CMS Collaboration, “CMS TriDAS project: Technical Design Report 2: Data-acquisition and high-level trigger”. Technical Design Report CMS. CERN, Geneva, 2002. CERN-LHCC-2002-026. CMS-TDR-006-add-2.
[88] CMS Collaboration, The CMS trigger system, JINST 12 (2017) P01020, arXiv:1609.02366.
[89] M Jeitler et al, The level-1 global trigger for the CMS experiment at LHC, 2007 JINST 2 P01006, https://doi.org/10.1088/1748-0221/2/01/P01006
[90] CMS Collaboration, LHC computing Grid. Technical design report, CERN-LHCC-2005-024, LCG-TDR-001
[91] E. Rutherford, H. Geiger, and J. Harling, “An Electrical Method of Counting the Number of α Particles from Radio-Active Substances,” Royal Society of London Proceedings Series A, vol. 81, pp. 141–161, Aug. 1908.
[92] F. Sauli, Gaseous radiation detectors: fundamentals and applications. Cambridge monographs on particle physics, nuclear physics and cosmology, Cambridge: Cambridge Univ. Press, 2014.
[93] V. Parkhomchuck, Y. Pestov, and N. Petrovykh, “A spark counter with large area” Nuclear Instruments and Methods, vol. 93, no. 2, pp. 269 – 270, 1971.
[94] Y. Pestov and G. Fedotivich, “A Picosecond Time Of Flight Spectrometer For The VEPP-2m Based On Local-Discharge Spark Counter,” SLAC SciDoc. SLAC Translation: SLAC-TRANS-0184.
[95] R. Santonico and R. Cardarelli, “Development of resistive plate counters,” Nucl. Instrum. Methods, vol. 187, p. 377, 1981. doi:10.1016/0029-554X(81)90363-3
[96] R. Cardarelli, A. Di Ciaccio, and R. Santonico, “Performance of a resistive plate chamber operating with pure CF3Br,” Nucl. Instrum. Meth., vol. A333, pp. 399– 403, 1993. doi:10.1016/0168-9002(93)91182-M.
[97] I. Crotty, J. Lamas Valverde, G. Laurenti, M. C. S. Williams, and A. Zichichi, “The Nonspark mode and high rate operation of resistive parallel plate

chambers," Nucl. Instrum. Meth., vol. A337, pp. 370–381, 1993. doi:10.1016/0168-9002(94)91105-3
[98] M. Abbrescia et al., "The simulation of resistive plate chambers in avalanche mode: Charge spectra and efficiency," Nucl. Instrum. Meth., vol. A431, pp. 413–427, 1999. doi:10.1016/S0168-9002(99)00374-5.
[99] A. Fridman and L. A. Kennedy, Plasma Physics and Engineering. Taylor and Francis, New York.
[100] CMS Collab. CMS Physics Technical Design Report. Vol. I: Detector Performance and Software, CERN/LHC, 1, 2006
[101] M. Abbrescia et al., "Effect of the Linseed Oil Treatment on the Performance of the Resistive Plate Counters," Tech. Rep. CMS-NOTE-1997-018.
[102] L. Changguo, "RPC electrode material study," Nucl. Instrum. Meth. A , vol. 602, no. 3, pp. 761 – 765, 2009. doi:10.1016/j.nima.2008.12.225
[103] M. Abbrescia et al., "Properties of the C2H2F4 based gas mixture for avalanche mode operation of Resistive Plate Chambers," Tech. Rep. CMS-NOTE-1997-004, CERN, Geneva, Jan 1997.
[104] P. Camarri et al., "Streamer suppression with SF6 in RPCs operated in avalanche mode," Nucl. Instrum. Meth. A, vol. 414, pp. 317 – 324, 1998. doi:10.1016/S0168-9002(98)00576-2
[105] M. Abbrescia et al., "Study of long-term performance of CMS RPC under irradiation at the CERN GIF," Nucl. Instrum. Meth. A, vol. 533, pp. 102 – 106, 2004, doi:10.1016/j.nima.2004.07.009
[106] M. Abbrescia et al., Beam test results on double-gap resistive plate chambers proposed for CMS experiment, Nucl. Instrum. Meth. A, vol. 414, pp. 135 – 148, 1998, https://doi.org/10.1016/S0168-9002(98)00571-3
[107] M. Abbrescia et al., "New Developments on Front End Electronics for the CMS Resistive Plate Chambers," Nucl. Instrum. Meth. A, vol. 456, p. 143, 2000.
[108] CMS collaboration, Up-scope of the CMS forward RPC low η system, Technical Design Report.
[109] F. Loddo et al., Front end electronics for RPC detector of CMS, Proceedings of the Fourth International Workshop on Resistive Plate Chambers and related Detectors, Napoli, 1997.
[110] M.L. Simpson et al., IEEE Trans. Nucl. Sci. NS-42 (4) (1995) 762.
[111] ANSI/TIA/EIA-644-A-2001, Std 1014-1987 IEEE Standard for A Versatile Backplane Bus: VMEbus.
[112] A. Ranieri, A New Front-End Board for RPC Detector of CMS, CERN-CMS-NOTE-1999-047

[113] CMS Collaboration, “Technical Proposal for the Upgrade of the CMS Detector through 2020”, CERNLHCC-2011-008, CMS-UG-TP-1, LHCC-P-004.
[114] S Colafranceschi. et al. (2014) Resistive Plate Chambers for 2013-2014 muon upgrade in CMS at LHC, JINST, 9, C10033. https://doi.org/10.1088/1748-0221/9/10/C10033
[115] M. Shopova et. al., “Resistive plate chambers for the LS1 muon upgrade in CMS experiment at LHC”, Bulgarian Chemical Communications, Volume 47, Special Issue B (pp. 185–191) 2015.
[116] M. Tytgat et al., The upgrade of the CMS RPC System during the First LHC Long Shutdown, 2013 *JINST* **8** T02002
[117] S. K. Park et al., RPC Gap Production and Performance for CMS RE4 Upgrade, arXiv:1408.3720
[118] S. Park et al., Production of gas gap for Forward RPCs of the CMS experiments, Nucl. Instr. Meth. A 550 (2005) 551
[119] S. Park et al., Beam test results of CMS RPCs at high eta region under high-radiation environment, Nucl. Instr. Meth. A 533 (2004) 37
[120] L.M. Pant et al., Resistive Plate Chambers for the upgrade of the CMS experiment, DAE Symp.Nucl.Phys. 57 (2012) 146-154
[121] CMS RE4 website. http://rpc-cms-re4-upscope.web.cern.ch/favicon.ico
[122] Glenn F. Knoll. Radiation, Detection And Measurement. Wiley, fourth edition, 2010. ISBN 978-0470131480
[123] P. Paolucci et al., The Detector Control Systems for the CMS Resistive Plate Chamber, CMS NOTE -2008/036
[124] A. Ball et al. Cosmic Ray Test Certi cation of the First 100 CMS Endcap RPCs and the Corresponding Construction Database. Nucl. Phys. B, 158:991 02, 2006
[125] M. Abbrescia et al., Resistive plate chambers performances at cosmic rays fluxes Nucl.Instrum.Meth. A359 (1995) 603-609
[126] S. Carpinteyro Bernardino et al., Quality Certification 4 (QC4) for RE4 in the Upgrade in CMS, Journal of Physics: Conference Series 651 (2015) 012005
[127] R. Mileva (2014). Изследвания с детектора CMS на събития с два мюона в крайното състояние. Sofia University. Faculty of Physics, Sofia, Bulgaria.
[128] G. Franzoni et al., Dataset definition for CMS operations and physics analyses, Nuclear and Particle Physics Proceedings 273–275 (2016) 929–933
[129] F. Thyssen, (2014). Commissioning, operation and performance of the CMS resistive plate chamber system. Ghent University. Faculty of Sciences, Ghent, Belgium.
[130] C. Carrillo, Search for Heavy Stable Charged Particles in the CMS Experiment using the RPC Detectors, CMS-TS-2011-018, CERN-THESIS-2011-032

[131] cms-sw · GitHub
[132] Rene Brun and Fons Rademakers, ROOT - An Object Oriented Data Analysis Framework, Proceedings AIHENP'96 Workshop, Lausanne, Sep. 1996, Nucl. Inst. & Meth. in Phys. Res. A 389 (1997) 81-86. See also http://root.cern.ch/
[133] Rene Brun and Fons Rademakers, ROOT — A C++ framework for petabyte data storage, statistical analysis and visualization, Computer Physics Communications; Anniversary Issue; Volume 180, Issue 12, December 2009, Pages 2499-2512
[134] CMS Collaboration, CMS distributed data analysis with CRAB3, Journal of Physics: Conference Series, Volume 664, CMS distributed data analysis with CRAB3 - IOPscience
[135] CMS Collaboration, Performance of the CMS Muon Detectors in 2016 collision runs, CERN-CMS-DP-2016-046
[136] CMS 2015 - taking data under difficult conditions | EP Department newsletter
[137] M. Shopova et al., Performance of Resistive Plate Chambers installed during the first long shutdown of the CMS experiment, CMS CR-2016/090, arXiv:1605.06798
[138] CMS Collaboration, Muon Identification performance: hadron mis-Id measurements and RPC Muon selections, CERN-CMS-DP-2014-018
[139] CMS Collaboration, Performance of CMS muon reconstruction in pp collision events at sqrt(s)=7 TeV 2012 JINST 7 P10002
[140] CMS Collaboration, First Muon Identification Efficiencies with 13TeV, 50 ns Data, CERN-CMS-DP-2015-047
[141] CMS collaboration, The CMS Resistive Plate Chambers system-detector performance during 2011, in Proceedings of the 13th ICATPP Conference, Villa Olmo, Como, Italy, 3–7 October 2011, pp. 460–468.
[142] R. Trejo et al., CMS RPC background studies during LHC run II, XIV Workshop on Resistive Plate Chambers and related detectors, Plenary talk